CORA Cork Open Research Archive
Cartlann Taighde Oscailte Chorcaí

Title	Fourier analysis of index-patterned Fabry-Pérot lasers
Authors	Boohan, Niall
Publication date	2024
Original Citation	Boohan, N. 2024. Fourier analysis of index-patterned Fabry-Pérot lasers. PhD Thesis, University College Cork.
Type of publication	Doctoral thesis
Rights	© 2024, Niall Boohan. - https://creativecommons.org/licenses/by/4.0/
Download date	2026-10-30 00:57:00
Item downloaded from	https://hdl.handle.net/10468/17491



UCC
University College Cork, Ireland
Coláiste na hOllscoile Corcaigh

NATIONAL UNIVERSITY OF IRELAND, CORK.

DOCTORAL THESIS

Fourier Analysis of Index-Patterned Fabry-Pérot Lasers

Author:

Mr. Niall Boohan

Supervisors:

Prof. Eoin O'Reilly

and

Mr. Brian Corbett

A thesis submitted in fulfilment of the requirements

for the degree of Doctor of Philosophy

in the

Photonics Theory Group,

School of Physics

Head of School:

Prof. Paul Callanan

December 2, 2024

Contents

Contents i

Declaration of authorship iv

Acknowledgements vii

List of abbreviations viii

Physical/mathematical units and constants ix

List of symbols and terms x

1 A background to index-patterned lasers 1
- 1.1 Introduction . . . 1
- 1.2 Overview of the single-frequency index-patterned laser . . . 3
- 1.3 The state-of-the-art in index-patterned lasers . . . 8
- 1.4 Objectives for this thesis . . . 10

2 The fundamentals of edge-emitting semiconductor lasers 12
- 2.1 Introduction . . . 12
- 2.2 Semiconductor lasing . . . 14
- 2.3 Complex refractive index . . . 19
- 2.4 Reflectivity and mirror loss . . . 21
- 2.5 The waveguide . . . 22
- 2.6 Modes . . . 27
  - 2.6.1 Longitudinal . . . 27
  - 2.6.2 Transverse . . . 28
- 2.7 The Fabry-Pérot laser cavity model . . . 30
- 2.8 The scattering matrix . . . 32
- 2.9 Discussion . . . 34

3 Single-frequency lasers 35
- 3.1 Introduction . . . 35
- 3.2 The index-patterned laser . . . 37
  - 3.2.1 The slot . . . 37
  - 3.2.2 Slot positioning for lasing mode enhancement . . . 39
  - 3.2.3 Slot pattern design using a feature density weighting function . . . 43
  - 3.2.4 Fourier calculation of the modal mirror loss . . . 49
  - 3.2.5 Spectral effects of slot-width . . . 52
- 3.3 The scattering matrix method (SMM) . . . 55
- 3.4 Bragg grating-based devices . . . 59
  - 3.4.1 The Bragg mirror . . . 59

3.4.2 The distributed feedback (DFB) laser . . . 61
3.4.3 The distributed Bragg reflector (DBR) laser . . . 64
3.5 Discussion . . . 65

4 Fourier cavity modelling **67**
4.1 Introduction . . . 67
4.1.1 A mathematical verification of the impact of weighted-average slot position on mode selectivity . . . 69
4.1.2 Grating-facet phase error . . . 70
4.2 Fourier analysis of exemplar design functions . . . 72
4.2.1 $f_1(\epsilon) = 1$ . . . 74
4.2.2 $f_2(\epsilon) = |\epsilon|$ . . . 75
4.2.3 $f_3(\epsilon) = \epsilon \sin(2\pi\epsilon)$ . . . 77
4.2.4 Verification of the first-order approximation and quantifying higher-order reflections in the cavity . . . 79
4.2.5 Change in modal threshold function with grating-facet phase . . . 81
4.2.5.1 Large changes in the relative grating-facet position . . . 85
4.3 Analysis . . . 88
4.3.1 Mode selectivity with weighted-average slot position . . . 88
4.3.2 The Fourier properties of index-patterned gratings . . . 89
4.3.3 Grating-facet phase and yield . . . 92
4.3.4 Thermal analysis; gain-bandwidth case study . . . 94
4.4 Discussion . . . 97

5 Implementation of Fourier designed gratings **98**
5.1 Introduction . . . 98
5.1.1 Design of experiment . . . 99
5.2 Results . . . 105
5.2.1 SMSR versus wavelength distribution . . . 106
5.2.2 General performance parameters . . . 110
5.3 Analysis . . . 113
5.3.1 Fourier model fitting . . . 113
5.3.1.1 Modal excitation and suppression from cavity resonances . . . 113
5.3.1.2 Variation in cavity refractive index . . . 121
5.3.2 General performance analysis . . . 122
5.3.2.1 Mode selectivity . . . 122
5.3.2.2 Loss . . . 122
5.3.2.3 Grating-facet phase and yield . . . 124
5.4 Discussion . . . 125

6 High-reflectivity facet index-patterned devices **126**
6.1 Introduction . . . 126
6.1.1 Change in weighting and design function after HR coating . . . 128
6.1.2 Chosen mode selectivity after HR coating . . . 131
6.1.3 Design of experiment . . . 132
6.2 Results . . . 138
6.2.1 SMSR versus wavelength distribution . . . 138
6.2.1.1 275 µm UC → HR . . . 138
6.2.1.2 350 µm HR . . . 140
6.2.2 General performance . . . 142

6.2.2.1 275 µm UC → HR . . . 142
6.2.2.2 350 µm HR . . . 145
6.3 Analysis . . . 147
6.3.1 Loss . . . 147
6.3.2 SMSR sensitivity to slot depth . . . 149
6.3.3 275 µm UC → HR mode selectivity . . . 151
6.3.4 Yield . . . 151
6.4 Discussion . . . 152

7 Conclusions & outlook **153**
7.1 Introduction . . . 153
7.2 Summary and research outcomes . . . 155
7.3 Maximising performance and yield . . . 157
7.3.1 Performance . . . 157
7.3.2 Yield . . . 159
7.4 Future modelling paths . . . 160

Declaration of authorship

I, Niall Boohan, certify that this thesis is my own work and I have not obtained a degree in this university or elsewhere on the basis of the work submitted in this thesis.

Niall Boohan

"I see no limit to the capabilities of machines"

— Claude Shannon

Abstract

Optoelectronics has the potential to revolutionise mass-produced, consumer-level goods (health, LiDAR, and 6G internet) as it has done for high-tech, specialised applications in metrology, spectroscopy, and telecommunications. To achieve this, key components need to become more structurally robust and easier to manufacture. The index-patterned laser, using a perturbation-based grating within the cavity waveguide, shows great potential as a low-cost, single-frequency light source. However, further research and understanding of the dependence of the device lasing spectrum on the grating perturbations within the cavity is required. This thesis uses a first-order reflection approximation, to allow a Fourier transform-based analysis of grating patterns and cavity structures to improve single-mode selectivity and device yield.

We demonstrate how placing the weighted average of the grating perturbation positions closer to the emitting facet can be used to select the lasing mode more strongly. The perturbations interact with the cavity facets to generate modal selection. However, it is not possible to control the facet-to-grating distance precisely enough to ensure a full yield of single-frequency lasers at predetermined wavelengths. We show that the phase difference between the laser light electric field at the perturbations and at the facet can be used to calculate the emission spectrum. This gives us a method for studying these facet position effects on the spectrum. In addition to this, we show how the change in the cavity resonances with length affects mode selection in the device. We analyse for the first time the effects of applying a high-reflectivity facet to the predominant reflecting facet of the cavity for mode selection. We also analyse the effects of higher-order reflections not included in our Fourier method, allowing us to assess its accuracy. The results are supported with a comparison against the experimental data. The grating pattern, position, and facet reflectivity can be used to create devices that have greater spectral purity with lower optical loss. Our ability to relate grating position and mode resonances in the cavity to the calculated device spectrum enables rapid analysis of grating designs for further potential yield improvements.

Future modelling work could include applying our designed laser to two-dimensional models with a non-constant refractive index, as this will capture further important device effects not included in our Fourier model.

Acknowledgements

I would like to start by thanking my supervisors Eoin and Brian. I have learnt so much during my Ph.D.. Although not the best place to admit it, Eoin has definitely opened my eyes to the power of maths. For Brian, this is my second time around working with him, and there isn't anyone better to learn from to make photonic devices.

I would like to thank my colleagues in the photonics theory group. I could not have asked for a nicer bunch of people to work alongside, and regret that I couldn't make it to the office more often! I would also like to thank my colleagues in PIADS. I really enjoyed getting to know you all and again regret we didn't spent more time together.

I would also like to thank Brian Kelly and The Team at Eblana Photonics Ltd., for the devices and experimental testing in this thesis. I would also like to thank Brian for his feedback and encouragement during the research.

List of abbreviations

AU	**A**rbitary **U**nits
CMOS	**C**omplementary **M**etal- **O**xide-**S**emiconductor
D	**D**imension
DBR	**D**istributed **B**ragg **R**eflrctor
DFB	**D**istributed **F**eed**B**ack
E	**E**lectric
E-beam	**E**lectron-beam
EM	**E**lectro-**M**agnetic
FWHM	**F**ull **W**idth at **H**alf-**M**aximum
HW	**H**alf-**W**avelength
HR	**H**igh-**R**eflectivity
LiDAR	**Li**ght **D**etection and **R**anging
PIC	**P**hotonic **I**ntegrated **C**ircuit
QW	**Q**uarter-**W**avelength
SCH	**S**eparate **C**onfinement **H**eterostructure
SEM	**S**canning **E**lectron **M**icroscope
SFP	**S**lotted **F**abry-**P**érot
SMM	**S**cattering **M**atrix **M**ethod
TE	**T**ransverse **E**lectric
TEM	**T**ransverse **E**lectro-**M**agnetic
TM	**T**ransverse **M**agnetic

Physical/mathematical units and constants

Speed of light	$c = 2.997\,924\,58 \times 10^{8}$ m/s
Permittivity of free-space	$\epsilon_0 = 8.854\,187\,81 \times 10^{-12}$ F/m
Permeability of free-space	$\mu_0 = 1.256\,637\,06 \times 10^{-10}$ N/m^2
Planck's constant	$h = 6.626\,070\,15 \times 10^{34}$ Js
Boltzmann constant	$k_B = 8.617\,333\,262 \times 10^{5}$ JK^{-1}
Elementary charge	$q = 1.602\,176\,63 \times 10^{19}$ C
pi	$\pi = 3.141\,592\,65$
Euler's number	$e = 2.718\,281\,82$
Imaginary unit	$i = \sqrt{-1}$

List of symbols and terms

α	Optical loss	cm^{-1}
α_p, α_g	Propagation, grating loss	cm^{-1}
α_f, α_U, α_H	Facet/mirror, uncoated, high-reflectivity coated loss	cm^{-1}
α_m	Modal mirror loss	cm^{-1}
$\Delta\alpha_m$ $\Delta\alpha_{m_0}$	Mode, selected mode mirror loss modulation	cm^{-1}
$20/50\Delta\alpha$, $\Delta\alpha_{nn}$	Mode selectivity against a twenty/fifty mode bandwidth, nearest neighbours	cm^{-1}
β_{sp}	Spontaneous emission factor	
Γ	Optical confinement factor	
ϵ	Normalised cavity position	
η	Slope efficiency	W/A
η_i	Current injection efficiency	
η_r	Radiative efficiency	
κ	Grating coupling factor	
λ	Wavelength	nm or µm
λ_{err}	Erroneous wavelength	nm or µm
$\delta\lambda$	Gain-bandwidth FWHM	nm or µm
λ_m	Fabry-Pérot cavity mode wavelength	nm or µm
λ_B	Bragg wavelength	nm or µm
ρ	Charge density	C/m^2
ϕ	Phase	
Φ	Phase position in index-patterned cavity	
ω	Radial frequency	$rads^{-1}$

A	Recombination factor	
C	Normalisation factor	
d	Slot-width	µm or nm
D	Density of states	$eV^{-1}cm^{-2}$
$\hat{E}$	Electric field amplitude	V/m
$E_{v,c,g}$	Energy levels in the valence, conduction, or bandgap	eV
E_{f_v,f_c}	Quasi Fermi energy in the valence or conduction band	eV
E_p	Mode energy level	eV
f	Frequency	Hz
$f_{v,c}$	Fermi-Dirac occupation probability valence or conduction band	
$f(\epsilon)$	Design function at ϵ	
Δf	Mode linewidth	MHz or kHz
F_{err}	Fractional cavity length	
g, g_m, Δg	Material, modal, referenced against gain-bandwidth peak gain	cm^{-1}
δg	Marginal gain	cm^{-1}
G	Threshold gain	cm^{-1}
$h(\epsilon)$	Design function after cavity weighting at ϵ	
$\hat{H}$	Magnetic field strength	A/m
$\hat{I}$,$\hat{J}$	Current, current density	A, A/m^2
I	Optical intensity	W/m^2
I_{th}	Threshold current	mA
k	Free-space wavenumber	nm^{-1} or μm^{-1}
L	Cavity length	µm or cm
L_{err}	Cavity length error	µm or cm
m	Mode number	
m_0	Chosen mode number	
M	Non-integer off-set mode number	
$\tilde{n}$, n, n'	Complex, real, imaginary refractive index	
N	Number of slots	
p	Integer	
P	Single-facet optical power or referenced to 1 mW	mW or dB
ΔP	Fractional change in power	mW or dB
Q	Q-factor	
r,R	Amplitude reflectivity, power reflectance	
R_{st}	Stimulated recombination rate	s^{-1}
S	Scattering parameter	
SMSR	Side-mode suppression ratio	dB
T	Temperature	K or °C
t,T	Amplitude transmissivity, power transmittance	
t	Time	s
$w(\epsilon)$	Cavity weighting function at ϵ	
$\hat{x}$, $\hat{y}$, $\hat{z}$	Cartesian coordinates	nm or µm or cm

Now all the business is out of the way, I would very much like to thank my girlfriend, Виктория*, for all her support throughout all the writing. I would like to thank my family for their support throughout the Ph.D., and my father, John. I would like to thank my nieces and nephews for their "Encouragement" to complete the thesis, after they discovered that a trip to Shake Dog was lined up to celebrate handing it in. The extended family as well, thank you for all the extra "Encouragement", particularly during the write-up.*

The Dilraj gang, Sander and Alexandros, also gets a particular mention, and I understand they are going to stop for a Dilraj en-route to the defence. Also, a shout-out to Lola the cat.

I would like to thank Rory and Conor for the emotional support lunches over the past few years. Marcus and Donal for the trips to Gino's. The Madem Bookclub, I would like to point out that I managed not to mention AI or machine learning throughout the entire thesis. The rest of my non-Cork friends for their support and encouragement.

Chapter 1

A background to index-patterned lasers

1.1 Introduction

Optoelectronics is a rapidly growing industry with several challenges. First, there is the continuous exponential growth in the demand for telecommunications data, which is projected to continue into the future. An exponential increase in transmitted data also means an exponential increase in power consumption. In Ireland in 2022, 18% of the electricity produced was consumed by data centres [1], with a significant percentage of the power used just for cooling for wavelength stability [2, 3]. The increase in data leads to an increase in demand for higher performance optoelectronic components. There are also many new areas for optoelectronics, which further increases demand, e.g., metrology [4], light distance and range finding (LiDAR) [5], and optical computing [6, 7]. Each of these sectors would benefit from cost reduction, particularly if one could be achieved similar to that of the complementary metal-oxide-semiconductor transistor. This would make optoelectronic components feasible in many more products, especially consumer-level ones with small manufacturing cost margins.

Our research looks at frequency control of Fabry-Pérot lasers by index-patterning of the device cavity. Although our research examines these devices from a fundamental 1D approach, it answers many questions about device operation that will be useful for the immediate development of index-patterned lasers.

This chapter covers the background to the index-patterned device and discusses where it could fit into the developing optoelectronics industry. Sec. 1.2 gives a brief overview of the device and the current methods used for its design. Sec. 1.3 analyses the state-of-the-art in terms of index-patterned lasers and the areas of optoelectronics in which it could be used in the near to medium term (~ 5 years). Sec. 1.4 summarises the goals of this thesis and has a synopsis of the chapters.

1.2 Overview of the single-frequency index-patterned laser

Single-frequency semiconductor lasers allow for high-volume data transmission. The high-frequency and -purity of the light facilitates fast modulation. They can also emit light at at the low optical loss windows for fibre-optic glass, facilitating data transmission over long distances [8]. The index-patterned laser is a single-frequency edge-emitting semiconductor laser. It is typically made by etching a sequence of slots into the waveguide ridge of a Fabry-Pérot cavity; hence it is also known as a slotted Fabry-Pérot (SFP) laser. The slot reduces the refractive index locally, as the light in the cavity extends into the air gap in the slot. The index-patterned grating can be designed to favour one Fabry-Pérot mode for lasing, creating a single-frequency laser from a multi-mode cavity. Modes are set wavelengths supported by the cavity resonances. The distance between the slots and the cavity facets is a key aspect of performance and yield, since it is impossible to control to the nanometre scale required to interact with the wave at a specific phase. Index-patterned gratings are applicable to any typical device length and wavelength. The perturbations do not have to be slots; any controlled reduction in the refractive index for a known length of cavity will suffice.

Fig. 1.1 is an outline of the index-patterned laser that includes some of its vertical structure detail. The diagram shows the light in the cavity extending into, and interacting with, the slots in the ridge. Most of the mode energy is contained between the cladding layers, which means that the Fabry-Pérot mode is perturbed by the slots. The cladding layers have a lower refractive index to vertically confine light to the gain section. The gain section is the semiconductor layers that generate the light in the laser. In our devices, the gain section is quantum well based. Quantum wells are nanometre-thickness layers that confine the carriers in a semiconductor for efficient recombination and light emission. The carriers in a semiconductor material are electrons and holes. A hole is the absence of an electron in the structure.

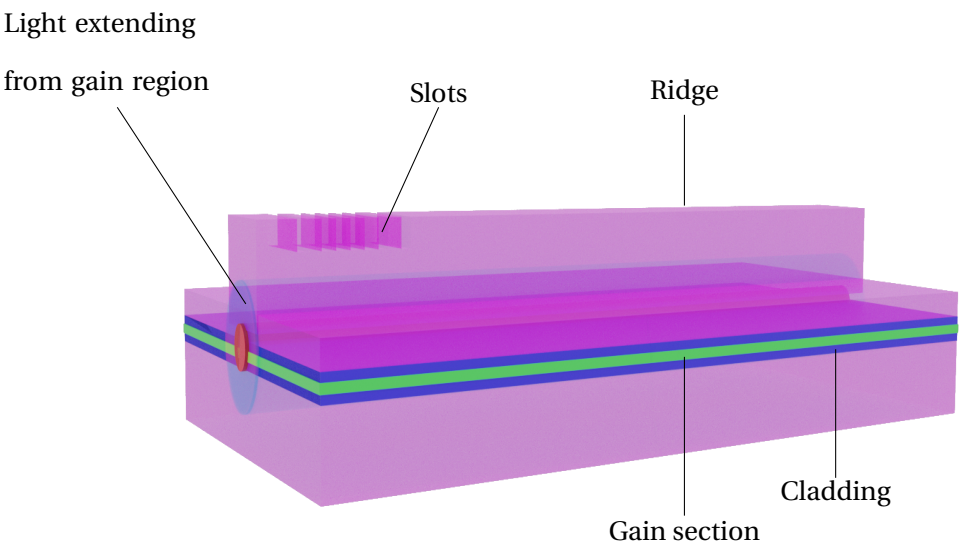


FIGURE 1.1: Diagram of the general structure of an index-patterned Fabry-Pérot laser. The gain section contains both quantum wells and barriers to contain them.

Fig. 1.2 [9] shows scanning electron microscope (SEM) images of an index-patterned laser, similar to the device we use. Panel a) has a top-down image centred on the grating structure of the device, panel b) shows a waveguide slot perturbation, and panel c) an in-plane view of a slot in a ridge.

The index-patterned laser can be made with a high side-mode suppression ratio (SMSR) (> 50 dB) [10]. SMSR is the ratio of the power in the lasing mode to the next-highest mode power in the device spectrum. They can be made to have a low-linewidth ($100-400$ kHz) [11, 12]. Linewidth is the full width at half-maximum (FWHM) frequency span of the lasing mode. They can be made with high output power (> 200 mW) [4]. Any of the power, linewidth, or SMSR parameters can be enhanced by changing the cavity design. For increased power, you have a longer and wider cavity. For a lower linewidth, increase the cavity length. For increased SMSR, you add additional slots. However, there is a trade-off for each of these parameters, particularly in terms of slots introducing optical loss. Much of the focus of our research will be on improving the SMSR of the device while keeping the number of slots in the cavity constant. Device wavelength can be tuned by changing the refractive index of the cavity, particularly the contrast of the refractive index steps in the grating. However, our research is based on devices operating at one set wavelength [13, 14].

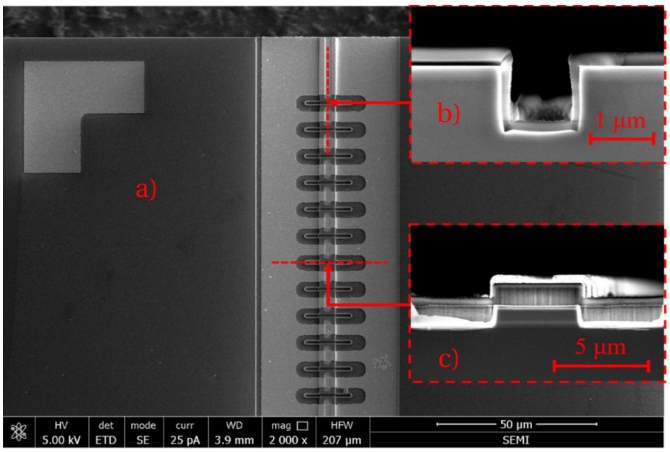


FIGURE 1.2: SEM images of an index-patterned laser device [9], a) top-down view of grating, b) slot profile, c) in-plane view of ridge slot.

Four general approaches have been used to design index-patterned gratings. The initial approach was based on a sub-cavity model of the grating, i.e., the perturbations create a system of interlinked weak Fabry-Pérot cavities within the device [15, 16, 17, 18]. This approach captures the physics of the device well, but does not prescribe the position of slots beyond having them at points of resonance with the chosen mode; iterative design methods have been used to overcome this. The Bragg equations can also be used [19], setting the pitch of the grating for mode selection. This method does not capture reflections between the grating and the Fabry-Pérot facets naturally and is often used as a starting point for an iterative numerical optimisation routine [20]. There are also purely numerical approaches [21, 22, 23]. Each of these approaches can develop effective gratings; however, the sub-cavity and Bragg approach have a limited number of positions that slots can be placed in, and numerical approaches can often develop seemingly random gratings whose design principles are difficult to understand.

The approach we use is based on the Fourier methods reported in Ref. [24]. It uses weighting functions to control the density of slots along the cavity for design and is an extension of the sub-cavity model approach. We treat the laser cavity electromagnetic field (EM-field) modes as ideal plane waves around a selected single mode [25, 26]. Changing the weighting function changes the slot distribution and hence the modal envelope of the spectrum. We can move forward and back between the cavity real-space structure and the wavelength spectrum using Fourier transforms. We use index perturbations in the grating and, therefore, just the primary reflections between the perturbations and the cavity facets for the Fourier transform, ignoring reflections between the perturbations.

The iterative numerical approaches are likely to give the best device results, compared to our Fourier-based method, given the computer's ability to search grating parameters to maximise performance. The goal of our research is to analyse how making specific changes to an index-patterned laser cavity changes the device spectrum and to draw conclusions about how the device operates from this. Although the Fourier approach does not necessarily generate the highest performance gratings, the fact that it is based on simple analytical equations makes the results easier to interpret and calculations quick to make. The Fourier method does not exclude the use of numerical optimisation routines after the initial grating design; however, this is beyond the scope of our research. We will use the Fourier approach to design gratings for real devices to compare with the theoretical results.

A major challenge to the continued development of the photonics industry is the manufacturing cost. Very low-cost mass-produced photonic chips would open up many new possibilities for the industry, e.g., environment sensors and affordable virtual reality headsets. The index-patterned laser is a simple device, which does not require many more manufacturing steps than a Fabry-Pérot laser [27, 28, 29, 30]. As the slot sizes can be relatively large ($\sim 1\,\mu m$), an index-patterned grating can be made using photolithography [31, 32], which is a low-cost process. Index-patterned lasers avoid using regrowth, which grows layers of semiconductor material on a wafer after etching and is expensive. The index-patterned grating is high-order. Grating order is the number of half-wavelengths between repetitions of the refractive index step layers.

Gratings in competing edge-emitting lasers are mostly made with Bragg mirrors, using regrowth. Bragg mirrors are ideally first-order gratings, i.e., a stack of quarter-wavelength thickness layers (~ 120 nm at 1550 nm) of contrasting refractive index. Structures of this size require E-beam etching, which is more expensive than photolithography. First-order gratings are more difficult to make [33, 34, 35], particularly for short-wavelength devices [36, 37]. Regrowth also creates interfaces of contrasting semiconductor materials that are susceptible to optical loss, heating, and failure [38]. The size of the refractive index step layers also makes them more delicate structures in terms of the reliability of the device [27].

1.3 The state-of-the-art in index-patterned lasers

The index-patterned laser is uniquely positioned in terms of the development of silicon photonics. Silicon is a low-cost material with low optical loss and high optical confinement, making it a good substrate to integrate with high-gain III-V materials [39, 40]. An index-patterned grating can be created by etching a silicon waveguide, and coupling the cavity to a high-gain material [37, 41]. There are emerging overlaps between index-patterned lasers and Bragg-based devices in silicon photonics. Bragg mirrors are often used as device facets to provide large reflections; an index-patterned grating could be incorporated into this configuration to improve modal selection [36]. Also, an index-patterned laser with non-perturbation slots in the waveguide would be undergoing significant Bragg reflections and could potentially be designed to work without cavity facets [42, 43].

Index-patterned lasers are useful for non-thermally controlled operation [44, 45]. The main issue with heating in laser operation is the shifting of the gain-bandwidth peak. The gain-bandwidth is the frequency range for which the gain that a mode receives is within 3 dB of the maximum spectral gain. The index-patterned laser can be designed to have strong modal selection against modes far from the selected mode ($\sim$ 50 modes), meaning the device will continue to lase on the selected mode even with a large change in the position of the gain-bandwidth peak. In the high-power laser space, lower optical loss and a wide modal selection bandwidth make the index-patterned laser an attractive option for single-frequency lasing [20, 26, 28].

Quantum dot materials have gain sites in their structures that are restricted in three dimensions to nanometres. Quantum dot devices have many qualities similar to index-patterned lasers, which could be enhanced by combining the two, i.e., they are resistant to back reflections and thermal drift, are low-linewidth, and have broadband modulation properties [46, 47, 48, 49, 50, 11, 12]. Index-patterned lasers are uniquely positioned for the development of quantum dot devices, as their gratings show potential to be able to select single modes in long-cavity devices with narrow modal spacing in the spectrum, which low-gain quantum dot devices require. Fig. 1.3 a) shows a diagram of an index-patterned grating heterogeneously integrated with quantum dot gain material. Fig. 1.3 b) and c) show SEMs of the grating structure.

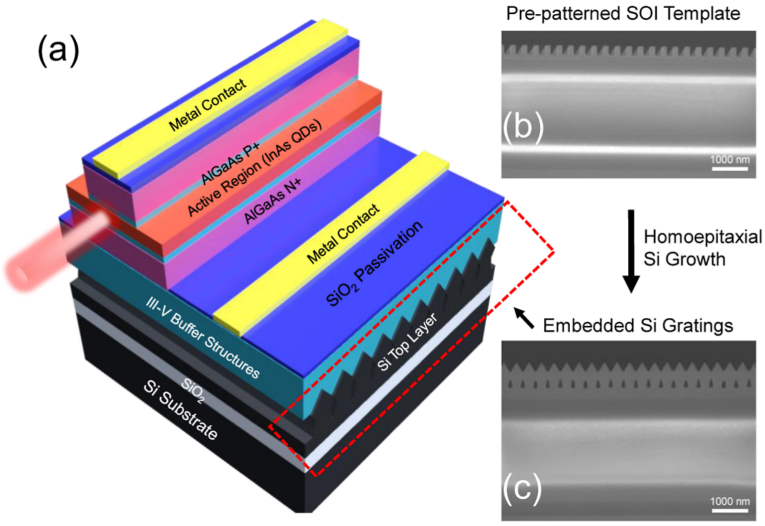


FIGURE 1.3: Example of a quantum-dot device on a silicon substrate using an index-patterned approach to single-mode lasing [37].

Many future developments for index-patterned lasers will harness more of their spectral and dynamic properties [51, 52]. For their transmission possibilities alone, optical frequency combs are a significant development in optoelectronics. Optical modes can be split into multiple carrier signals, offering an order of magnitude increase in transmission rates. There are many methods to create optical combs; one of the most straightforward ways is to modulate an index-patterned laser device [40, 53]. The index-patterned device has also recently been shown to have potential for the generation of solitons [54], the generation of random values for cryptography [55, 56], and the generation of terahertz and microwave signals [57, 58]. Each of the properties are related to the unique EM-field profiles in the cavities of index-patterned lasers. In addition to selecting a lasing mode, the Fourier approach allows for a level of control to sculpt the mode profile of the spectrum of the laser and hence the EM-field of the cavity. There is also a useful potential application of using slots or perturbations to feedback selected frequencies and phases into the cavity to suppress some of the unwanted spectral noise in the lasing mode [59].

1.4 Objectives for this thesis

The aim of this thesis is to use Fourier methods to analyse how slot position and cavity length affect the spectrum and performance of the index-patterned laser. We will look to further establish the Fourier method for modelling index-patterned lasers, as prior to this it has only been used to model ideal cavities. We aim to contrast our Fourier-modelled results with experimental SMSR and lasing wavelength. We also wish to examine the experimental impact of grating changes to: threshold current, I_{th}, single-facet output power, P, slope efficiency, η, and grating loss, α_g. The threshold current is the forward bias current of the laser required for it to begin lasing. Slope efficiency is the rate at which the output power changes as the current increases, when the device is lasing [60].

SMSR is the device parameter that we are particularly looking to improve with grating changes. The maximum SMSR is a gauge as to how well the lasing mode is selected, and the distribution of SMSR with lasing wavelength is a gauge of how resistant a grating design is to grating-facet phase effects. Improved modal selectivity will also reduce the threshold current of a laser device and improve the thermal stability of the laser. We partnered with Eblana Photonics Ltd. [61], to develop and test real devices. We used their device production runs to implement our Fourier designs.

This thesis has six following chapters. Ch. 2 will introduce the underlying physics involved in a laser device; it will describe a Fabry-Pérot cavity and the fundamentals of a scattering matrix.

Ch. 3 will introduce the engineering and mathematics involved in creating a single-mode laser, with the main focus on the index-patterned device. We will give a summary of the competing distributed feedback (DFB) and distributed Bragg reflector (DBR) laser and how the Bragg mirrors on which they are based operate. We will directly compare the DFB and the index-patterned laser for grating loss. There is also a description of the scattering matrix method algorithm that we use to benchmark our Fourier calculation.

Ch. 4 analyses our Fourier modelling results, where we changed the grating patterns in the device to see how this changed the modelled modal mirror gain threshold spectrum. We will also move the grating position in the cavity to see how this changes the mode selection.

Ch. 5 will analyse the experimental results of our designs for uncoated facets, with supplementary modelling. Here, we will see how changing the device pattern affects real device performance. We will analyse the effect of not having ideal cavity resonances on mode selection from the grating. We will also look at how optical loss varies between grating designs.

Ch. 6 will analyse the effect of applying a high-reflectivity (HR) coating to an index-patterned device cavity, both theoretically and experimentally. We will also look at the effect of HR coating on optical loss from the gratings and how slot etch depth affects the SMSR of the index-patterned laser.

Ch. 7 will provide a summary of the thesis and discuss the future directions of this research.

Chapter 2

The fundamentals of edge-emitting semiconductor lasers

2.1 Introduction

This chapter will discuss the core concepts behind the operation of edge-emitting semiconductor lasers, including a 1D model of light in a waveguide. In Sec. 2.3 we discuss semiconductor materials and particularly light generation and lasing processes in them. In Sec. 2.4 we discuss complex refractive index, i.e., real refractive index together with loss/gain. In Sec. 2.2 we will see how an abrupt change in refractive index can lead to reflectivity and how this develops to mirror loss from the cavity. Mirror loss quantifies the optical power emitted from the facets of the laser. In Sec. 2.5, we analyse the 1D wave mode solutions to the EM-field equations in waveguides. Sec. 2.6 will discuss the topic of modes in more detail. Sec. 2.7 will describe a 1D model for the Fabry-Pérot laser cavity. In Sec. 2.8 we will look at the scattering matrix, which is the basis for the semi-analytical scattering matrix method (SMM) that we use to benchmark the Fourier calculations against.

The main goal of this chapter is to describe a semiconductor laser, waveguiding in the laser cavity producing modes, that we then approximate as 1D electric field (E-field) plane waves. As optoelectronic semiconductor materials are typically non-ferromagnetic, we can assume that magnetic permeability is the same as in free-space, and therefore we only consider the E-field portion of the EM-field. The fact that we can use 1D plane waves to describe Fabry-Pérot modes allows us to use a Fourier approach. The scattering matrix is a more general tool that we also use to calculate the E-field in laser devices.

2.2 Semiconductor lasing

In solids, the atomic energy levels of constituent atoms can overlap forming bands of allowed, and bandgaps of disallowed energies for electrons. The Fermi level, E_f, is the highest occupied energy level of an electron in this band structure at absolute zero. In metals, the Fermi level lies within one of the bands. In an insulator, the Fermi level lies within a bandgap. In a semiconductor, the Fermi energy level lies in a bandgap but close enough to the band edges that electrons can be excited to transition between the bands by the ambient thermal energy [62]. We can also note that typically semiconductors consist of highly ordered crystal structures. For an electron, the bands below the Fermi level are the valence bands and above are the conduction bands. Semiconductors in the excited state, i.e., optical or electrically energised, are often described using a separate quasi-Fermi level for the valence band, E_{f_v}, and conduction band, E_{f_c}. f_v and f_c are the occupation probabilities under quasi-equilibrium conditions for the valence and conduction bands

$$f_v = \frac{1}{1+\exp\left(\frac{E_v - E_{f_v}}{k_B T}\right)}, \tag{2.1}$$

$$f_c = \frac{1}{1+\exp\left(\frac{E_c - E_{f_c}}{k_B T}\right)}. \tag{2.2}$$

E_v and E_c is the respective valence or conduction band energy, k_B is Boltzmann's constant and T is ambient temperature. ΔE_f is the difference between the quasi-Fermi levels. Without additional electrons or holes being added to the structure, i.e., in the non-excited state, the conduction band is mostly empty and the valence band is mostly full of electrons at room temperature in an n-type semiconductor.

Ambient thermal energy can excite and electron from the valence band to the conduction band, leaving an empty state in the valence band, i.e., a hole. Over time the electron will dissipate energy and fall back into the valance band, recombining with a hole. An equilibrium is established between thermal excitation and recombination. Photon generation uses a direct bandgap semiconductor. In a direct bandgap semiconductor the energy maximum of the valence and the energy minimum of the conduction band have the same momentum vector, facilitating photon interactions with carrier generation and recombination. The energy of the photon emitted is the difference of the two recombining carriers. This produces light of a frequency, f,

$$E_c - E_v = hf, \tag{2.3}$$

where h is Planck's constant. In a laser, the semiconductor material is engineered to improve the efficiency of light generation. Photon generation can be increased by bringing a region doped with excess electron donors, "n-type", beside a region doped with excess hole donors, "p-type". Fig. 2.1 a) shows such a structure, the pn homojunction. At the boundary of these two regions, a high concentration of holes and electrons will be in close proximity to each other. When a voltage is applied to the semiconductor, electrons traverse the boundary for recombination and vice-versa for holes.

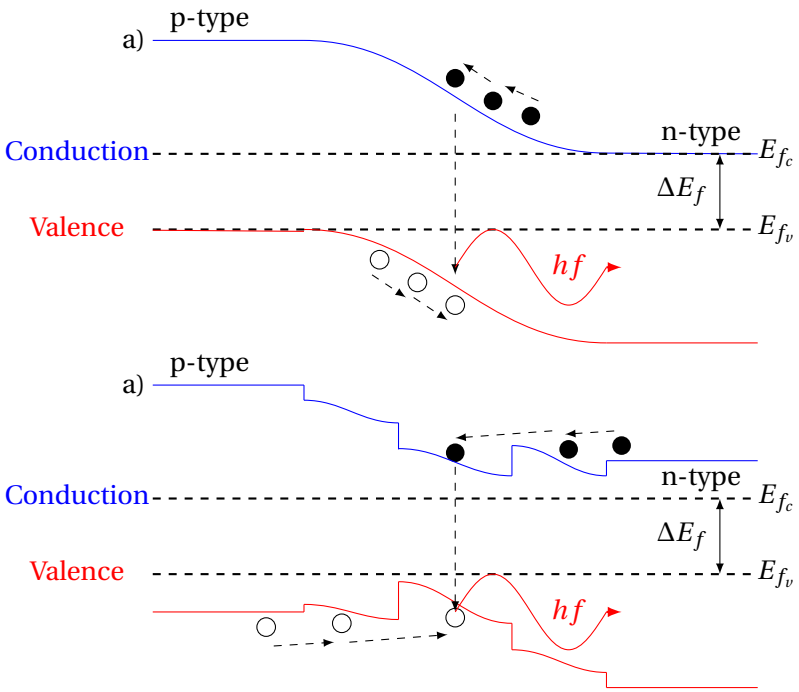


FIGURE 2.1: a) pn homojunction diode, b) separate confinement heterostructure [63].

Typically additional energy steps for carriers are added to the structure to further restrict them to a region of high concentration, Fig. 2.1. Quantum wells are the most significant of these structures. Quantum wells are thin layers on the scale of the de Broglie wavelength of the carriers in thickness, ~ 10 nm [64]. They have high energy steps to the surrounding barrier layers, Fig. 2.2 a). Confining carriers to this scale can also prevent an increase in density of states, D, with increasing energy. The density of states is the number of states a system has per unit energy. By preventing an increase in available states as voltage is increased into to the gain region of the device, Fig. 2.2 b) → c), a high concentration of carriers can be maintained. The density of states for energies in the bandgap, E_g, is zero.

Fig. 2.2 b) shows the refractive index profile of a pn separate confinement heterostructure (SCH). This consists of the refractive index for the quantum wells, the barriers and the cladding, as well as a surrounding region of graded refractive index (GRIN) to enhance the photon confinement to the gain section.

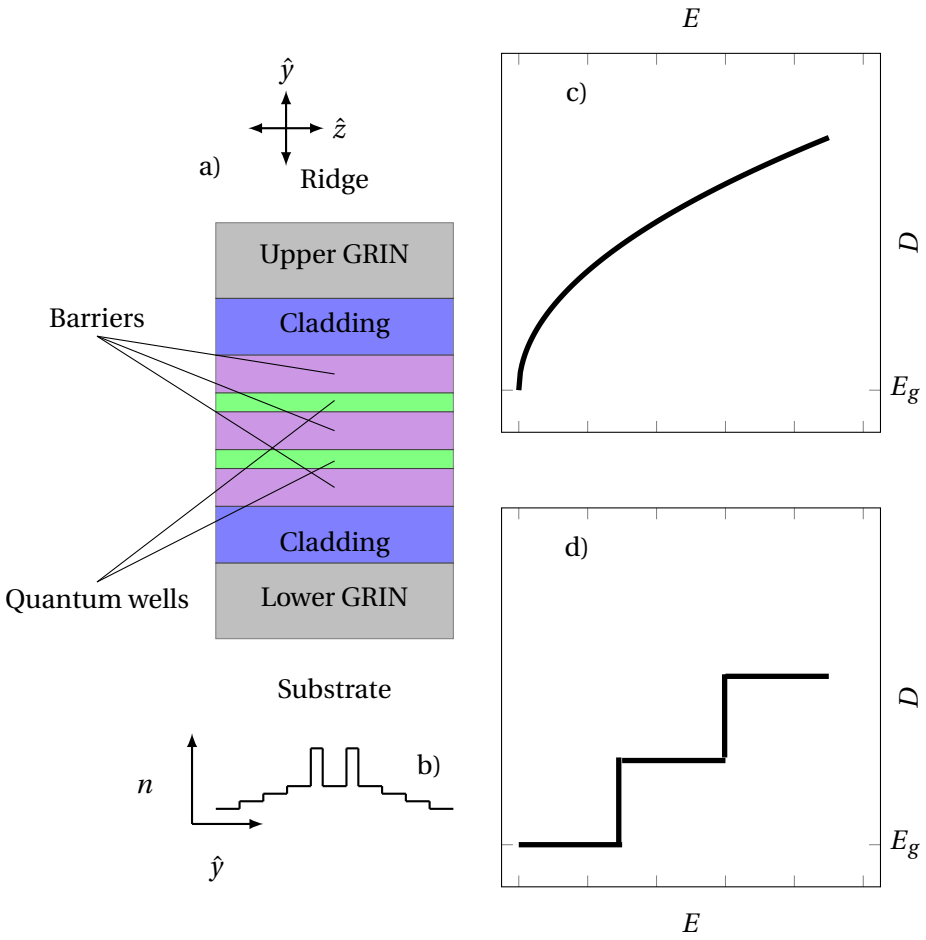


FIGURE 2.2: a) semiconductor layers around the active region of the laser, b) an example of the refractive index profile of the structure, c) density of states bulk material, d) density of states quantum wells [65].

Absorption occurs when a photon excites an electron from the valence band to the conduction band. An electron and hole can spontaneously recombine, producing a photon of random direction, phase, and frequency within the gain-bandwidth of the laser. The gain-bandwidth is the frequency range where gain is is within 3 dB of the maximum gain value. A photon can also stimulate an electron and hole into recombining, producing a photon with matching direction, phase, and frequency. Carriers can be provided for stimulated emission by applying a bias current/voltage to the semiconductor. We get net gain when

$$f_c(1-f_v) > f_v(1-f_c), \tag{2.4}$$

or alternatively

$$\Delta E_f > hf. \tag{2.5}$$

This is the Bernard-Duraffourg condition for population inversion [66]. Population inversion occurs when there is a higher population of electrons in the conduction band than the valence band in the quantum well, and is a requirement for lasing. Lasing occurs in a cavity when stimulated and spontaneous emission match the losses in the cavity. There is also a frequency/energy dependency of gain/loss due to carriers being more (or less) likely to recombine for a given photon energy, due both to the energy dependence of $f_c - f_v$.

2.3 Complex refractive index

The real, n, and imaginary, in', are the two parts of the complex refractive index, $\tilde{n}$;

$$\tilde{n} = n + in'. \tag{2.6}$$

The use of the complex refractive index allows for a straightforward calculation of the E-field vectors. The real part of refractive index quantifies variation in the rate of change of phase of a light wave in a material compared to a vacuum. The imaginary refractive index quantifies the change in amplitude as the wave travels through the material. Material gain, g, is an increase in E-field per unit length of propagation [67], and propagation loss, α_p, its decrease.

Propagation loss mostly consists of the photon energy absorbed by the material through recombination being dissipated into the semiconductor structure through vibrations called phonons, as well as scattering from the sidewalls of the waveguide. Material gain can be related to our imaginary refractive index as

$$n' = \frac{\lambda(\alpha_p - \Gamma g)}{4\pi}, \tag{2.7}$$

Γg is the gain a specific mode receives, allowing for how much it overlaps the quantum wells, Γ.

An intuitive way to think about semiconductors is to think about the negatively charged electrons in the electronic shells around the crystal structure as mass-on-spring oscillators with the positive crystal centres of the constituent atoms [68, 69]. An input optical E-field will oscillate the electrons. As each electron oscillates, it generates its own E-field, travelling in the same direction as the inbound light. Electrons in the previous path of the light are already oscillating, opposing return movement. In this way, light travels forward through the semiconductor as internal E-fields within its structure. The interaction of the light with the material slows its progress through the structure by a factor, n. Light of different frequency interacts more (or less) strongly with a material as the mass-on-spring oscillator has its own natural resonance frequencies. The change in real refractive index with frequency is known as dispersion, $n(\lambda)$.

When modelling our laser devices we ignore the effects of dispersion. The AlGaInAs gain, and InP substrate layers we experimentally develop our gratings on in Ch. 5 and Ch. 6 [29], have small dispersion effects in the 1500 → 1600 nm range [70, 71]. Including dispersion would increase the complexity of the calculation and not significantly improve its accuracy.

For the imaginary part of refractive index, gain and loss do vary significantly with wavelength in quantum well devices, so the imaginary refractive index is allowed to vary with wavelength when included. Loss/gain and refractive index are also approximated to be constant along the cavity; however, they can vary significantly in a real cavity from carrier injection, local heating, and changing optical field intensity. Although these are significant effects, we have, at least initially, chosen to study bare cavity dimensional effects, ignoring these additional material effects. The imaginary refractive index is positive value for extinction and negative for gain.

2.4 Reflectivity and mirror loss

When there is an abrupt change in refractive index, the forward and reverse fields no longer cancel between the two side-by-side electron crystal centre oscillators, meaning a portion of the E-field is returned in the reverse direction, i.e. reflected. The ratio of the amplitude of the E-field reflected at a boundary, r, can be directly related to the real refractive index of the two materials on either side of the boundary

$$r = \frac{n_1 - n_2}{n_1 + n_2}, \tag{2.8}$$

where n_1 is the real refractive index of the material in which the light is in, and n_2 is for the material it is entering. When the real refractive index is higher in the material into which the light is entering, the reflected wave undergoes a phase shift of π. This occurs because the net phase of incident, transmitted, and reflected waves must be maintained at the dielectric boundary according to Maxwell's equations [72]. We can convert amplitude reflectivity to power reflectance by squaring the value, $R = r^2$.

At the facets of the cavity, a portion of the light is reflected back into the cavity, and the rest is lost from the system. This is known as mirror or facet loss, α_f. The mirror loss per unit length of a cavity of length L is

$$\alpha_f = \frac{1}{L} \ln\left(\frac{1}{r_l r_r}\right), \tag{2.9}$$

where $r_{l/r}$ is the reflectivity of the left/right cavity facet. Mirror loss can be modified by changing the cavity length or facet reflectivities.

2.5 The waveguide

An optical waveguide is a structure that confines and allows the transmission of light with low power loss. Semiconductor materials can naturally form good optical waveguides. They can exhibit low power loss at optical frequencies and can be tailored to have a wide variation of refractive indices. This allows for large refractive index step boundaries between different material or materials and the surrounding free-space. A strip of semiconductor material can form a waveguide by containing light through total internal reflection, Fig. 2.3. The semiconductor waveguide is an important structure in our research, since cleaving facets at the end of the structure can form a Fabry-Pérot cavity for lasing, Sec. 2.7 and Fig. 2.3.

For light to be contained efficiently in a waveguide, it forms a standing wave that meets the boundary conditions imposed by the waveguide. The boundary is the sharp refractive index step formed at the edge of the waveguide, $\hat{x}$ and $\hat{y}$ in Fig. 2.3. In an ideal, totally confining waveguide, the boundary conditions are [73, 74]

$$\hat{E}^{||} = 0, \tag{2.10}$$

$$\hat{H}^{\perp} = 0, \tag{2.11}$$

where $\hat{E}^{||}$ is the E-field vector ($\hat{E}$) parallel to the boundary and $\hat{H}^{\perp}$ is the magnetic field strength vector ($\hat{H}$) perpendicular to the boundary.

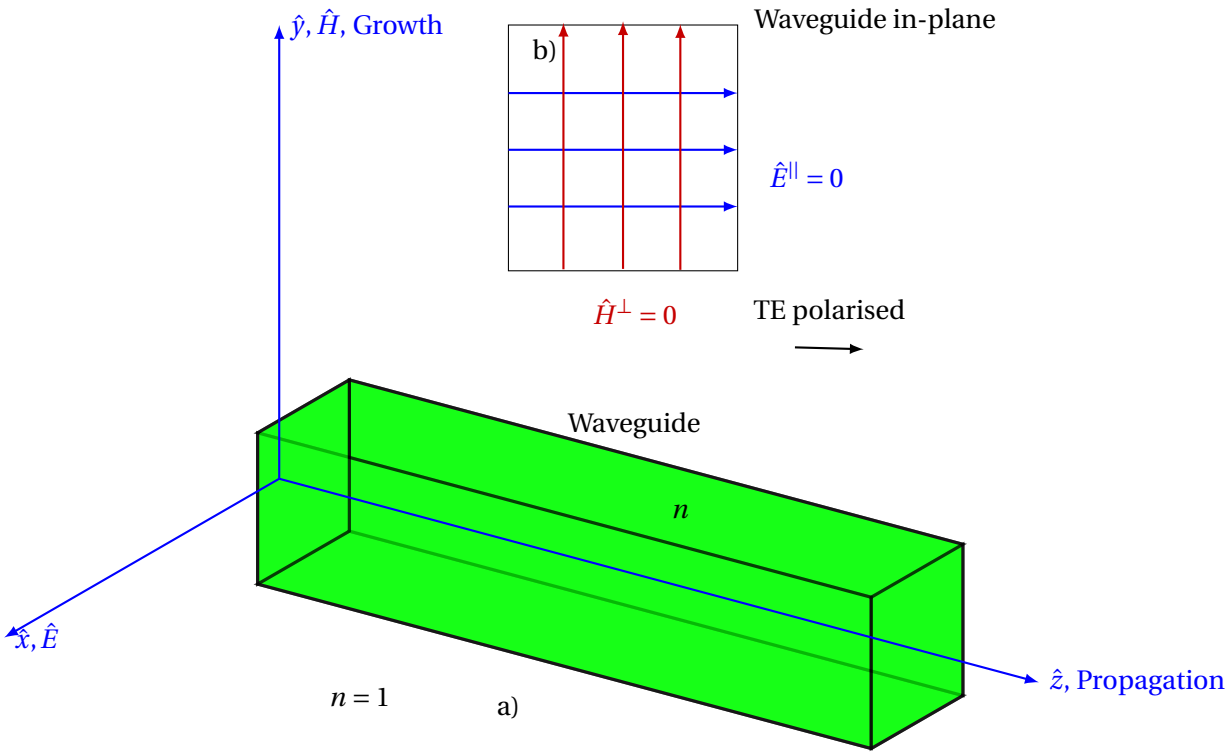


FIGURE 2.3: a) Coordinate system used in this thesis with a 1D sinusoidal E-field to approximate a mode in the waveguide. E-field oscillates transversely to the growth direction of the semiconductor, i.e. a TE mode. Semiconductor layers extend in the $\hat{x}$ direction. b) In-plane TE mode meeting the boundary conditions.

E-fields are described by Maxwell's equations. Maxwell's equations are accurate in what they describe, but, as coupled partial differential equations, they are computationally difficult to calculate. This is particularly true for high-frequency optical waves in micrometre-scale structures, where many calculation steps are required. Using boundary conditions, the E-field in a cavity can be distilled into a superposition of plane waves. Maxwell's equations for EM-fields in a dielectric material are [73, 75]

$$\nabla \times \hat{E} = -\mu_0 \frac{\partial \hat{H}}{\partial t}, \tag{2.12}$$

$$\nabla \times \hat{H} = \hat{J} + \tilde{n}^2 \epsilon_0 \frac{\partial \hat{E}}{\partial t}, \tag{2.13}$$

$$\nabla . \hat{E} = \frac{\rho}{\epsilon_0}, \tag{2.14}$$

$$\nabla . \hat{H} = 0, \tag{2.15}$$

ϵ_0 and μ_0 are the permittivity and permeability of free-space, respectively; $\hat{J}$ is the current density and ρ is the charge density. Assuming a perfect dielectric, the current density and charge density can be set to zero.

To further simplify, we assume our waveguide is surrounded by free-space on all sides, $n = 1$ in Fig. 2.3. In a real device, this is not the case, where a waveguide is formed by a ridge on a substrate semiconductor. Applying the curl operator to Eq. 2.12

$$\nabla \times (\nabla \times \hat{E}) = -\mu_0 \nabla \times \left(\frac{\partial \hat{H}}{\partial t} \right) = -\mu_0 \tilde{n}^2 \epsilon_0 \frac{\partial^2 \hat{E}}{\partial t^2}. \tag{2.16}$$

To simplify Eq. 2.16 further, we can use the vector identity $\nabla \times (\nabla \times \hat{A}) = \nabla.(\nabla.\hat{A}) - \nabla^2 \hat{A}$, where $\hat{A}$ is any vector. This gives us

$$\nabla^2 \hat{E} = \mu_0 \epsilon_0 \tilde{n}^2 \frac{\partial^2 \hat{E}}{\partial t^2}, \tag{2.17}$$

or for a TE polarised wave travelling parallel to the $\hat{z}$-axis

$$\frac{\partial^2 \hat{E}}{\partial z^2} = \frac{\tilde{n}^2}{c^2} \frac{\partial^2 \hat{E}}{\partial t^2}, \tag{2.18}$$

where c is the speed of light and $c = \frac{1}{\sqrt{\epsilon_0 \mu_0}}$. This meets the wave equation criteria, which means that we can use a plane wave solution to this equation to describe the E-field oscillations [64]

$$\hat{E}(z,t) = \hat{E}_0 \exp\left(i(\tilde{n}kz - \omega t)\right), \tag{2.19}$$

where $\hat{E}(z,t)$ is the E-field vector at the point z at time t, $\hat{E}_0$ is the initial E-field vector at the origin ($z = 0$ and $t = 0$), k is the free-space wavenumber $\left(k = \frac{2\pi}{\lambda}\right.$, where λ is the free-space wavelength$\left.\right)$, and ω is the radial frequency of light $\left(\omega = \frac{2\pi c}{\lambda}\right)$.

Another useful simplification is that our study of laser devices only involves their operation in the steady-state, which means that we can neglect the time dependency of the wave and only allow it to oscillate in $\hat{z}$

$$\hat{E}(z) = \hat{E}_0 \exp(i\tilde{n}kz). \tag{2.20}$$

We can separate the real and imaginary parts in Eq. 2.20, highlighting the oscillating component and the gain/loss component

$$\hat{E}(z) = \hat{E}_0 \exp(inkz) \exp\left(-n'kz\right). \tag{2.21}$$

The 1D plane wave equation can be used to model the index-patterned device; using the complex refractive index to include loss/gain and real refractive index changes to model the device structure. In our modelling we will treat modes as 1D plane wave solutions to the E-field of the cavity.

2.6 Modes

In terms of a laser cavity, modes form both longitudinally and transversely, and we will discuss the two aspects separately. Modes can be thought of as allowed energy states or wavelengths of the cavity resonator [76]. Ideally, a mode is orthogonal to the other modes in the cavity, i.e., they are independent of each other [77]. This is an important justification for using the Fourier-transform approach to model the resonator.

2.6.1 Longitudinal

For modes to form in the longitudinal extent, $\hat{z}$ in Fig. 2.3, the light wave traverses the length of the cavity and reflects under phase inversion at the facet. When a wave has an antinode at both facets, it is preferred over a wave that does not. This creates the half-wave resonance condition for the allowed modes

$$\lambda_m = \frac{2Ln}{m}, \tag{2.22}$$

where m is the mode number and λ_m is the free-space wavelength of the mode. This equation also demonstrates the dependence of lasing wavelength on cavity refractive index. The forward and reverse waves will have a π phase separation between them, as there must be a 2π phase shift after one whole round trip for a mode to form. The mode is the sum of the forward and reverse travelling E-field waves. As longitudinal modes can form over the cavity length, which is many times the wavelength of the light, they can be approximated relatively accurately by a plane wave. In our model, there is one standing wave for each mode in the resonator cavity. In real devices, there is a narrow frequency band of wavelengths due to the span of wavelengths the resonator cavity can maintain around the mode central frequency, i.e., cold-cavity linewidth.

Modes are not constantly spaced in terms of wavelength [78]

$$\Delta\lambda = \frac{\lambda^2}{2Ln(\lambda)}, \tag{2.23}$$

but are in terms of energy. The energy spacing between two modes in the cavity, $\Delta E_{\Delta p}$, can be calculated by multiplying the minimum energy of a resonator mode, $\frac{hc}{2nL}$, by the integer difference, Δp, between the two modes

$$\Delta E_{\Delta p} = \Delta p \frac{hc}{2Ln}. \tag{2.24}$$

When a mode receives sufficient gain, it lases; changing the structure of the mode. Coherent stimulated emission interactions begin to dominate over incoherent spontaneous emission in the cavity, and the mode narrows. The increase in gain with carrier concentration also causes an exponential increase in the amplitude of the mode over the background spontaneous emission in the spectrum. A mode couples two systems together; the E-fields of the oscillating electrons in the gain material and the E-field of the light in the optical cavity [68, 79].

2.6.2 Transverse

Optical cavities also have modal components in the transverse $\hat{x}$ and $\hat{y}$ directions, Fig. 2.3. They tend to be best described by EM-field distributions, as they are spatially restricted [74], but still have the half-wave resonance condition. The defined waveguide structure gives the transverse modes of the waveguide well-defined patterns, intensity profiles, and consistent phase. [75].

Vertically, $\hat{y}$ in Fig. 2.3, it is mostly the semiconductor layers, with many refractive index boundaries for reflection, that offer tight confinement. As the gain section in a quantum well-based device is narrow (< 100 nm) [38], good overlap between the lasing mode and the quantum wells is vital for operation. In the ridge waveguide structure on which our devices will be experimentally implemented, semiconductor material is etched away on either side of the cavity, leaving the waveguide surrounded by free-space for lateral mode confinement. The lateral structure does not have the same spatial restrictions and does not require the same level of confinement as the vertical structure. The lateral structure also provides some confinement for the vertical extent of the mode.

Most optoelectronic devices are designed to have one spatial mode. This is usually the primary transverse electric (TE) mode, where the E-field oscillates transverse to the semiconductor growth direction, $\hat{x}$ in Fig. 2.3. In the transverse magnetic (TM) mode, the E-field oscillations are in-line with the growth direction of the semiconductor layers, $\hat{y}$ in Fig. 2.3 and Fig. 2.2. Devices are more likely to be TE, as the gain the TE mode receives tends to be higher than that of the TM in lattice-matched and compressively strained quantum wells, and also the TE mode reflects more efficiently at the cavity facets [75, 80].

We can handle variations in the transverse structure of the device by changing the refractive index in our model. This is known as the effective refractive index and accounts for the change in complex refractive index a mode experiences in a cavity due to the transverse mode shape in the cavity waveguide. A large portion of this effect is determined by how much the mode interacts with the free-space around the waveguide. This allows us to compress the 3D-space of the waveguide to 1D. Effective refractive index changes in the structure/interface can be calculated with 2D or 3D modelling software or direct measurements of real devices.

2.7 The Fabry-Pérot laser cavity model

Index-patterned lasers are created by perturbing the modes in a Fabry-Pérot cavity laser. A Fabry-Pérot resonator is formed by two reflecting surfaces directly opposite each other and a relatively lossless medium between them. Our laser device consists of a strip of waveguide with the refractive index step on each end providing the reflective surfaces. The waveguide structure acts as a confining medium for light in the $\hat{x}$ and $\hat{y}$ directions.

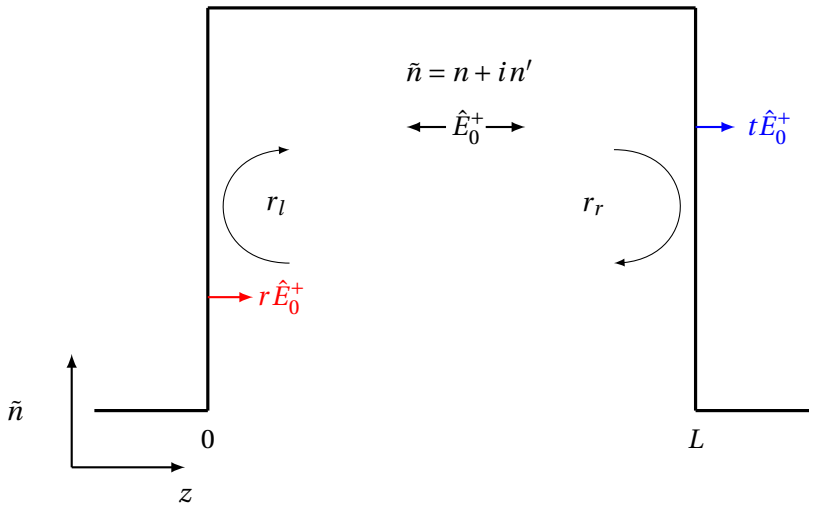


FIGURE 2.4: Diagram of a Fabry-Pérot resonator, showing a cavity of set complex refractive index, spontaneous emission of a E-field (black arrows), reflectivity feedback (red arrow), and emission from the cavity (blue arrow).

We can see in Fig. 2.4 a diagram of our model for a Fabry-Pérot cavity laser, showing a constant complex refractive index along the cavity. The total loss per unit length, α, that the E-field can experience in the cavity is the sum of the propagation loss and the mirror loss

$$\alpha = \alpha_p + \alpha_f. \tag{2.25}$$

For a Fabry-Pérot cavity to lase, sufficient gain must be applied to overcome the optical losses of the cavity.

In a laser cavity, the mode spacing is inversely proportional to the cavity length, Eq. 2.22. In short vertical-cavity lasers, mode spacing can be sufficiently large for only one mode to be at a high spectral-gain wavelength for lasing. In edge-emitting lasers, with relatively long cavities, the mode spacing is narrow, resulting in several modes lasing. To overcome this, typically a wavelength dependence for r is developed in the cavity using a grating, i.e., mirror reflectivity. In the index-patterned laser we do this by changing the effective refractive index of small sections of a Fabry-Pérot laser cavity, to change the reflectivity the Fabry-Pérot modes experience.

2.8 The scattering matrix

To model a single-mode laser, complicated 1D optical cavities containing gratings can be broken down into a series of sub-cavities. We model loss/gain, reflection, and phase change is the sub-cavity using a complex plane, Fig. 2.5.

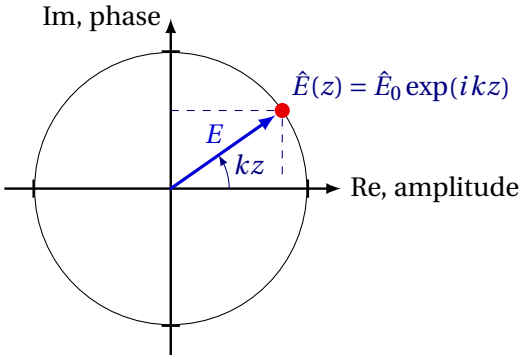


FIGURE 2.5: Complex plane for an E-field plane wave.

Each sub-cavity can be mathematically represented by a 2×2 matrix. Each element in the matrix multiplies the input and output travelling wave vectors, Fig. 2.6 and Eq. 2.26. A basic optical unit, e.g., a section of waveguide, can be viewed as three cascaded scattering blocks, two dielectric interfaces at either end, and one transmission line between, Fig. 2.6.

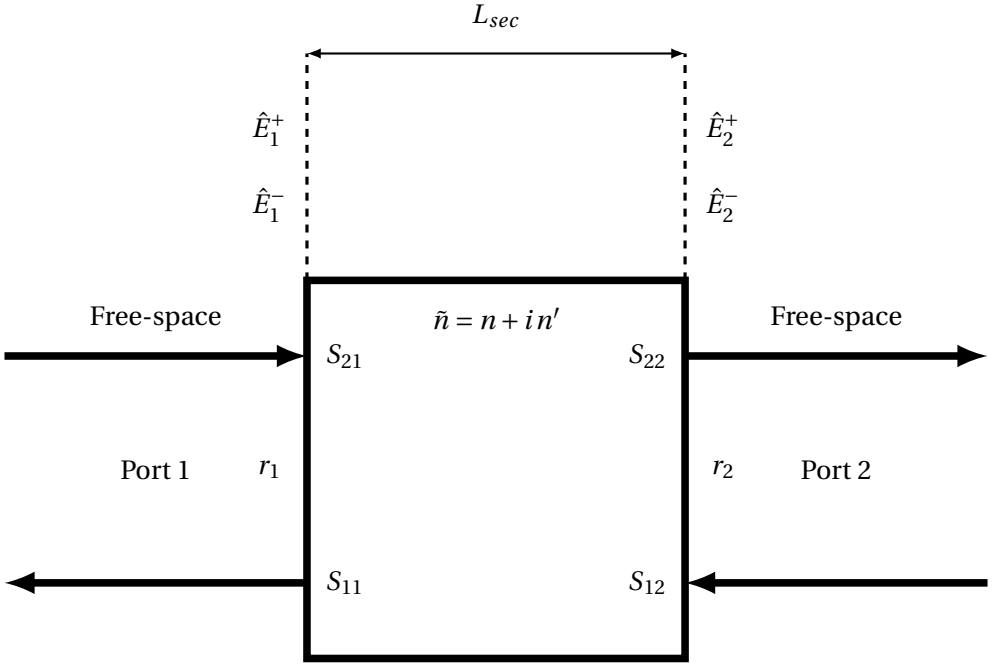


FIGURE 2.6: Scattering matrix model for one optical unit, with its matrix representation in Eq. 2.26.

There are several ways to mathematically formulate this idea. The scattering matrix is the particular formulation that we use. The competing transfer matrix approach becomes numerically unstable for large systems in the presence of evanescent modes due to the coexistence of exponentially decaying and growing waves [81]. The scattering matrix relates the incoming and outgoing E-field vectors [64]

$$\begin{bmatrix} \hat{E}_1^- \\ \hat{E}_2^+ \end{bmatrix} = \begin{bmatrix} S_{11} & S_{12} \\ S_{21} & S_{22} \end{bmatrix} \begin{bmatrix} \hat{E}_1^+ \\ \hat{E}_2^- \end{bmatrix}, \tag{2.26}$$

where $\hat{E}_1^+$ is the complex value of an input E-field vector, $\hat{E}_1^-$ is the reflected value, E_2^+ is the transmitted value and $\hat{E}_2^-$ is an input value at the other end of the structure, often set to zero.

Calculating each layer in a background free-space, along with relating the external E-field vectors on each side of the structure, makes the layers symmetric. This means that the loss/gain or reflection experienced by the forward and reverse propagating waves in a section of waveguide are the same [82], halving the number of calculations required. For the value returned from the left input of the scattering block ($\hat{E}_1^-$)

$$S_{11} = -r_1 + \frac{t_1^2 r_2 \exp(-2i\tilde{n}kL_{sec})}{1 - r_1 r_2 \exp(-2i\tilde{n}kL_{sec})}, \tag{2.27}$$

where $t = \sqrt{1-r^2}$, and L_{sec} is the length of the waveguide section. Using the symmetry of our formulation

$$S_{11} = S_{22}. \tag{2.28}$$

For the transmitted E-field through the block ($\hat{E}_2^+$)

$$S_{21} = \frac{t_1 t_2 \exp(-i\tilde{n}kL_{sec})}{1 - r_1 r_2 \exp(-2i\tilde{n}kL_{sec})}, \tag{2.29}$$

and, using symmetry

$$S_{21} = S_{12}. \tag{2.30}$$

We can then multiply the scattering matrices of a sequence of optical sections to model complicated optical structures. This allows for controlled design and study.

2.9 Discussion

Initially we looked at the processes for light generation in a semiconductor and how light interacting with a semiconductor material slows its progress. We then saw how light confined in a waveguide can form 1D waves from Maxwell's equations, and how these 1D waves are the basis for plane wave modes in an optical cavity. Most of the light in a cavity is in a frequency space localised around the mode centres. If we can calculate what happens to light around the mode centres ($\pm \sim 1$ pm), we will understand what happens to most of the light in the cavity. This will significantly reduce the number of calculations required to model the E-field of a cavity and simplify our analysis of the index-patterned structures. The Fourier analysis approach is based on the modification of the plane wave modes of the Fabry-Pérot resonator. We also saw how the concepts of plane waves in the Fabry-Pérot cavity can be extended to describe more complex optical structures using the scattering matrix.

It is important to note that we are missing some of the physical details of waveguide structures by reducing the 3D EM-field to 1D plane waves. We only partially capture these effects with an effective refractive index. There are advantages to 1D modelling, as it allows the study of specific effects of changing refractive index layers in the $\hat{z}$ direction without the added complexity and computation time of changing structure in the $\hat{x}$ and $\hat{y}$ directions. 1D calculations are orders of magnitude faster than 2D/3D calculations, particularly when we base our calculations on mode centres. This allows for a much greater variety of structures to be analysed in our modelling.

In the next chapter, we develop our Fourier model for index-patterned lasers using plane wave modes. We will also develop the SMM modelling approach, which multiplies together individual scattering matrices to model complete optical structures. We will compare both methods, and the SMM will be used to analyse Bragg mirror-based devices.

Chapter 3

Single-frequency lasers

3.1 Introduction

The first half of this chapter will describe both how the index-patterned laser works and our Fourier approach to modelling it. In Sec. 3.2.1 we explain our reflection model for an individual slot. In Sec. 3.2.2 we describe how positioning a slot in a waveguide can be used to select a lasing wavelength. In Sec. 3.2.3 we describe our design approach, where we use weighting functions to control the density of slots along the cavity. In Sec. 3.2.4 we will describe the Fourier mirror threshold gain calculation. In Sec. 3.2.5 we analyse the importance of the slot-width on the mirror gain spectrum using the Fourier model. Sec. 3.3 will describe our scattering matrix method (SMM) model and the algorithm we use to calculate the modal mirror threshold spectrum.

In the second half of the chapter, we describe how competing single-frequency edge-emitting devices function. Sec. 3.4 will describe the principle of operation of Bragg mirrors. We then analyse how laser types based on Bragg mirrors generate single lasing modes. In Sec. 3.4.2 we discuss the distributed feedback laser (DFB), and in Sec. 3.4.3 the distributed Bragg reflector (DBR) laser.

For a laser to operate on one set mode, there has to be more optical power in that mode than in other competing modes. In edge-emitting lasers, this is typically done by reflecting additional light at the chosen wavelength back into the cavity using the contra-directional light coupling of gratings. To analyse index-patterned devices, we mainly use Fourier-based methods derived by considering the modes of a Fabry-Pérot cavity as discrete plane waves to model the spectral effects of changing grating and device geometries. The fact that the approach is 1D, allows us to analyse the effect of changing perturbation position in relation to the cavity facets without additional cavity parameters obscuring results and conclusions.

We will see how the physics and mathematics from Ch. 2 can be applied to develop an index-patterned grating and to analyse competing laser types. The outcome of this chapter is to understand how the index-patterned laser works and how it is different from other edge-emitting lasers.

3.2 The index-patterned laser

Index-patterned lasers are typically made from a Fabry-Pérot cavity with a number of partially reflecting internal slots. The slots are introduced by etching into the top of the laser waveguide [24, 43, 83]. Here, we will detail how slots can be introduced to achieve single-mode lasing for a specified free-space wavelength, λ_0. It is important to note that we must lase on the closest allowed mode, m_0, of the Fabry-Pérot resonator, including the mode phase shift introduced by the grating perturbations. In a real device, this mode must also be near the spectral peak of the gain-bandwidth.

The goal of the perturbations is to couple a small percentage of the m_0 mode's forward travelling wave energy into its reverse travelling wave and to minimise coupling for unselected modes. Multiple slots must be positioned correctly to effectively select a single mode. That is, when the slots are all positioned to be at the peaks of the forward travelling wave of the E-field of the m_0 mode, the m_0 mode is more strongly reflected and has a lower mirror threshold loss than the unselected modes.

Placing slots at points of resonance with the selected mode can excite additional modes, as well as m_0. As the mode number is high, modes close to m_0 will have similar E-field distributions along the cavity, and are susceptible to excitation. To reduce the selection of these neighbouring modes, we use design functions to control the density of the slots along the cavity. This gives an overarching pattern to the slots and the gain threshold spectrum. We will describe how we implement these design functions. We will also show how a modal mirror gain threshold spectrum can be calculated by considering the first-order reflections of plane waves in a Fabry-Pérot cavity.

3.2.1 The slot

Photolithography and chemical etching are often used to create the waveguide slots, as this is the most cost-effective approach. E-beam patterning can also be used; it is more accurate with slot dimensions and positioning; however, it is also more expensive.

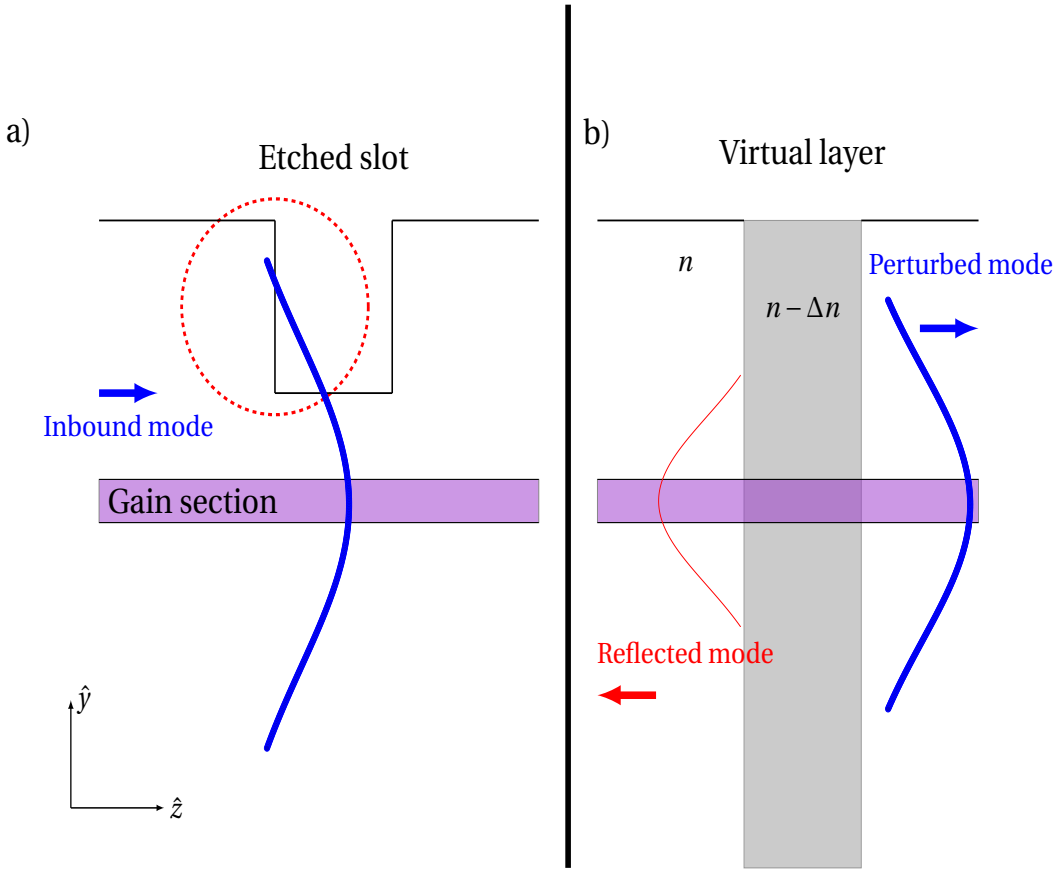


FIGURE 3.1: a) relief of a slot in an index-patterned waveguide, showing schematically how the incident mode tails extend into free-space above the slot (red circle). b) virtual layer approximation to this process that the Fourier model uses. A small amount of the mode is reflected by the slot and most of the mode is transmitted as we move from left to right in the diagram.

The principle of reflection for a slot in the waveguide in our model is that the refractive index of the etched section decreases as the mode tail interacts with the free-space in the slot, Fig. 3.1 a). The closer the slot is etched to the quantum wells, the greater the reduction in refractive index, but also the greater the optical loss. Optical power is radiated out of the waveguide as a result of reduced optical confinement and scattering by the slot.

To model this process in 1D we use a virtual layer of reduced effective refractive index, Fig. 3.1 b). A small portion of the mode energy is reflected by the abrupt change in the refractive index, and most of the mode energy is transmitted through the slot. However, in-depth investigation has shown that the modal mismatch between the etched and unetched waveguide sections is what generates most of the reflection [84], not the abrupt 1D change in refractive index. We do not consider the loss of the slot in the Fourier model. Loss is included when we convert mode selection into SMSR in Sec. 5.2.1 and Sec. 6.2.1.

3.2.2 Slot positioning for lasing mode enhancement

To study how a slot can enhance m_0 selectivity, we consider a Fabry-Pérot laser cavity with facets of equal reflectivity amplitude, r. In our model we take the operation point of our laser as the steady-state, where the gain is to equal the sum of all losses in the cavity

$$\alpha_f = G - \alpha_p, \tag{3.1}$$

where G is the cavity threshold gain. As we use the Fourier calculation to particularly study changes in modal mirror loss with wavelength, we exclude propagation losses and the spectral gain-bandwidth effects in our initial calculation. These can be added separately when required, as in Sec. 5.2.1 and Sec. 6.2.1. This gives a gain threshold condition for the cavity of

$$r^2 \exp(\alpha_f L) = 1. \tag{3.2}$$

In the absence of any refractive index perturbations, the maximum amplitudes of the right (left) E-fields at the gain threshold steady-state, $\hat{E}_r$ ($\hat{E}_l$), vary with position in the cavity ϵL as

$$\hat{E}_r(\epsilon L) = \hat{E}_0 \exp\left[\frac{\alpha_f}{2}\left(\frac{1}{2}+\epsilon\right)L\right], \tag{3.3}$$

$$\hat{E}_l(\epsilon L) = \hat{E}_0 \exp\left[\frac{\alpha_f}{2}\left(\frac{1}{2}-\epsilon\right)L\right], \tag{3.4}$$

where ϵ is a unitless ratio of position in the cavity; $\epsilon = 0$ at the centre and $\epsilon = \pm\frac{1}{2}$ at the facets. As we only consider mirror losses, we have an E-field amplitude change with position that exactly matches what is required to equal mirror loss in our Fourier calculation.

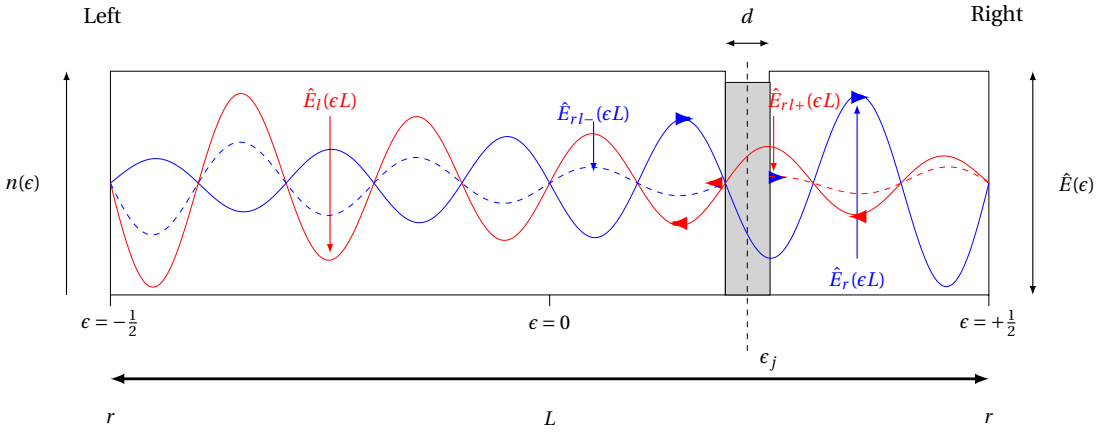


FIGURE 3.2: Plane wave reflections due to an ideal refractive index perturbation of one quarter-wavelength in a Fabry-Pérot cavity. The (red) solid line is the right (left) travelling portion of the mode, and the blue (red) dashed line its left (right) travelling reflection. The red line sinusoid incident on the left face of the perturbation is a whole number of half-wavelengths from the left facet of the cavity, and the blue line sinusoid incident on the right face is an odd number of quarter-wavelengths from the right facet. Note for simplicity of presentation, we only include in the figure light reflected from a single facet of the slot.

We consider to introduce a small refractive index step, i.e., perturbation/slot of short length d, on the right-hand side of the cavity in Fig. 3.2. This reduces the local refractive index by Δn over the length d. As the slots we introduce are perturbations, this allows us to make a useful approximation in our calculations. Our design approach includes all orders of reflection between the cavity facets and the slot faces but ignores all reflections between the slot faces. This approach simplifies the design process because it allows us to mathematically consider each slot in the grating independently. For illustrative purposes, we consider just the primary reflections between the slot faces and cavity facets.

Each introduced slot creates two independent subcavities, one with the respective cavity facet on each side of the slot, as in Fig. 3.2. To further simplify the analysis, we assume that the slot is one quarter-wavelength wide

$$d = \frac{\lambda_0}{4(n-\Delta n)}. \tag{3.5}$$

If we now consider the right propagating field, $\hat{E}_r$, incident on a perturbation centred at ϵL, then the amplitudes of the E-field plane waves reflected from the left face and from the right face of the perturbation, $\hat{E}_{rl-}$ and $\hat{E}_{rl+}$ are given by

$$\hat{E}_{rl\pm}(\epsilon L) = \frac{\Delta n}{2n}\hat{E}_0 \exp\left[\frac{\alpha_f}{2}\left(\frac{1}{2}+\epsilon\right)L \pm \frac{d}{2}\right]. \tag{3.6}$$

Setting $d = 0$ when calculating the amplitude of the reflected wave and treating these as two independent reflections at ϵL. When the left face of the perturbation is an integer number of half-wavelengths from the left cavity facet, each of these reflections adds independently to the left propagating field, increasing its amplitude by $\hat{E}_{rl}(\epsilon L) = \frac{\Delta n}{2n}\hat{E}_r(\epsilon L)$. The field intensity is proportional to the total E-field squared. To first-order in Δn, each reflection increases the magnitude of the field squared by

$$\left(\hat{E}_l + \hat{E}_{rl}\right)^2 - \hat{E}_l^2 = \frac{\Delta n}{n}\hat{E}_r(\epsilon L)\hat{E}_l(\epsilon L). \tag{3.7}$$

This then leads to a fractional change in the power propagating to the left, ΔP_l, due to the two reflections, of

$$\Delta P_l = \frac{2\Delta n}{n} \frac{\hat{E}_r(\epsilon L)\hat{E}_l(\epsilon L)}{\hat{E}_l^2(\epsilon L)} = \frac{2\Delta n}{n} \exp\big(\alpha_f \epsilon L\big). \tag{3.8}$$

Similarly, the fractional change in power propagating to the right due to out-of-phase reflections from the perturbation is given by $\Delta P_r = -\frac{2\Delta n}{n} \exp\big(-\alpha_f \epsilon L\big)$, with the total fractional change in power ΔP then given by

$$\Delta P = \frac{4\Delta n}{n} \sinh\big(\alpha_f \epsilon L\big). \tag{3.9}$$

The increase in power in the laser cavity at the mirror loss threshold leads to a change in the modal mirror loss for the mode m_0, with unity net gain now occurring to first-order when

$$|r^2|^2 \exp\big(2(\alpha_f - \Delta\alpha_{m_0})L\big)(1+\Delta P) = 1, \tag{3.10}$$

where a positive value of $\Delta\alpha_{m_0}$ then describes the reduction in the mirror threshold for the m_0 mode. Solving this equation to first-order in Δn, we obtain for a quarter wavelength length perturbation centred at ϵL, that

$$\Delta\alpha_{m_0}(\epsilon) = \frac{2\Delta n}{Ln} \sinh(\alpha_f \epsilon L) \sin(2\Phi), \tag{3.11}$$

where $\sin(2\Phi) = 1$ when the left face of the perturbation is an integer number of half-wavelengths from the left cavity facet, and where Φ is the phase change between the left-hand facet and the centre of the perturbation

$$\Phi = \frac{2\pi}{n\lambda_0}\Big[\big(\frac{1}{2}+\epsilon\big)L - \frac{d}{2}\Big] + \frac{\pi}{4}, \tag{3.12}$$

with $\Phi = m_0\pi\big(\epsilon + \frac{1}{2}\big)$ when $\Delta n = 0$. The term $\sin(2\Phi)$ in Eq. 3.11 takes account of how $\Delta\alpha_{m_0}$ changes when the perturbation is not an integer number of half wavelengths from the left facet. The change in mirror loss has its maximum reduction for mode m_0 when the phase difference equals $p\pi + \frac{\pi}{4}$, where p is an integer, as in Fig. 3.2.

The gain change then varies as $\sin(2\Phi)$ as the perturbation position and Φ are changed. The sin term

$$\sin(2\Phi) = \sin(m\pi + 2m\pi\epsilon), \tag{3.13}$$

captures the reflection phase of both the left and right cavity facet with the slot, as shown in Fig. 3.3, and is applicable for any cavity mode, not just m_0.

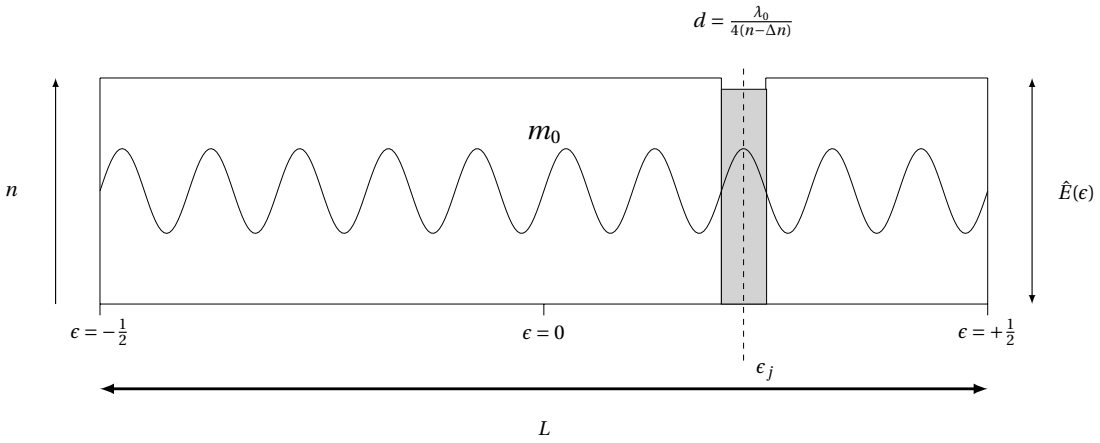


FIGURE 3.3: The $\sin(2\Phi)$=$\sin\left(2m_0\pi\left(\epsilon+\frac{1}{2}\right)\right)$ function aligning with the centre of the perturbation. The slot-width is one half-wavelength of the phase-doubled wave and a quarter-wavelength of m_0.

3.2.3 Slot pattern design using a feature density weighting function

To implement a slot grating using a weighting function, we followed the approach in Ref. [24], where the authors aimed to introduce a distribution of slots that would recreate the sinc function spectrally in k-space. The sinc function was seen as the ideal function, as it reduces the threshold of the selected mode, while leaving the surrounding modes unchanged, as in Fig. 3.4 b). An inverse-scattering approach was used, in which an inverse-Fourier transform was applied to the sinc function in k-space to calculate the required pattern in ϵ-space. Knowing that this process worked, we could then introduce functions in ϵ-space and analyse their behaviour in k-space. The continuous Fourier transform of the $f(\epsilon) = 1$ example

function is

$$f(k) = \int_{-1/2}^{1/2} f(\epsilon) \exp(-2\pi i \epsilon k) d\epsilon = \int_{-1/2}^{1/2} [\cos(2\pi\epsilon k) - i \sin(2\pi\epsilon k)] \, d\epsilon, \tag{3.14}$$

where we set $f(\epsilon) = 1$ on the right-hand side. As the function is even about $\epsilon = 0$, the integral of the sine component of the Fourier transform equals zero. Only the positive cosine needs to be considered, doubling to account for its negative mirror component about $\epsilon = 0$

$$f(k) = \int_{0}^{1/2} 2\cos(2\pi\epsilon k) d\epsilon = \mathrm{sinc}(\pi k). \tag{3.15}$$

The desired gain threshold spectrum in Ref. [24] is given by the function $f(\epsilon) = 1$ in cavity-space, when integrating ϵ from $\frac{-L}{2} \rightarrow \frac{L}{2}$. A diagram of the Fourier transform pair can be seen in Fig. 3.4.

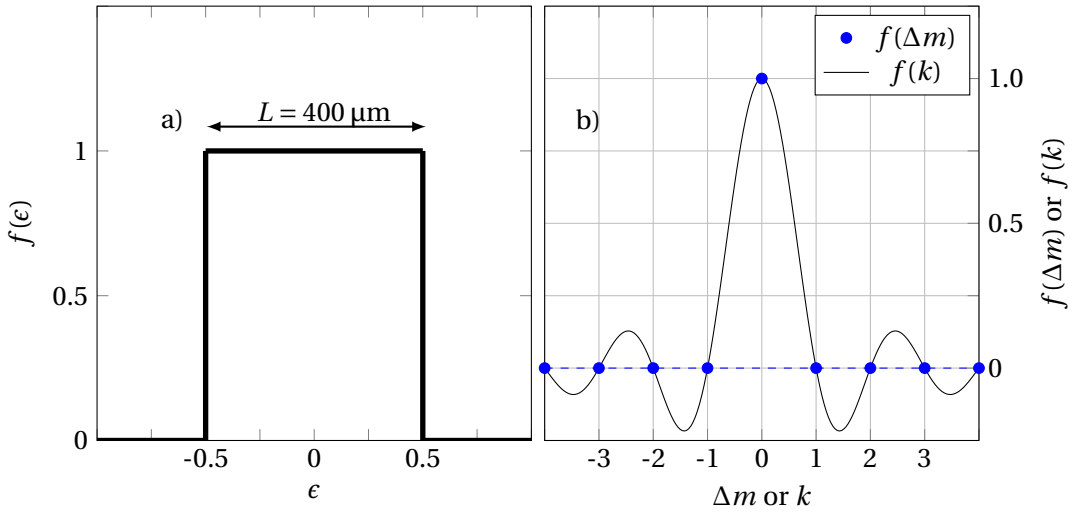


FIGURE 3.4: a) the top-hat real ϵ-space input function for full cavity length, b) its sinc function Fourier transform pair. Mode number is converted to wavenumber via $k = \frac{m\pi}{L}$.

We can see in Fig. 3.5 a diagram of multiple slots in a cavity. The dashed circles are points where the forward travelling E-field is reflected into the reverse travelling wave from the left side of each slot. Reflections (not shown in figure) also occur from the right facets of the slots. The net difference in the amplitudes of both waves scaled by the reflectivity of the slot is the net reflectivity experienced by the mode at that slot. This is an increasing value moving from $\epsilon = 0 \rightarrow +\frac{1}{2}$. Therefore, the position of the slot has a varying relationship with the selectivity of m_0.

The Fourier transform calculation is based on the integration of the inner product of the function under analysis with a series of plane waves within a defined numerical range. The modal plane waves in our laser cavity are exponentially increasing in amplitude with gain. We must therefore weight our functions to account for this amplitude change of the cavity modes to make our modal threshold calculation consistent with the Fourier transform.

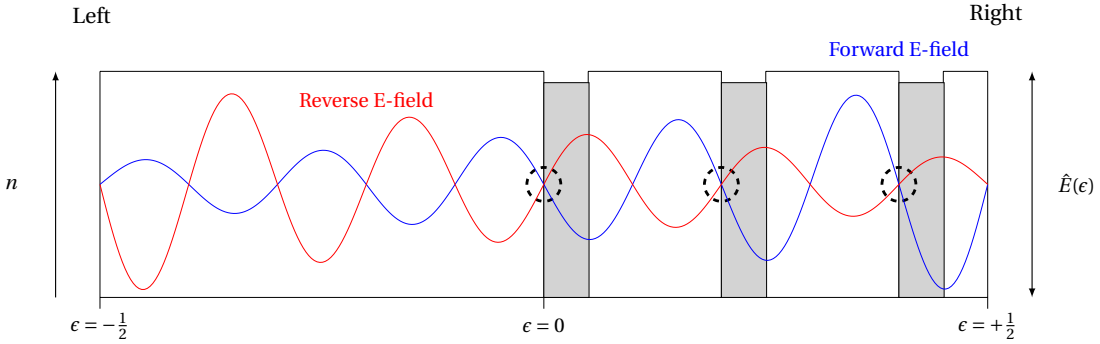


FIGURE 3.5: Forward and reverse travelling waves of the m_0 mode in the cavity. Dashed circles show the points at which the wave is reflected into its opposite direction wave, i.e., forward into reverse and vice versa. Reflections (not shown) also occur on the right-hand side of each slot.

This effect can be mathematically described by [85, 86, 26]

$$w(\epsilon) = \frac{1}{2}\left\{\sqrt{\frac{r_l}{r_r}}\exp(\alpha\epsilon L) - \sqrt{\frac{r_r}{r_l}}\exp(-\alpha\epsilon L)\right\}. \tag{3.16}$$

For the regime where both cavity facets have equal reflectivity, $r_l = r_r = r$, we approximate this as

$$w(\epsilon) \sim \sinh(\alpha_f \epsilon L), \tag{3.17}$$

to make the calculations simpler and more intuitive. We introduce the weighted slot distribution function as

$$h(\epsilon) = \frac{f(\epsilon)}{w(\epsilon)}, \tag{3.18}$$

where $h(\epsilon)$ is the design function after weighting. $h(\epsilon)$ is the function that must be matched by the density of slots in the cavity to recreate the mirror gain threshold spectrum of $f(\epsilon)$, Fig. 3.4 a) → Fig. 3.7 a).

To relate the mode selected by the grating, m_0, to its free-space wavelength, λ_0, we must allow for the cavity mode shift due to the reduced refractive index of the N perturbations in the cavity

$$m_0 = 2\left(\frac{Ln - Nd\Delta n}{\lambda_0}\right). \tag{3.19}$$

m_0 dictates the possible set values for the position of the slots, since the left face of each slot should be half-wavelength resonant with the m_0 mode and the left facet of the cavity. This discretises the slot placement, as ideally slots should only be placed at these set points.

To design the grating, we divide the length of the cavity by m_0, which gives a grid of points with a spacing equal to one half-wavelength of the forward travelling wave of m_0. We then weight the density of slots along this grid to match the weighted design function, $h(\epsilon)$. This will imprint the Fourier transform of that original design function, $f(\epsilon)$, on the mirror threshold spectrum of the device. The general method for sampling the weighted design function to retrieve the slot positions for one side of the cavity is [87]

$$\frac{1}{C}\sum_{N}\int_{\epsilon_{min}}^{\epsilon_j} h(x)dx = j - \frac{1}{2}, \tag{3.20}$$

where C is normalised to the number of slots introduced. ϵ_{min} is the start of the grating, as it is not always the case that the grating starts at $\epsilon = 0$; for example, the weighted inverse of the sinc function, $\frac{1}{\sinh(\epsilon)}$, diverges as $\epsilon \to 0$. Finally, we adjust the position of each slot to align the left face of the slot with the peak of $\cos\left(\left(\frac{1}{2}+\epsilon\right)\pi m_0\right)$, maximising the reflectivity of the slot and the selectivity of the pattern.

We can see in Fig. 3.6 a schematic example of an index-patterned device cavity. The grating consists of slots with centre positions at $\epsilon_{1,2,3}$. Reflections between the "Left facet" of the cavity, r_l, and the grating, $r[\hat{E}_0^+]$, generate most of the m_0 mode selectivity. Most of the mode amplitude is transmitted through the grating, $t[\hat{E}_0^+]$, and the "Right facet" of the laser, $\sqrt{1-r_r}$. We have also included a resonant and an anti-resonant sub-cavity for one slot in the diagram. Here, the resonant sub-cavity is formed with the "Left facet" and the anti-resonant sub-cavity is formed with the "Right facet". The index-patterned structure can be viewed as a series of connected Fabry-Pérot sub-cavities [17, 15].

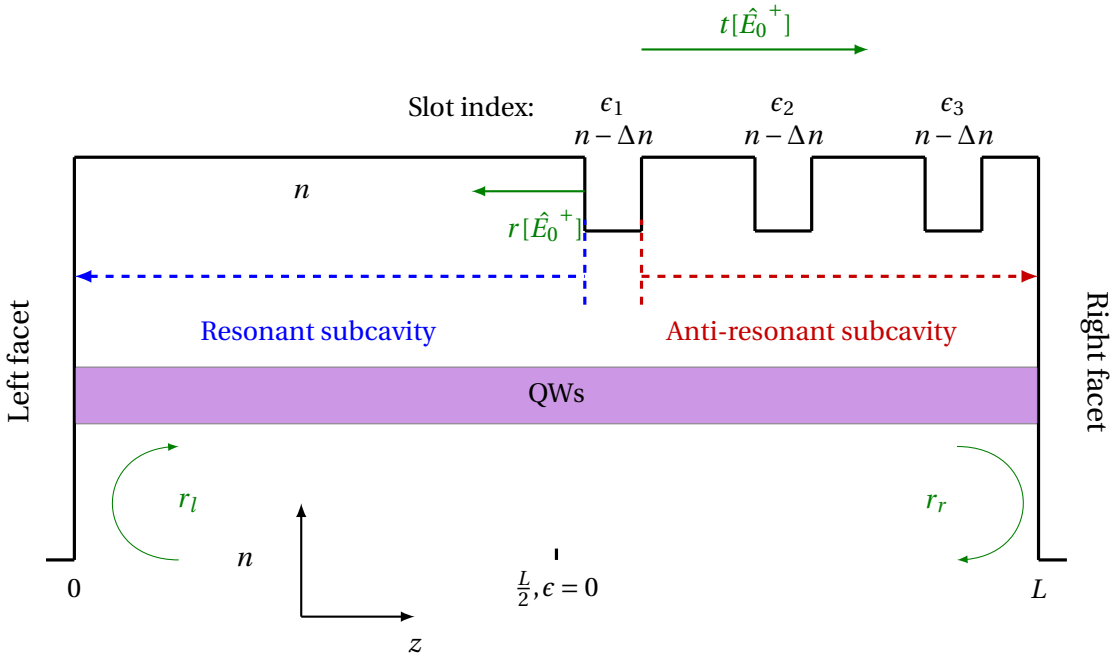


FIGURE 3.6: Schematic of an ideal index-patterned grating device. A series of sub-cavities are formed between the slots and the cavity facets.

Apart from a $\frac{\pi}{2}$ phase shift, a grating pattern is symmetric on either side of the centre of an uncoated cavity, in terms of its interactions with the cavity facets. This means that slots on one side of the cavity are sufficient to recreate the design function spectrally. The $\frac{\pi}{2}$ phase shift accounts for the reflection into either the forward- or reverse-travelling wave as one dominates on either side of the cavity. In our terminology, the pattern is implemented by placing slots on the right-hand side of the cavity, as in Fig. 3.6, predominantly affecting the forward travelling wave of the m_0 mode. Slots could be placed on the left side of the cavity; however, the index-pattered laser is often made with a HR coating on the "Left facet" and an anti-reflective (AR) coating on the "Right facet". The slots on the left side would then be resonant with the AR coating on the "Right facet", forming a significantly weaker sub-cavity than the slots on the right side that are resonant with the HR coating on the "Left facet". Slots on the left side of the cavity would minimally add to the mode selectivity and increase the optical loss in the cavity. In this thesis we only deal with HR coating of the left facet as AR coating the right facet was not part of the manufacturing procedure of the particular production runs we added our devices to. It still stands that slots on the left hand side of the cavity would form a weaker resonance and contribute less to mode selectivity.

As each slot face acts as a point of frequency discrimination, essentially as a sampling point for the function, there must be a sufficient number of slots to sample the functions correctly, but not too many to incur excessive optical loss. Increasing the number of slots gives an improved discrete approximation to the continuous target function and thus increases the modal selectivity of m_0. However, the greater the loss or variation in lasing wavelength from grating introduction, the less effective the design method will be. To this end, you do not want functions with abrupt changes in feature density, as these take more points to sample correctly [87, 88]. In our initial modelling of a laser we work with $n = 3.2$, which is typical for a 1550 nm laser. We also use twenty slots, $N = 20$, with a refractive index step of $\Delta n = 0.02$, as our industrial partner, Eblana Photonics Ltd. [61], uses parameters similar to these for their grating designs to produce devices with good modal selection (SMSR> 40 dB) and slope efficiency (> 0.1 W/A). These are also similar to values used in the literature [36, 89].

3.2.4 Fourier calculation of the modal mirror loss

After generating a slot pattern from a weighted design function, we use a discrete Fourier transform approach to calculate how the grating modulates the resonant mode mirror loss of the Fabry-Pérot cavity. We start by expanding Eq. 3.13 using trigonometric identities

$$\sin(m\pi + 2m\pi\epsilon) = \cos(m\pi)\sin(2m\pi\epsilon) + \sin(m\pi)\cos(2m\pi\epsilon). \tag{3.21}$$

The calculation can then be shifted to integer modes, Δm, centred around m_0; $m = m_0 + \Delta m$, using for integer m that $\cos(m\pi) = \cos(m_0\pi)\cos(\Delta m\pi)$ and $\sin(m\pi) = 0$ [86]

$$\cos(m\pi)\sin(2m\pi\epsilon) = \cos(m\pi)\cos(\Delta m\pi) \times [\sin(2\pi\epsilon m)\cos(2\pi\epsilon\Delta m) + \cos(2\pi\epsilon m)\sin(2\pi\epsilon\Delta m)]. \tag{3.22}$$

We can substitute Eq. 3.22 into Eq. 3.11 and then sum for each of the N perturbations introduced [86]

$$\Delta\alpha_{\Delta m} = \frac{2\Delta n}{Ln}\cos(m_0\pi)\cos(\Delta m\pi)\times \sum_{j=1}^{N} w(\epsilon)[\sin(2\pi\epsilon_j m_0)\cos(2\pi\epsilon_j\Delta m) + \cos(2\pi\epsilon_j m_0)\sin(2\pi\epsilon_j\Delta m)]. \quad (3.23)$$

This equation transforms the cavity slot positions into modal mirror loss modulation, calculating the mirror threshold for each mode in the required spectral range. Eq. 3.23 allows us to analyse how changes in the positions of slots in an index-patterned grating change the threshold gain of the modes in the device spectrum. The mirror threshold modulation function can then be added to the mirror threshold of the cavity

$$\alpha_m = \alpha + \Delta\alpha_m, \quad (3.24)$$

where α_m is the mirror loss experienced by the m^{th} mode after the grating introduces a mirror threshold modulation of $\Delta\alpha_m$. Fig. 3.7 shows a diagram of the design and modal mirror threshold calculation process. Panel a) is the design function after weighting, panel b) is the slot pattern generated by the function $h(\epsilon)$, and panel c) is the calculated Fourier-transformed mirror loss spectrum.

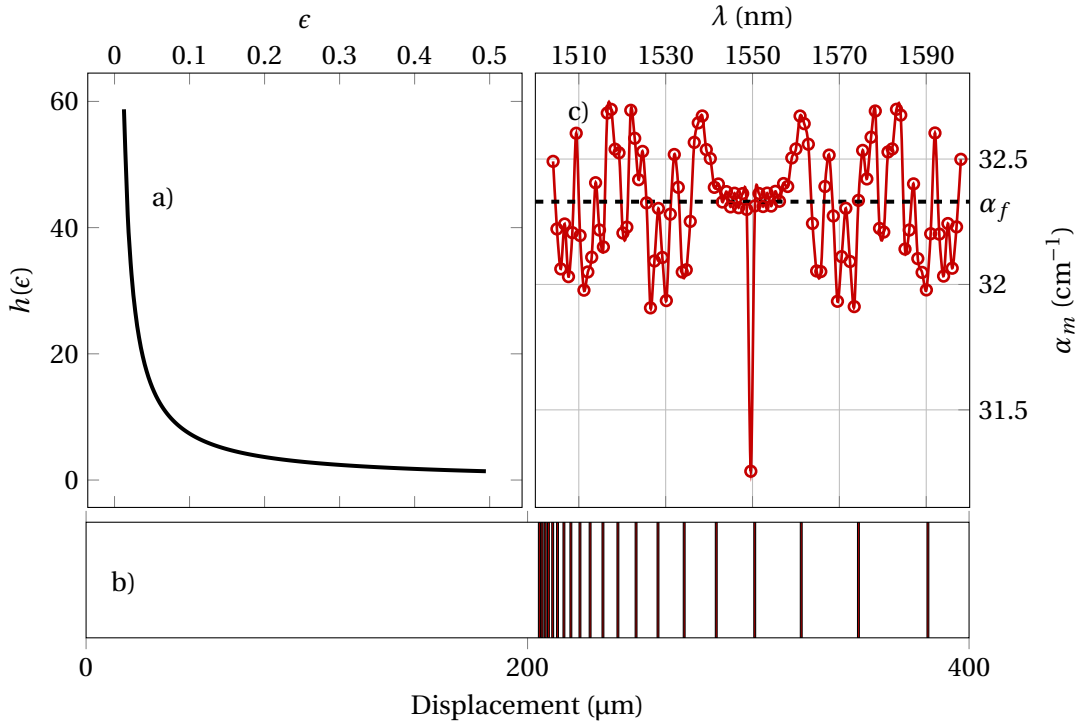


FIGURE 3.7: a) $h(\epsilon)$ for $f(\epsilon)$=1 and ϵ=0.0125→0.5, b) the slot pattern with slot density weighted to match $h(\epsilon)$, for N=20, n=3.2, Δn=0.02, and L = 400 μm. c) Discrete Fourier transform of the cavity in b).

It has generally been assumed in the design of index-patterned lasers that all of the perturbations introduced are perfectly positioned with respect to the cavity facets to select m_0 [24, 36]; and therefore the sine wave reflection from the left slot facet is perfectly aligned to the left travelling m_0 E-field sine wave, $\sin(2\pi\epsilon_j m_0) = 1$; and is perfectly out of phase with the cosine reflection wave right-hand facet of the slot, $\cos(2\pi\epsilon_j m_0) = 0$. We note that ϵ_j is at the centre of the slot, midway between the two slot faces. Only the first term in the square brackets on the right-hand side of Eq. 3.23 needs to be considered. In this case, the constructed index pattern represents a discrete approximation to a continuous Fourier cosine transform of the real-space design function, $\cos(2\pi\epsilon_j \Delta m)$, corrected to allow for the variation in the amplitude of the weighting function, $w(\epsilon_j) = \sinh(\alpha_f \epsilon_j L)$, along the cavity. In addition to considering perturbations that are ideally positioned, our analysis will also include the second term on the right-hand side of Eq. 3.23, $\cos(2\pi\epsilon_j m_0)\sin(2\pi\epsilon_j \Delta m)$, to consider the case where the slots are not ideally positioned with respect to the left facet.

3.2.5 Spectral effects of slot-width

A sketch of an ideal slot in a cavity model can be seen in Fig. 3.8. An ideal slot-width in our modelling is $\frac{\lambda_0}{4(n-\Delta n)}$ or 0.122 µm for $n-\Delta n = 3.18$, and $\lambda_0 = 1550$ nm, which are our modelled cavity parameters. This slot-width is ideal as it minimises additional spectral effects of the slot on the gain threshold spectrum. It was slot position rather than slot-width that was the focus of our research. This slot-width is difficult to create because it is beyond the resolution of photolithography (~ 0.5 µm). It is also beyond the resolution of E-beam etching [90], since deviations > 5 nm in slot-width will have a noticeable effect on the Fourier threshold spectrum. It is also difficult to etch a small deep slot reproducibly for manufacture [87]. Ideal slot-widths become even more difficult for short-wavelength devices < 1550 nm. Therefore, it is important to understand the implications of not having an ideal slot-width for the grating.

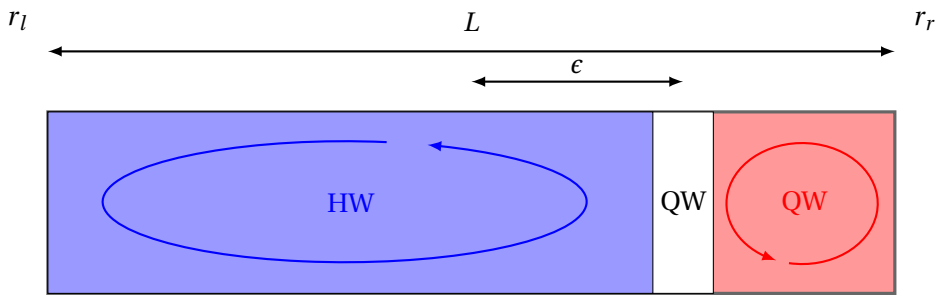


FIGURE 3.8: Ideal slot-width and cavity model. Longer half-wavelength (HW) resonant selective section on the left and a shorter quarter-wavelength (QW) resonant anti-selective section on the right.

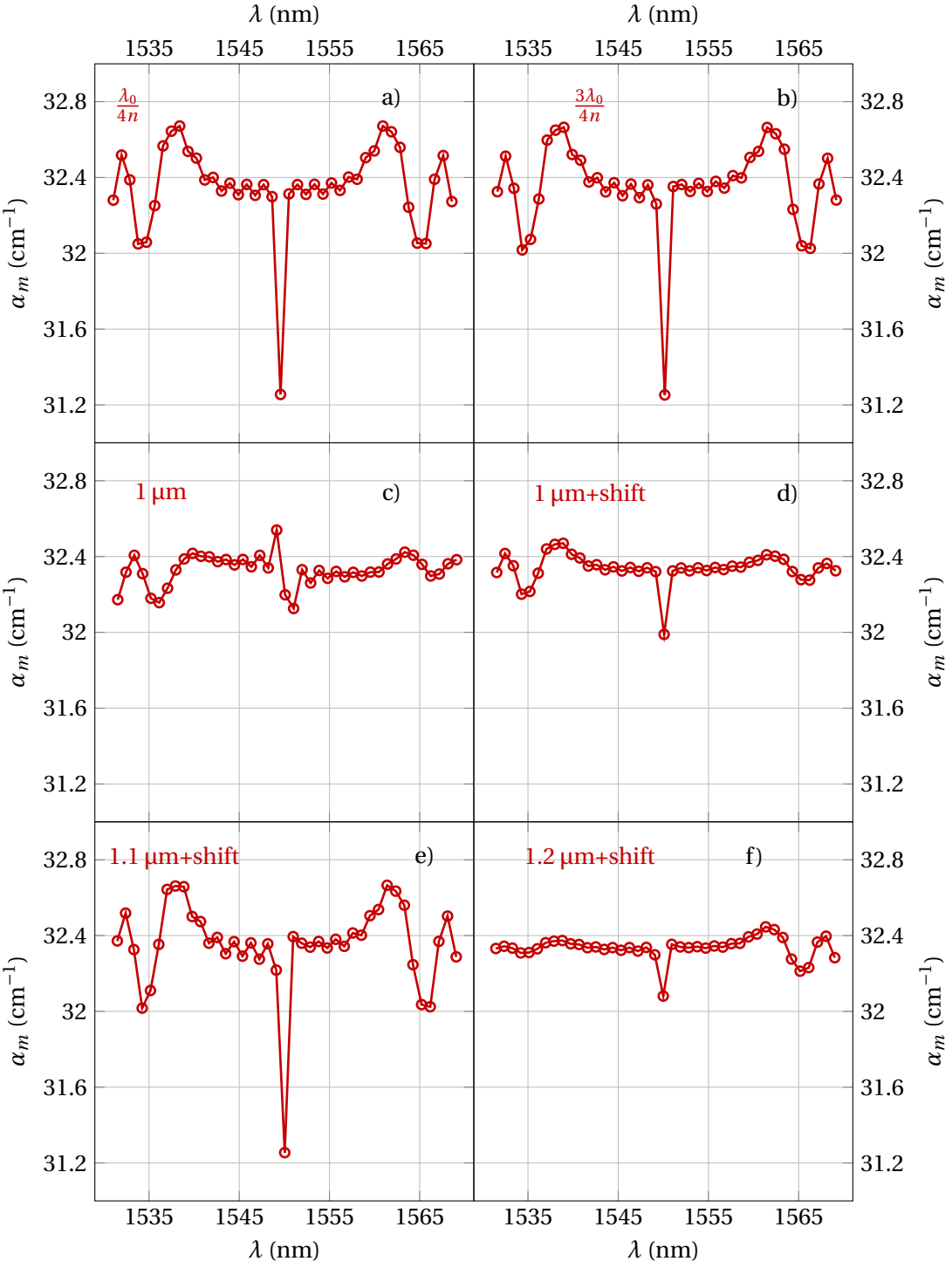


FIGURE 3.9: Effect of changing slot-width on the threshold gain spectrum of an index-patterned device. For $f(\epsilon)$=1, N=20, n=3.2, Δn=0.02, and $L = 400$ µm.

In Fig. 3.9 a), we can see a threshold spectrum from an index-patterned grating when each slot matches the ideal grating for the $f(\epsilon) = 1$ function using the modelling parameters defined in Tab. 4.2. In Fig. 3.9 b), we can see what happens when the slot is a third-order of Bragg reflection, $\frac{3\lambda_0}{4n}$. The slot is still quarter-wavelength resonant, so the threshold gain spectrum is largely unchanged. In Fig. 3.9 c) and Fig. 3.9 d), we have a non-quarter-wavelength resonant dimension for the slot-width of 1 µm. In Fig. 3.9 c), the gain selection pattern is distorted. In Fig. 3.9 d), the position of the grating in the cavity is shifted to cancel the sine Fourier transform components in the spectrum, giving an approximately cosine gain threshold spectrum. We can see that the selectivity is markedly reduced from Fig. 3.9 a), as the slot is not close to being a quarter-wavelength resonant, $\frac{1\ \mu m}{1.55\ \mu m/4n} = 8.26$. In Fig. 3.9 e), we can see that if the slot-width is increased marginally by 0.1 µm, then much of the selectivity is recovered, as the slot is now closer to being quarter-wavelength resonant, $\frac{1.1\ \mu m}{1.55\ \mu m/4n} = 9.08$. In Fig. 3.9 f), we can again see a reduction in selectivity for the 1.2 µm slot as we move away from a constructive resonance in the cavity.

When using plane waves to model an ideal 1D cavity we overestimate slot resonances. The 1D plane wave model has all interactions occurring on one axis. In 2D modelling, more variation of the mode amplitude with cavity position is allowed, resulting in less spectrally narrow resonances in the cavity [84, 15]. Slots are regions of relatively high loss; this will degrade reflections in the section, reducing resonances further. However, resonances are still present; i.e., it is important to target a slot-width that is close to being an odd quarter-wavelength multiple [91]. For example, it is more beneficial to target a slot-width of 1.1 µm than 1 µm. Although 0.1 µm is within the resolution tolerance of photolithography, slot-widths should converge to target a length of 1.1 µm.

3.3 The scattering matrix method (SMM)

To verify and benchmark our first-order Fourier plane wave model, we also used a scattering matrix method (SMM) to calculate the mirror gain threshold modal spectrum of our device. The SMM that we use combines the individual scattering matrix for each uniform section of the waveguide one by one to calculate the scattering matrix for the entire cavity structure. We applied a scattering matrix of zero length and a refractive index of one at each end of the laser cavity; this simulates the laser facet coupling into free-space. From this we have a scattering matrix for a complete device, allowing us to calculate the output E-field amplitudes ($\hat{E}_2^+$) from the input gain and a small-value E-field ($\hat{E}_1^+$) to simulate spontaneous emission in the cavity, Fig. 2.6. Although theoretically our SMM output E-field amplitude squared is optical intensity, we use relative arbitrary values (AU) for input and output E-field. Given the approximations we use in the model, real values of intensity would have little merit. One scattering matrix for the cavity is generated per wavelength per applied gain value, which means that every wavelength within the desired range must be scanned discretely.

To calculate the threshold mirror gain function using the SMM, we must first find the modes and then find the gain value at which the modes reach their threshold. It is difficult for the SMM to find the threshold values, as the laser modes are sensitive to the applied modal gain values, given their exponential relationship

$$\Gamma g = \ln\left(\frac{\mathrm{Re}\left\{\hat{E}_1{}^+\right\}}{\mathrm{Re}\left\{\hat{E}_2{}^+\right\}}\right). \tag{3.25}$$

Mode peaks are also of narrow spectral width. We can see in Fig. 3.10 a phase diagram of the Fabry-Pérot cavity mode formation process. The E-field wave is restricted when introduced into a Fabry-Pérot cavity; allowing some frequencies but suppressing others, Fig. 2.5 a) and b). When gain is applied, the maximum amplitude of the E-field increases, but the range of allowed frequencies is further restricted, as in Fig. 3.10 c) and d).

Mathematically, this can continue until infinity; forming a pole, representing a mode. In a real device, the minimum mode frequency width is limited by the maximum current and therefore gain, but also noise in the cavity. As our theoretical SMM cavity is noiseless and the gain is arbitrary, we can have infinitely narrow modes. However, there is only a finite resolution at which we can perform the SMM scan. Selecting a wavelength close to the ideal-mode plane wave wavelength gives a plane wave with properties close to that of the ideal mode, i.e., the correct expected gain threshold.

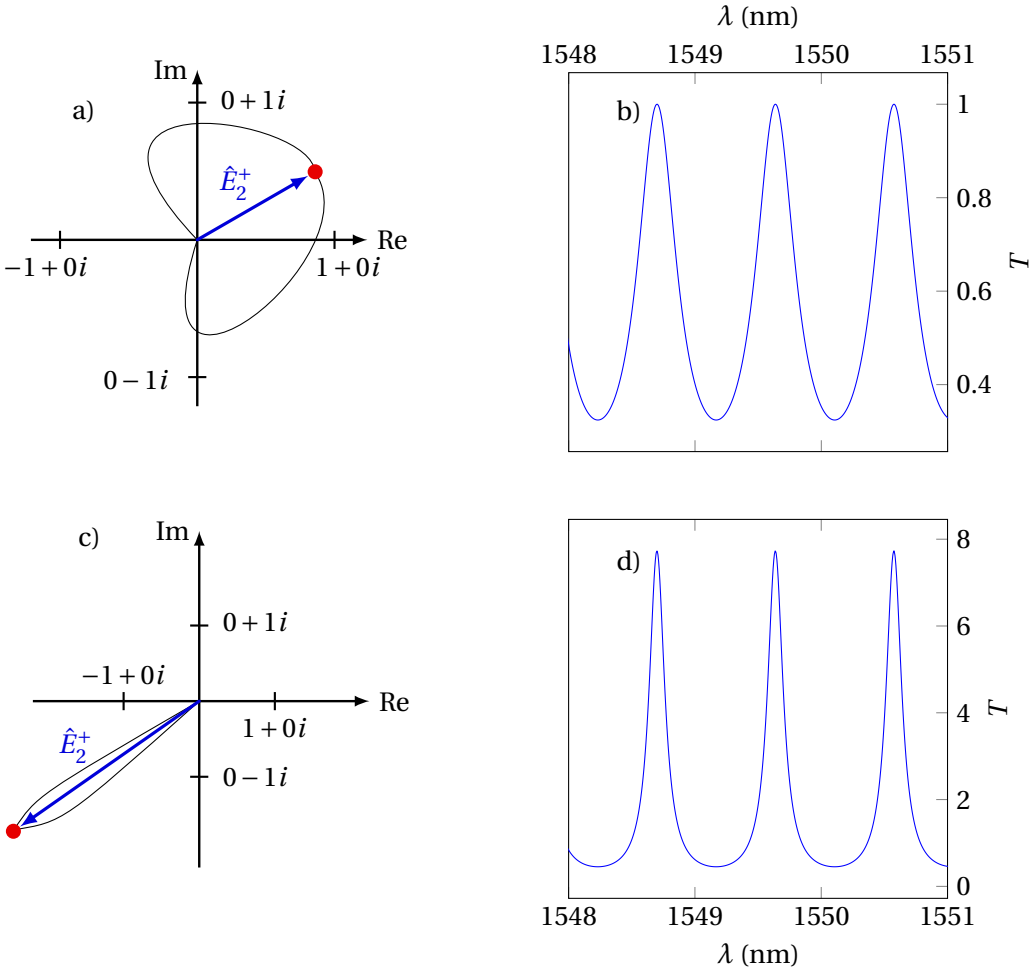


FIGURE 3.10: a) phase and amplitude trace of an output E-field ($\hat{E}_2^+$) from a Fabry-Pérot cavity, b) SMM calculation of the power transmission $\left(T = t^2 = \left(\frac{\hat{E}_2{}^+}{\hat{E}_1{}^+}\right)^2\right)$ of the E-field vector through the cavity. c) gain applied to the E-field in the cavity, d) SMM showing the formation of poles in the spectrum as a result of gain and feedback [92].

In Fig. 3.11 we can see an SMM calculation of the threshold function for an index-patterned laser structure with the sinc function modal pattern using the parameters in Tab. 4.2. To find the mode thresholds, we developed an algorithm that first made a high-resolution SMM sweep across the full spectrum of wavelengths we wished to analyse, e.g., 1530 → 1570 nm. We made the sweep at an applied gain greater in magnitude than the mirror loss of the cavity; e.g., −39 cm^{-1} for Fig. 3.11, which has a cavity threshold 32.3 cm^{-1}. We then selected the peaks of this sweep and reduced the gain applied to them until they reached an output value close to threshold, e.g., 1 AU. We then re-scanned a region around the peak (e.g. ±0.1 nm) to ensure that we were operating at a local maximum. We then increased the gain in the cavity until this wavelength reached an arbitrarily high output value, e.g., 10,000 AU. The gain at this high output power is the calculated mirror threshold gain of the mode. This process was repeated for each peak, allowing for the calculation of the modal mirror threshold spectral function.

Increasing the resolution increases the sweep time. Ideally, you want to find the sweep resolution with the minimum number of points that can find all of the mode centres. Making an initial scan beyond the threshold gain of the resonator more efficiently finds peaks close to the mode centre singular value than making scans below the cavity threshold value. The sweep resolution was typically in the range $1 \times 10^{-3} \rightarrow 1 \times 10^{-5}$ nm.

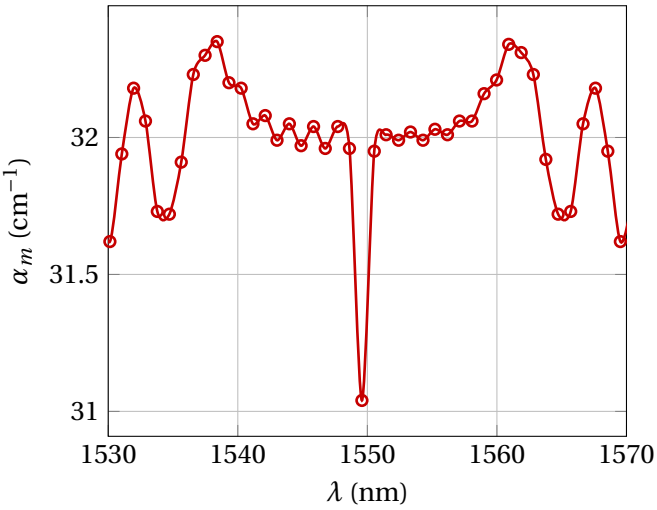


FIGURE 3.11: Example of the modal mirror loss threshold spectrum output from the SMM calculation for $f(\epsilon)$=1, N=20, n=3.2, Δn=0.02, and $L = 400$ µm.

Apart from reflections beyond first-order, the SMM has inherent differences to the Fourier method. The Fourier method analytically calculates the modes as phase-shifted modes of the Fabry-Pérot cavity after the introduction of the grating. The SMM must find these values in the cavity model rather than prescribing them. The SMM by design does not go to the mirror threshold gain value and only goes to a value close to the threshold. The SMM also operates at a value close to the mode wavelength, and the Fourier calculation operates at a prescribed mode wavelength.

3.4 Bragg grating-based devices

There are two incumbent single-mode edge-emitting laser designs, both based on Bragg mirrors; the distributed feedback (DFB) and the distributed Bragg reflector (DBR) device. We will first analyse how a Bragg mirror reflects light. We will then see how it is applied for single-mode lasing in a DFB and a DBR laser.

3.4.1 The Bragg mirror

Bragg mirrors are used in lasers because they can increase the reflectivity amplitude beyond what a single surface can provide, or they can be made to select a single frequency, or often fulfil both functions simultaneously. Bragg mirrors are based on consecutive repeating layers of lower (n_L) and higher (n_H) refractive index material or structures with an equivalent effective refractive index — these are known as Bragg pairs. Each Bragg pair combines for in-phase reflections at a specific wavelength known as the Bragg wavelength, λ_B, if the thickness of each layer is $\frac{\lambda_B}{4n_{L/H}}$ resonant.

Looking at the grating as a whole, forward and reverse travelling E-field waves exchange energy efficiently if they are of the same wavelength, forming a standing wave in the structure [93]. Reflectivity can be treated as distributed throughout the structure, or it can be considered to occur cumulatively as an effective single reflection, r_{eff}. Effective reflectivity is assumed to occur at one discrete point, usually at the start of the grating. The key parameter of the Bragg mirror is κ, which is the coupling value between the forward and reverse travelling waves. For the 1D interpretation that we use in our research, κ is the mean reflectivity per unit length [38]. κL is then the reflectivity of the entire grating. Fig. 3.12 shows a Bragg mirror reflecting an inbound E-field, oscillating at the Bragg wavelength, $r_{eff}\hat{E}^{+}_{\lambda_B}$.

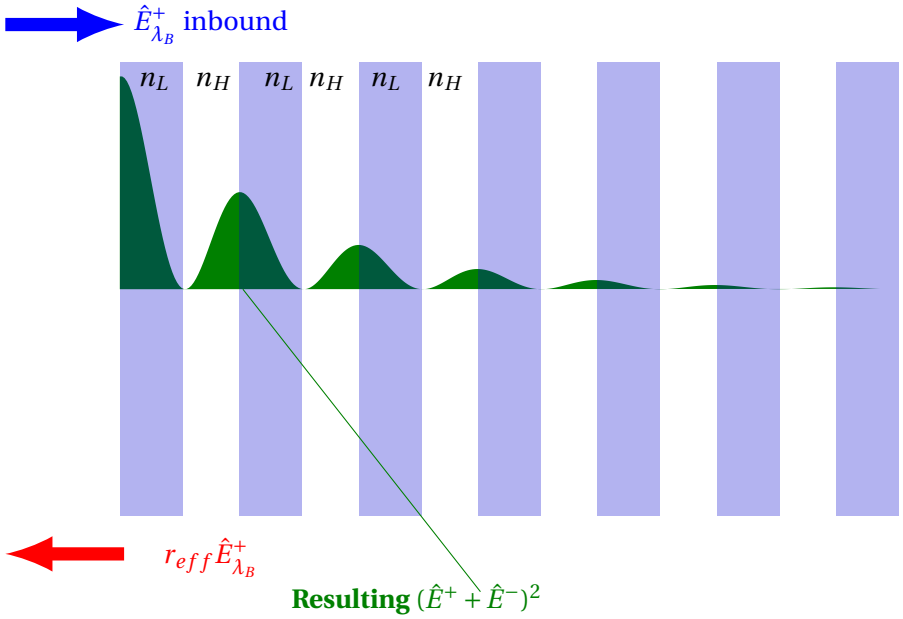


FIGURE 3.12: The E-field generated by an ideal $\frac{\lambda_B}{4n}$ Bragg mirror, coupling energy from the forward travelling wave to reverse, without gain or loss.

Using an SMM to analyse a Bragg mirror, we can see in Fig. 3.13 a) how increasing Δn increases the reflectance to the limit of one, centred at the Bragg wavelength, and broadens the reflectance band. In Fig. 3.13 b) the number of repeat Bragg pairs increases with the refractive index step being held constant. The reflectance also converges to one but does not broaden, and only resolves more closely to the "Top-hat" function centred on the Bragg wavelength. The first-order Fourier calculation cannot be used to analyse Bragg structures. Inter-slot reflections are the basis of mode selection in these devices and are not included in the first-order calculation.

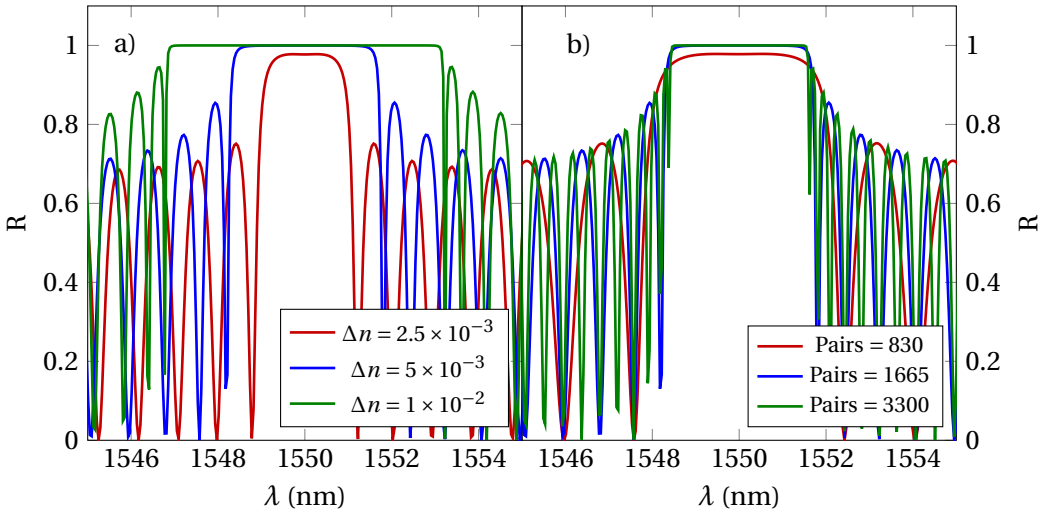


FIGURE 3.13: SMM modelling of a $\frac{\lambda_0}{4n}$ Bragg mirror. a) number of Bragg pairs is held constant at 1665, and the refractive index step is changed; b) refractive index step is kept at Δn=5 × 10^{-3} and the number of pairs is changed.

3.4.2 The distributed feedback (DFB) laser

A DFB laser uses an intra-cavity grating, typically etched into the cladding of the waveguide either above or below the gain section. The DFB grating reflections are treated as distributed along the cavity. The cavity length is related to the mode penetration into the device grating and is not a set value; leading to the concept of an effective cavity length. The effective cavity length can be determined by the mode spacing of the laser, or estimated in the design stage based on the magnitude of Δn and optical loss in the grating [94, 64].

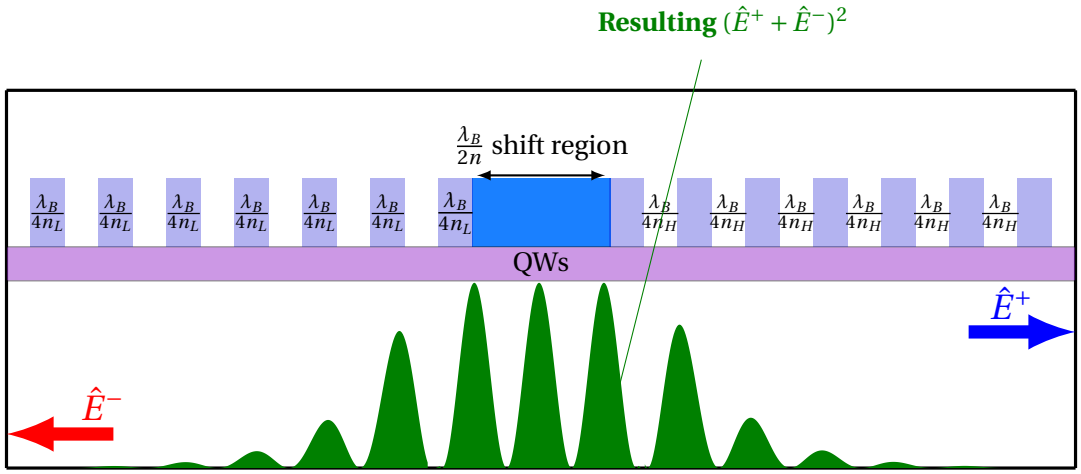


FIGURE 3.14: DFB diagram, with the resulting E-field standing wave of the cavity [95, 96].

One issue with the Bragg mirror in a DFB laser is that there is a degeneracy of modes on either side of the Bragg wavelength. This often results in a low SMSR device, as two modes are equally selected. For single-mode lasing, DFB lasers are typically designed with an extra $\frac{\lambda_0}{4n_H}$ phase shift in the n_H layer at the centre of the cavity, as in Fig. 3.14 and loss modulation between layers in the Bragg pair [64, 97]. This allows one single mode to form at the Bragg wavelength which can be tailored to have high SMSR [93, 98]. This also allows mode formation without facet reflections, unlike the index-patterned laser. In Fig. 3.15 a), we have the power reflectance, R, spectrum calculated using the SMM algorithm of a lossless DFB laser of $\Delta n = 5 \times 10^{-3}$, 1665 Bragg pairs with layer thicknesses of $\frac{\lambda_0}{4n_{L/H}}$. This gives a total cavity length $L \sim 400\,\mu\text{m}$. In Fig. 3.15 b), we calculated the modal mirror threshold spectrum for the device. In Fig. 3.15 c) and d) we can see how the addition of a phase step $\frac{\lambda_0}{4n_H}$ to the central slot with a 1 cm^{-1} loss modulation along the grating selects a single mode. The loss modulation was generated by adding a constant loss of 1 cm^{-1} to the cavity, then adding an additional 1 cm^{-1} loss to the higher refractive index layers.

The modal modulation is stronger in Fig. 3.15 than in Fig. 3.11. The parameter values of this Bragg grating were selected for a clear demonstration of a Bragg mirror, and are not from an actual device. The grating values in Fig. 3.11 are more similar to a real index-patterned laser, making it an unfair comparison of mode selection between the device types.

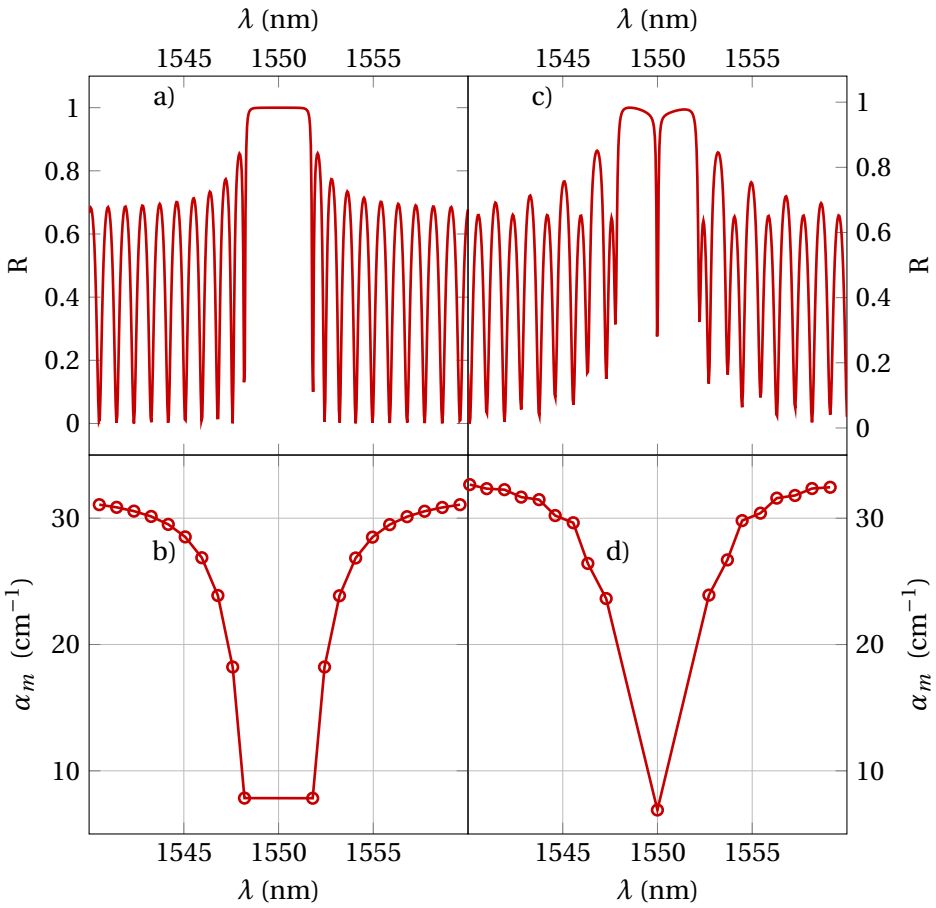


FIGURE 3.15: SMM modelling of a DFB laser; a) a reflectance spectrum of a quarter-wavelength stack of layer with Δn=5 × 10^{-3}, c) has an extra quarter-wavelength shift applied and 1 cm^{-1} loss modulation applied to the Bragg pair. b) and d) are the respective mirror threshold scans for the laser devices.

The DFB is used more often for sources where tuning of the lasing wavelength is not required. The grating is along the length of the cavity and is therefore difficult to tune without affecting the device's other operating factors, e.g., current density and cavity temperature. Typically, DFB lasers only tune ~ 5 nm. This soft limit is due to the fact that DFBs mainly use temperature to change the refractive index of the grating for frequency tuning. This typically occurs at a rate of ~ 0.1 nm °C^{-1}, meaning that the temperature of the cavity must be shifted by 50°C to tune the wavelength 5 nm. The gain-bandwidth peak of the device also changes with temperature, at a higher rate of ~ 0.5 nm °C^{-1}, resulting in a peak shift of 25 nm [99]. This is likely to put the lasing wavelength in a lower spectral gain region with a competing mode near the peak of the gain-bandwidth, reducing the SMSR [99, 100]. Wider tuning is possible with more exotic structures [101].

3.4.3 The distributed Bragg reflector (DBR) laser

In contrast to the DFB laser, the DBR laser has a Bragg mirror external to the gain section; at the front and back, but only a mirror at one end is necessary, Fig. 3.12 and Fig. 3.16. The Bragg mirrors of a DBR laser are designed to be discrete reflectors at the end of the cavity; however, there is significant mode-leakage into the grating sections [93]. A DBR is used when large tuning ranges are required. The fact that the gratings are separate from the gain section means that they can be tuned without changing the gain-bandwidth of the gain section [102]. The gratings act as facets for the device, controlling the level of reflectivity back into the gain section of the cavity and the amount of power output. The Bragg mirrors also dictate the spectrum of the device [93]. The front and back mirrors can have different overlapping phase-shifted grating patterns to select several modes for wide-bandwidth tuning (> 50 nm) [103, 102]. A DBR would typically have half or less mirror pairs than a DFB laser (< 700) [104, 105], but these can have a bigger refractive index step to maintain mode selectivity [38, 106, 107].

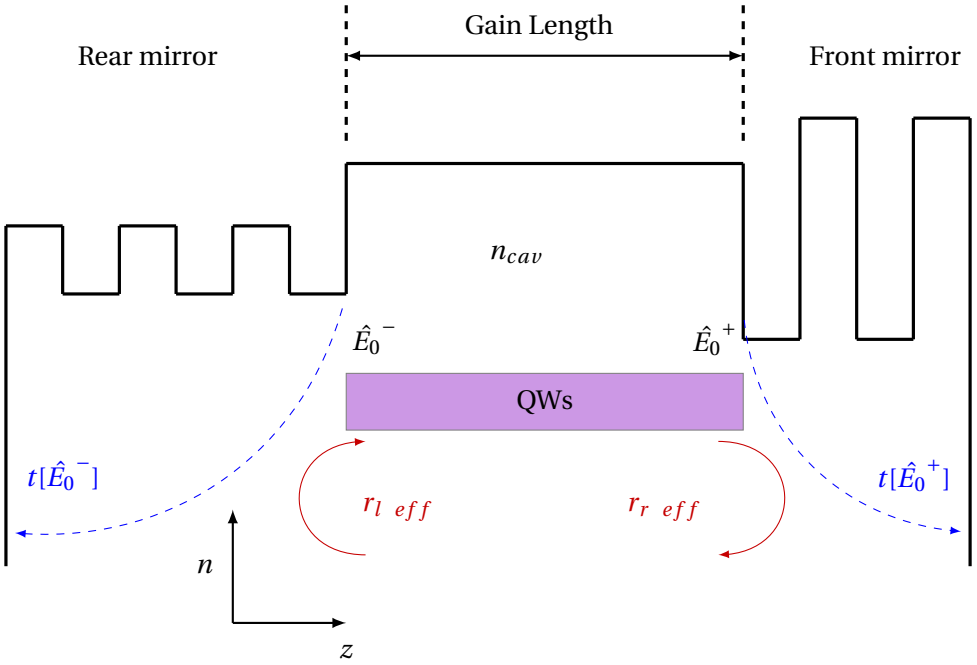


FIGURE 3.16: DBR laser schematic, refractive-index steps forming gratings for front and back mirrors [95].

3.5 Discussion

The key point of this chapter is to develop both a physical and a 1D Fourier model for the index-patterned laser. Both the analytical Fourier-based method and the semi-analytical SMM fundamentally look to quantify the changes to the E-field plane wave modes in a laser cavity via changes to the modal mirror gain threshold spectrum. The SMM includes all reflections in the cavity, and the Fourier method only accounts for reflections between the slots and the facets, not reflections between the slots.

We also analysed the importance of the slot-width on the index-patterned device spectrum, noting that real devices behave differently from the 1D model. There is a 2D aspect to the mode path in the cavity, where the mode extends upward to the slot and reflects that we are not capturing [15], see Fig. 3.1. We also did not capture the significant 2D modal shape mismatch of reflection between the slot and the waveguide [84]. Higher-dimensional E-field calculations of the complete device cavity are required to understand these effects on modal selection. In terms of maximising performance, our Fourier function approach could be taken as a starting point in an optimisation algorithm; then, an iterative 2D SMM could be used to maximise performance taking into account higher-dimensional cavity effects and higher-order reflections [42].

There are several methods to introduce refractive index steps into a Fabry-Pérot cavity, but none is as widely used as the waveguide slot. The etching of a hole through the cavity of the device is one [32]. It is a simpler method to create a refractive index step, as the etch depth of the hole does not have to be precisely controlled. However, holes have significantly more optical loss than slots. Grating designs need to be relatively simple in this case, as there are fewer holes and therefore reflection points available to approximate the pattern. Extended ridge devices have been modelled and developed for index-patterned devices [22, 23]. Here, a portion of the ridge is flared to change its effective refractive index. Another perturbation grating method, relevant to the rapid growth in silicon photonics in recent years, is placing a III-V gain section on a pre-etched silicon waveguide [36, 37]. This method could provide a major future application area for the index-patterned laser, as it allows a simple, yet high-performance laser to integrate relatively seamlessly onto silicon PICs. Further research is needed to examine the effect of changing the type and shape of the refractive index step.

Analysing the DFB and DBR lasers allows us to understand the competing edge-emitting laser types and how the index-patterned device operates differently. DFBs can provide sufficient SMSR for single-mode lasers ($>$ 40 dB) and DBRs can deliver low-linewidth ($<$ 100 kHz) with sufficient SMSR across a wide bandwidth ($>$ 50 nm) [108, 102]. The intrinsic linewidth of a DFB laser is relatively high ($\sim$ MHz), and can only meet low-linewidth requirements with additional suppression measures. The index-patterned laser has can meet these requirements, with a naturally lower intrinsic linewidth [11, 13]. Although DFB and DBR lasers are made with prescribed cavities, reflections from the facets of the waveguide outside the Bragg structure are still an issue. One of the main reasons why DFB and DBR lasers are so widely used today is that they are established devices with highly refined manufacturing processes. In this chapter, we have seen how the index-patterned device is a simpler structure, more suited to mass manufacture, with potentially higher performance in terms of linewidth.

In the next chapter, we will theoretically analyse the effect of changing the grating design on the spectrum of index-patterned lasers.

Chapter 4

Fourier cavity modelling

4.1 Introduction

This chapter will focus on our Fourier modelling of index-patterned lasers. In Sec. 4.1.1 we derive a mathematical proof of how increasing the weighted-average of slot position can improve the selectivity of m_0. Sec. 4.1.2 explains how grating-facet phase changes can be incorporated into the Fourier method. In Sec. 4.2 we will analyse the three exemplar design functions that we use for modal selection in this chapter, as we will use different functions in Ch. 5 and Ch. 6. Sec. 4.2.4 compares the first-order Fourier method with the SMM, which includes all orders of reflection. In Sec. 4.2.5, the change of the grating-facet phase is modelled. Sec. 4.3.1 will compare the calculated selectivity of m_0 with the weighted-average of the slot position. Sec. 4.3.2 will look at the Fourier properties of the index-patterned gratings. Sec. 4.3.3 will assess the phase and yield implications of using different design functions in the cavity. Finally, Sec. 4.3.4 will analyse specifically how our exemplar functions behave with changing temperature.

We compared three different exemplar design functions and, therefore, three different slot distributions by calculating their modal mirror loss spectra. We could then draw conclusions about the effect of different properties of design functions on the spectrum of the device. From the sinh term in Eq. 3.23, we can see the dependence of the magnitude of the modal modulation on the position of the slot in the cavity. We explore the possibility of using this property to increase the m_0 selectivity of an index-patterned grating. The selectivity of m_0 over additional modes in the spectrum is also an important factor for the SMSR of the device. We will also explore how the choice of design function can improve this.

Facet cleaving has a large error margin, $\sim 10\,\mu m$. The etching of the device facets has much greater control of the facet position, but is still beyond the wavelength fraction (< 5 nm) required to align to $\cos\left(\left(\frac{1}{2}+\epsilon\right)\pi m_0\right)$ with the slots [90]. A variation in the optical path length from the grating to the facet with manufacture may have a significant impact on the SMSR yield of the device. We will show how the Fourier approach can be used to model, and therefore mitigate, these errors by including the sine-transform term in the mirror loss modulation calculation. We particularly mean SMSR yield in this thesis, but production index-patterned lasers would have to meet several specifications for manufacturing yield. We will model both sub-wavelength and micrometre scale changes to our grating to facet distance and analyse how this affects the mirror loss spectrum. For the continued development of the Fourier design method [109], it is important to understand the impact of reflections between slots. To date, it has not been calculated for these perturbation gratings [110]. To do this, we compared the first-order Fourier approach with a semi-analytical SMM calculation that uses all orders of reflection [82].

In addition to mode selectivity against cavity threshold, $\Delta\alpha_{m_0}$ there are several other selection metrics that we will use when evaluating grating performance. Given that the profile of the spectral gain-bandwidth is not flat, modal competition often comes from the nearest-neighbour modes. Therefore, it is useful to quantify this particular selectivity, $\Delta\alpha_{nn}$. It is not always the case that the greatest modal competition comes from the nearest-neighbour modes — $20\Delta\alpha$ and $50\Delta\alpha$ measure the selectivity against a twenty- and fifty-mode bandwidth of modes, respectively, to quantify this phenomenon. The fifty-mode bandwidth will particularly attempt to quantify the modal suppression for large spectral shifts that can occur with cavity heating. Although index-patterned devices are typically made with a HR coating applied to the "Left facet", in this chapter we investigated designs with equal reflectivity facets to simplify the analysis.

4.1.1 A mathematical verification of the impact of weighted-average slot position on mode selectivity

We derive an integral expression based on Eq. 3.23 from Ch. 3

$$\Delta\alpha_{\Delta m} = \frac{2\Delta n}{Ln}\cos(m_0\pi)\cos(\Delta m\pi)\times \sum_{j=1}^{N} w(\epsilon)[\sin(2\pi\epsilon_j m_0)\cos(2\pi\epsilon_j\Delta m) + \cos(2\pi\epsilon_j m_0)\sin(2\pi\epsilon_j\Delta m)], \quad (4.1)$$

to estimate the maximum reduction in mirror loss of mode m_0 for a given design function, $f(\epsilon)$, when the weighting factor, $w(\epsilon)$, is taken into account. This will highlight the importance of the weighted-average of the slot position for m_0 selectivity. We first normalise the slot distribution function, $h(\epsilon) = \frac{f(\epsilon)}{w(\epsilon)}$, by integrating over the cavity region where the slots are placed

$$\int_0^{1/2} \frac{f(\epsilon)}{w(\epsilon)} d\epsilon = C, \quad (4.2)$$

with the normalised distribution function given by $\frac{1}{C}h(\epsilon)$. If we introduce N slots into the cavity, then the number of slots between ϵ and $\epsilon + d\epsilon$, dN, equals $\frac{N}{C}h(\epsilon)d\epsilon$. The slots in this region will reduce the threshold gain level by [24]

$$d(\Delta\alpha_{m_0}) = \frac{2\Delta n}{Ln} w(\epsilon) dN = \frac{N}{C}\frac{2\Delta n}{Ln} w(\epsilon) h(\epsilon) d\epsilon. \quad (4.3)$$

Replacing $w(\epsilon)h(\epsilon)$ by $f(\epsilon)$ and integrating over the length of the cavity, we obtain

$$\Delta\alpha_{m_0} = \frac{N}{C}\frac{2\Delta n}{Ln}\int_0^{1/2} f(\epsilon)d\epsilon. \tag{4.4}$$

Substituting Eq. 4.2 into Eq. 4.4 we then derive

$$\Delta\alpha_{m_0} = N\frac{2\Delta n}{Ln}\frac{\int_0^{1/2} f(\epsilon)d\epsilon}{\int_0^{1/2}\frac{f(\epsilon)}{w(\epsilon)}d\epsilon}. \tag{4.5}$$

Evaluating Eq. 4.5 then provides an estimate of the maximum reduction in mirror loss that can be achieved for the selected mode m_0, for a given function $f(\epsilon)$.

4.1.2 Grating-facet phase error

When a half-wavelength resonant cavity is formed with the left face of the slot and the "Left facet" of the cavity, Fig. 4.1 a), then the reflected waves from the slots align perfectly with the forward travelling m_0 wave; $\sin(2\pi\epsilon_j m_0) = 1$ and $\cos(2\pi\epsilon_j m_0) = 0$. ϵ_j is the position of the centre of the slot in unitless cavity ratio. Only the first term in the square bracket of Eq. 4.1 is non-zero, and the Fourier transform for the grating is via the cosine coefficient, i.e., $\cos(2\pi\epsilon_j\Delta m)$ to determine the selection of the modes. If the slot is shifted by $\frac{\lambda_0}{8n}$ (~ 60 nm) in the laser, as in Fig. 4.1 b), then we get $\sin(2\pi\epsilon_j m_0) = 0$ and $\cos(2\pi\epsilon_j m_0) = 1$. The first term in the square brackets of Eq. 4.1 becomes zero, and the Fourier transform for the grating is via the sine coefficient, i.e., $\sin(2\pi\epsilon_j\Delta m)$. An intermediate phase position can then be described by the linear addition of the cosine and sine transform functions. This creates a framework for analysing how the mirror loss spectrum of the cavity changes as the relative position of the grating from the cavity facets changes during device manufacture, as in Fig. 4.1.

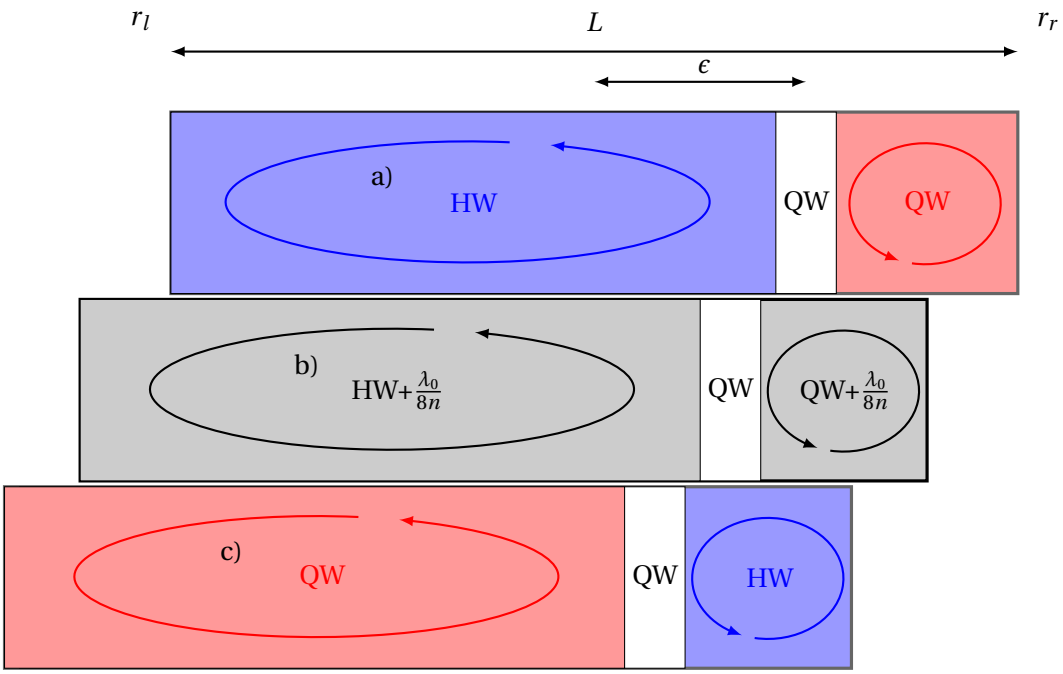


FIGURE 4.1: a) diagram of the ideal cavity design model, b) $\frac{\lambda_0}{8n}$ facet position error applied to each side, c) $\frac{\lambda_0}{4n}$ error.

4.2 Fourier analysis of exemplar design functions

The general approach we took for analysing new functions was trial and error, i.e., we selected various functions and compared the mirror threshold functions they produced. From our mathematical analysis in Sec. 4.1.1, we did have an initial guidance in selecting functions, i.e., functions with greater weighted average slot position than $f(\epsilon) = 1$. To present the research we chose $f_2(\epsilon) = |\epsilon|$ and $f_3(\epsilon) = \epsilon \sin(2\pi\epsilon)$ to compare to f_1, as these functions best highlight the key results of our analysis. The three exemplar design functions along with their sine and cosine transforms are stated in Tab. 4.1.

As well as the low weighted average slot position, f_1 is also the original and most studied Fourier design function [24, 36], making it a good basis comparison to include. After weighting f_2 to account for the changing E-field in the cavity, it produces a grating with a much higher weighted average slot than f_1. The slot spacing is also close to being constant, similar to the Bragg approach with a set slot spacing. Therefore f_2 is also a useful design to compare [19]. f_2 is more selective for m_0 but selects a wider bandwidth of modes around m_0. To improve on this, we sought a function that would narrow the frequency range of mode selection, while maintaining m_0 selectivity, e.g., $f_3(\epsilon) = \epsilon \sin(2\pi\epsilon)$. The Fourier modelling in this chapter uses the device parameters presented in Tab. 4.2. Note that our slot-width value is beyond what lithography can produce, and we are using this ideal dimension to simplify the Fourier analysis process.

No.	Function	Cosine transform	Sine transform
f_1	$f(\epsilon) = 1$	$\frac{\sin(\pi\Delta m)}{\pi\Delta m}$	$\frac{1-\cos(\pi\Delta m)}{\pi\Delta m}$
f_2	$f(\epsilon) = \lvert\epsilon\rvert$	$2[\frac{\sin(\pi\Delta m)}{\pi\Delta m} + \frac{\cos(\pi\Delta m)-1}{(\pi\Delta m)^2}]$	$2[\frac{\sin(\pi\Delta m)-\pi\Delta m\cos(\pi\Delta m)}{(\pi\Delta m)^2}]$
f_3	$f(\epsilon) = \epsilon \sin(2\pi\epsilon)$	$\frac{1}{2}[\frac{\pi(1-\Delta m)\cos(\pi\Delta m)+\sin(\pi\Delta m)}{\pi(1-\Delta m)^2}$ $+\frac{\pi(1+\Delta m)\cos(\pi\Delta m)-\sin(\pi\Delta m)}{\pi(1+\Delta m)^2}]$	$\frac{1}{2}[\frac{\pi(1-\Delta m)\sin(\pi\Delta m)-(\cos(\pi\Delta m)+1)}{\pi(1-\Delta m)^2}$ $+\frac{\pi(1+\Delta m)\sin(\pi\Delta m)+(\cos(\pi\Delta m)+1)}{\pi(1+\Delta m)^2}]$

TABLE 4.1: Cosine and sine transforms for the exemplar design functions, normalised so that the cosine transform equals one for $\Delta m = 0$.

L (µm)	400
n	3.2
Δn	0.02
λ_0 (nm)	1550
m_0	1652
N	20
R, % power	27
α_f (cm^{-1})	32.3
d (µm)	0.122

TABLE 4.2: Design parameters used.

4.2.1 $f_1(\epsilon) = 1$

The sinc function selects m_0 and leaves the other modes close to m_0 unchanged, as in Fig. 4.2 c). However, past ~ 1565 nm and ~ 1535 nm the grating no longer has control over the modes, i.e., the modal threshold gain is no longer clearly defined by the design function. Potentially, these modes can be relatively strongly selected reducing SMSR. f_1 also requires a significant number of our limited twenty slots near the centre of the device to correctly reproduce the function, as in Fig. 4.2 b) and c), limiting the m_0 selectivity. It is also important to note that due to the $\frac{1}{\sinh}$ weighting for $f_1(\epsilon) = 1$; as $\epsilon \to 0$, the bunching of slots (minimum slot-gap ~ 1.2 µm), makes the pattern difficult to create given the difficulty of etching and metal coating slots this close together. Furthermore, the very centre of the cavity cannot be sampled, as the weighted function explodes for $\epsilon < 0.0125$. For these reasons, we looked at functions that would minimise the number of slots near the centre of the cavity.

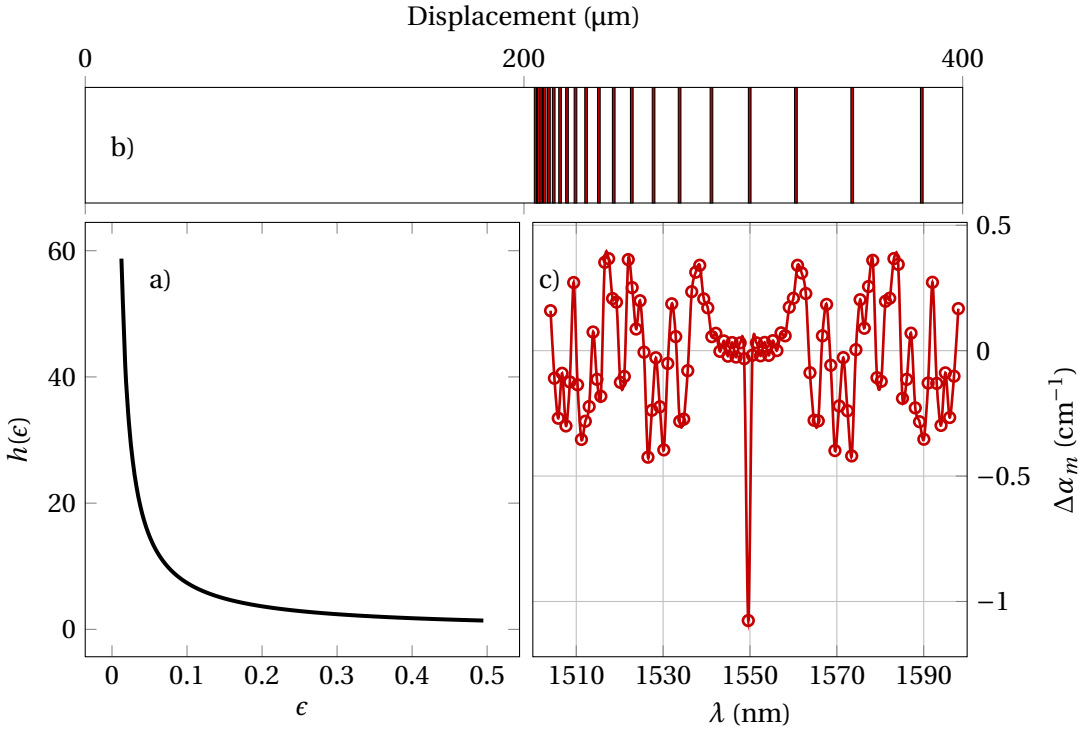


FIGURE 4.2: a) f_1 weighted design function for ϵ=0.0125→0.5, b) corresponding slot pattern, c) Fourier modal mirror loss modulation calculation. Designed and modelled using parameters in Tab. 4.2.

The initial implementation of f_1 for the Fourier design approach was based on repeating overlapping sinc patterns [24]. This resulted in an additional modulation for the density of the slots along the cavity. The modulation could be tailored to reduce the selection of additional modes in the cavity. However, during our investigation, we found that it gave marginal improvements in terms of net modal selection and a reduction in selectivity for m_0 for equal reflectivity facets. It was also a complicated slot pattern in terms of functional analysis. For these reasons, we used a single sinc pattern and analysed its Fourier properties. This gives a $\frac{1}{\epsilon}$ decreasing density of slots moving from $\epsilon = 0.0125 \rightarrow 0.5$.

4.2.2 $f_2(\epsilon) = |\epsilon|$

The function $f_2(\epsilon) = |\epsilon|$, has a linear increase in amplitude moving from $\epsilon = 0.0 \rightarrow 0.5$, as seen in Fig. 4.3 a). After weighting, this function becomes approximately, but not exactly, constant along the length of the half-cavity, Fig. 4.4 a). In Fig. 4.2 and Fig. 4.4, b) and c), we can see that the average slot position for f_2 is further from the "Left facet" than f_1, and the mode selectivity has increased, $\Delta\alpha_{m_0} = 1.1 \rightarrow 2.1$ cm^{-1}. However, we can see that the $m_{\pm1}$ modes are also selected for f_2. We can see how unmodulated the modes $m_{\pm2\rightarrow20}$ are for f_2 compared to f_1. However, f_2 has modes with large modulation at $\sim$ 1515 nm and 1585 nm. Although these modes have their thresholds increased in the ideal cavity, they will be strongly reduced with a $\pm\frac{\lambda_0}{8n}$ grating shift, as we will see in Sec. 4.2.5. f_1 does not have a modulation that approaches this magnitude outside of m_0.

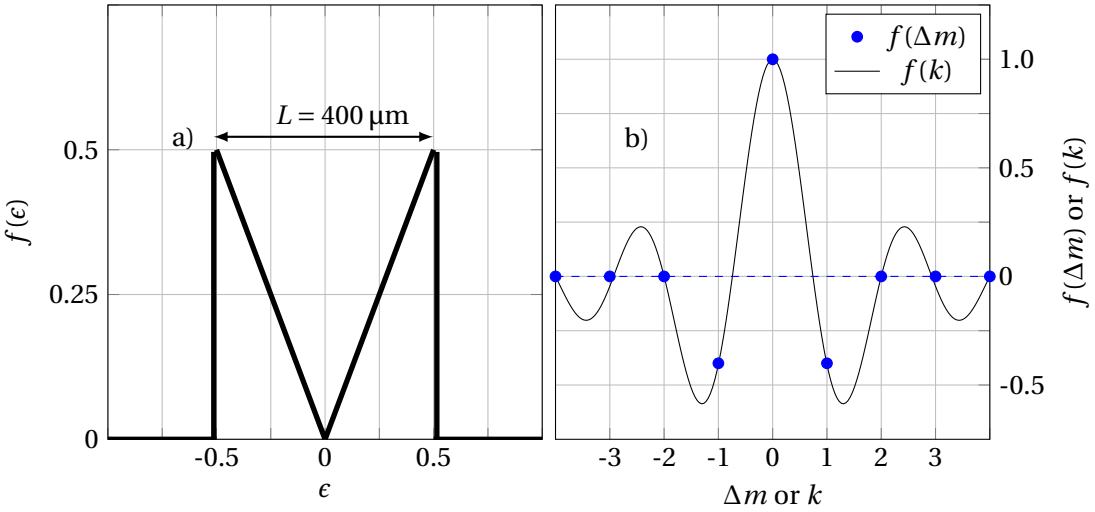


FIGURE 4.3: a) f_2 function for full cavity length, b) corresponding Fourier transform normalised to one.

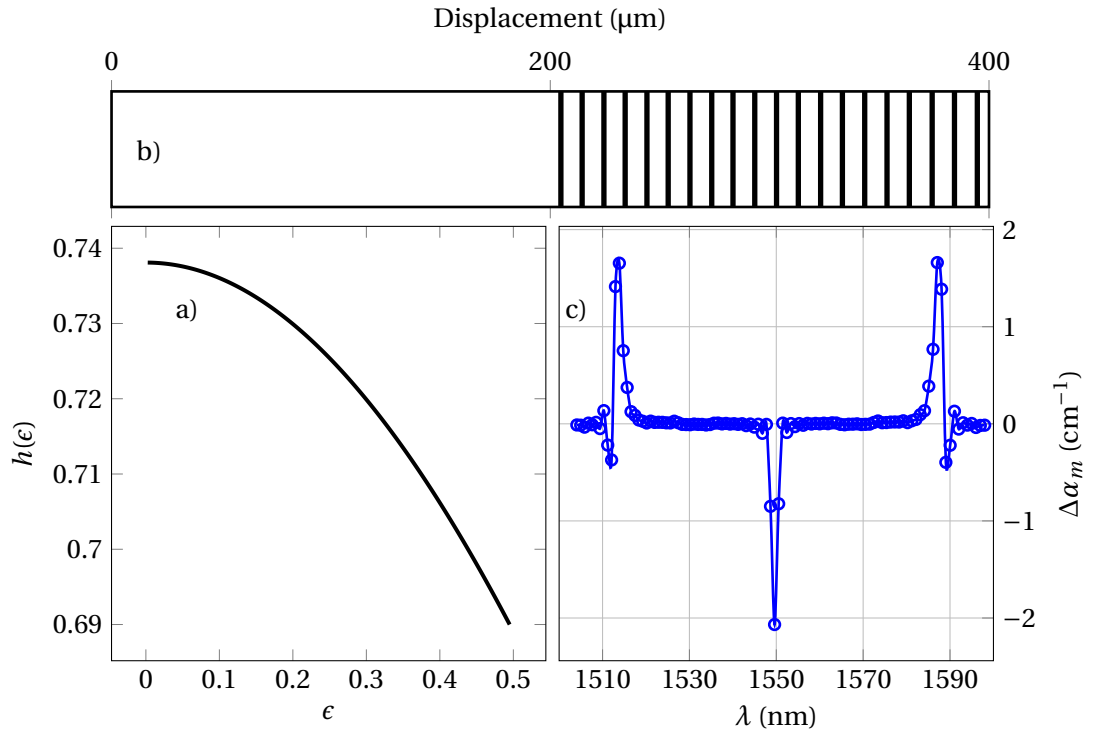


FIGURE 4.4: a) f_2 weighted design function for ϵ=0.0→0.5, b) corresponding slot pattern, c) Fourier modal mirror loss modulation calculation. Designed and modelled using parameters in Tab. 4.2.

4.2.3 $f_3(\epsilon) = \epsilon \sin(2\pi\epsilon)$

The function $f_3(\epsilon) = \epsilon \sin(2\pi\epsilon)$ looks to reduce the selectivity of the $m_{\pm1}$ modes over f_2 while maintaining the m_0 selectivity. We can see in Fig. 4.5 a), that f_3 has a peak in the design function around $\epsilon \sim 0.25$, increasing the density of slots in this region, as in Fig. 4.6 b). Unlike $f(\epsilon) = 1$, this region of high slot density is not near the centre of the cavity. In Fig. 4.4 and Fig. 4.6, b) and c), we can see that f_2 and f_3 have approximately equal average slot positions and the two functions have approximately equal m_0 selectivity. We can also see that f_3 has reduced selectivity of the $m_{\pm1}$ modes compared to f_2. Furthermore, f_3 does not experience the same strong modal modulation at ~ 1515 nm and 1585 nm as f_2.

There are several benefits to the f_3 design function, apart from its spectral qualities. It has been shown experimentally that patterns with slots that are closer together tend to have lower optical loss. There is no full theoretical explanation for this; however, in Ref. [9], it is partially attributed to scattering from the waveguide. The fact that the pattern has a low density of slots near the "Right facet" means that the pattern is not significantly disturbed if the facet is cleaved in the wrong position. In addition, the slots are not bunched together to the extent that the slots have to be removed from the grating to manufacture, Ch. 5.

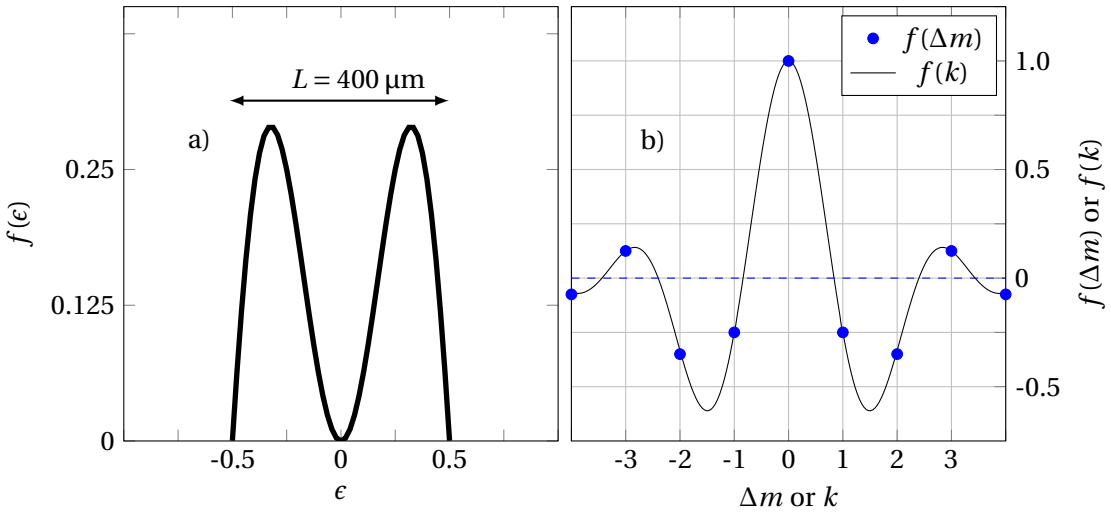


FIGURE 4.5: a) f_3 function for full cavity length, b) corresponding Fourier transform normalised to one.

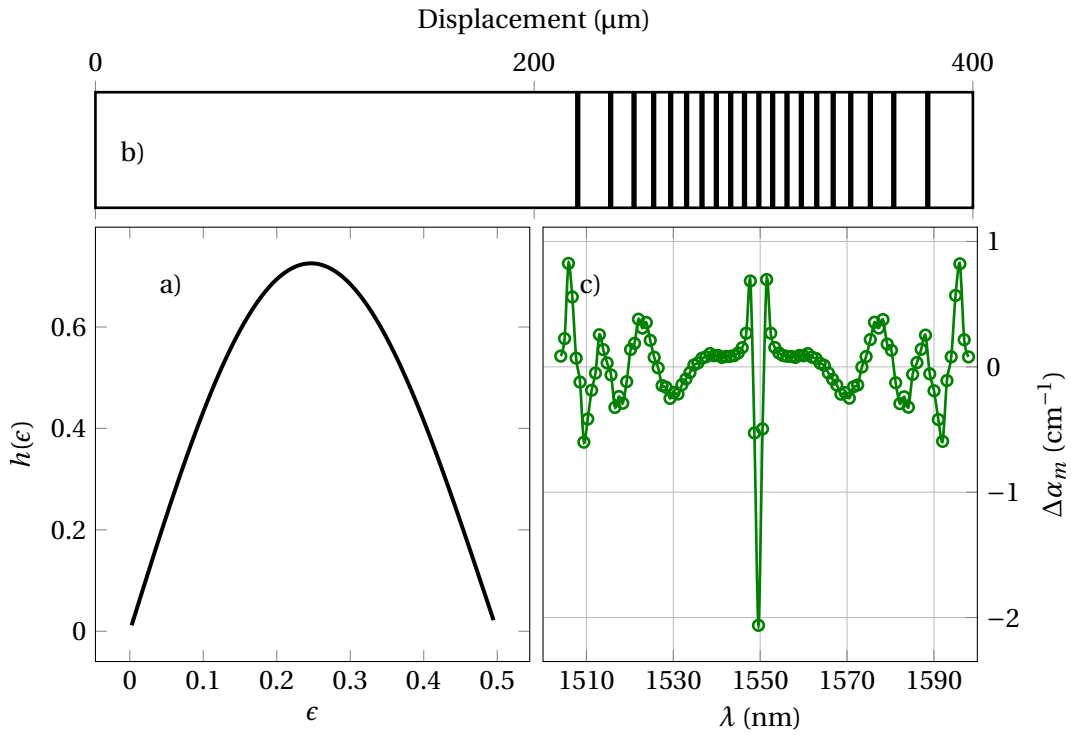


FIGURE 4.6: a) f_3 weighted design function for ϵ=0.0→0.5, b) corresponding slot pattern, c) Fourier modal mirror loss modulation calculation. Designed and modelled using parameters in Tab. 4.2.

4.2.4 Verification of the first-order approximation and quantifying higher-order reflections in the cavity

To verify the first-order of reflection approximation and calculate the level of higher-order reflections in the cavity, we subtracted the SMM mirror loss threshold modulation, with all orders of reflection, from the Fourier modulation which included just the first-order of reflection. The blue lines in Fig. 4.7 show the SMM-calculated modal mirror loss spectra for the three different exemplar functions, with ideal slot positioning. The red lines show the SMM subtracted from the Fourier-calculated value. The largest discrepancy in the spectrum for each function is $\sim -0.2\ \mathrm{cm}^{-1}$ for modes close to m_0. This verifies how effective the first-order reflection approximation is for perturbation-slot devices with moderate cavity lengths and facet reflectivities ($L = 400\,\mu\mathrm{m}$, $R = 27\%$). We can see that f_1 has the smallest discrepancy between the Fourier and SMM calculations. This is likely the result of f_1 having the lowest input from inter-slot scattering, which the Fourier method does not include. Many of the f_1 slots are bunched together at the centre of the cavity, where the optical power is modelled to be low and the impact of scattering between the slots is low. Optical power is low in the centre of the cavity due to the exponential effect of gain in the cavity. The dominant light source in the cavity is reflection from the cavity facets. After reflection, light then transverses the cavity, exponentially increasing in amplitude, both forward and reverse. This makes the region in the centre of the cavity the place with the smallest sum of forward and reverse fields.

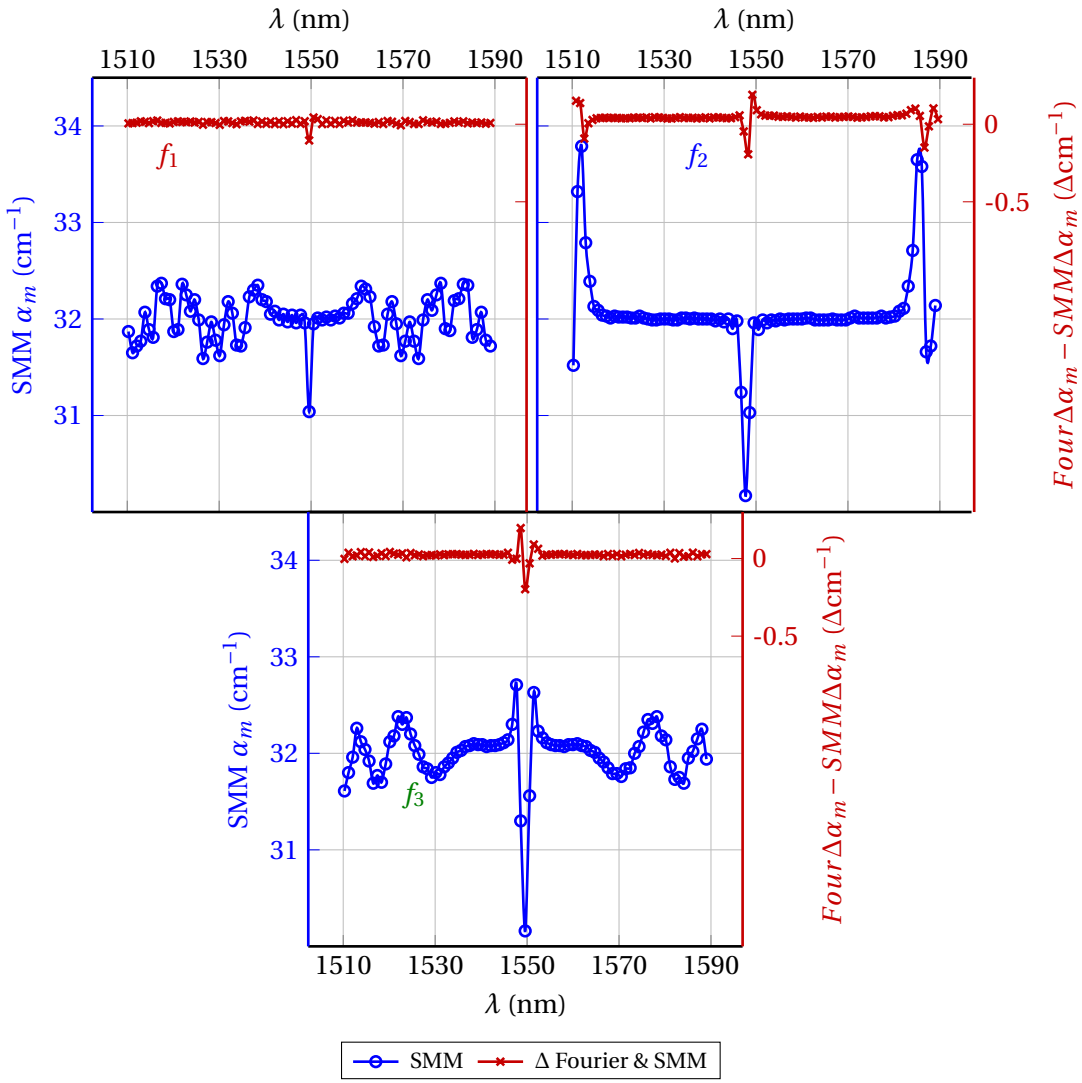


FIGURE 4.7: SMM calculated mirror loss spectra (blue) with ideal slot positioning to all orders of reflection for the functions in Tab. 4.1, the SMM subtracted from the first-order Fourier model (red). For functions in Tab. 4.1, modelled using parameters in Tab. 4.2

The SMM calculation has a mostly negative modal mirror threshold discrepancy compared to the Fourier calculation. One reason for this is that resonant inter-slot scattering decreases the mirror threshold for most modes; however, for some modes, this effect is destructive; hence the positive discrepancy values. The discrepancy is the value we use to quantify inter-slot scattering. Overall, these inter-slot scattering effects are small, and there is a good convergence between the two calculations. The largest discrepancies are near m_0. This is due to a small amount of close-to-resonant scattering between different slots at m_0 and for neighbouring modes.

It is important to note that the Fourier method calculates an exact theoretical mirror threshold. The SMM cannot calculate this exact value, and returns a threshold value for a high output power which should be close to the theoretical limit. Although there are two factors contributing to the discrepancy between the SMM and the Fourier calculation, any discrepancy value we calculate places an upper limit on the effect of inter-slot scattering.

4.2.5 Change in modal threshold function with grating-facet phase

We applied a $\frac{\lambda_0}{8n}$ shift to each slot in the f_1, f_2 and f_3 grating patterns and recalculated Eq. 4.1. For f_2 in Fig. 4.8 we can see that the modes that are strongly suppressed in the in-phase position around 1510 nm and 1590 nm, are strongly selected in the out-of-phase position. The two modes at 1590 nm are as strongly selected as the $m_{0\pm1}$ modes near 1550 nm and could result in a low SMSR device if the gain-bandwidth peak is near 1590 nm. We can see how the selected mode has changed to m_{0+1} for each of the designs for the $\frac{+\lambda_0}{8n}$ shift; m_{0-1} would have been selected for a $-\frac{\lambda_0}{8n}$ shift.

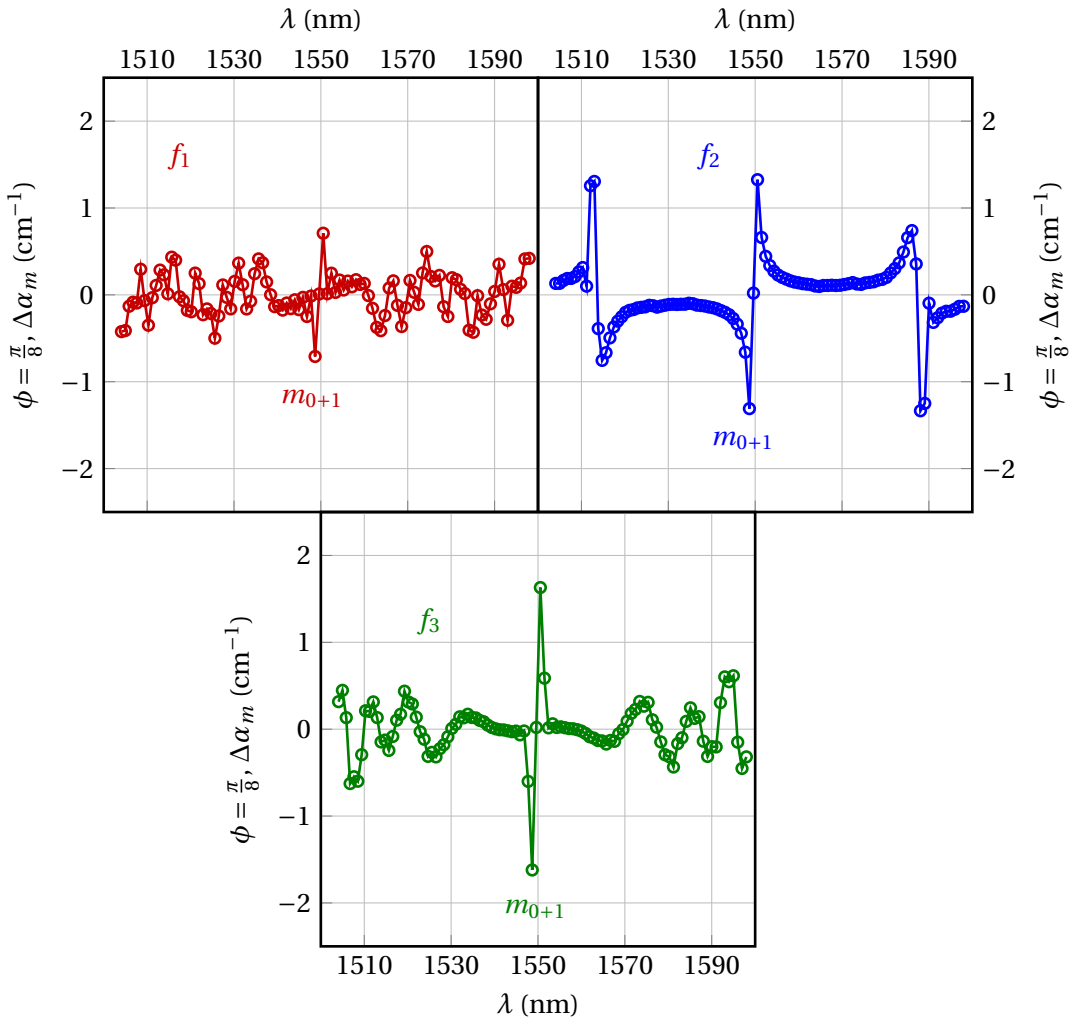


FIGURE 4.8: Fourier calculated mirror loss spectral function comparison for a $+\frac{\lambda_0}{8n}$ phase shift in grating position. For functions in Tab. 4.1, modelled using parameters in Tab. 4.2.

In Fig. 4.9 we track how selectivity and the mode with the lowest mirror loss change as the grating changes position by a distance $+\frac{\lambda_0}{16n}$ and $+\frac{\lambda_0}{8n}$ for f_1. For Fig. 4.10 we performed the same calculation over a range of $+\frac{\lambda_0}{2n}$ for one hundred phase steps — and plotted the selectivity of the mode and the mode number with the lowest mirror loss, Δm_0, as a function of the change in grating position. We measure selectivity against modes within twenty- and fifty-modes of m_0 for each phase position to analyse varying selectivity with mode bandwidth.

Three parameters change for incorrect facet positioning for our device. One, the phase between the grating and the facet; two, the impact of the slot due to its position in the cavity as the cavity length changes. These two parameters are linked and can be captured by changing the slot positions in the cavity for Eq. 3.23, while keeping the cavity length fixed as an integer multiple of half-wavelengths for the designed wavelength value. These are the two parameters that we examine in this chapter. The third is a change in cavity modes due to the cavity length being a non-integer multiple of half wavelengths for the designed wavelength value. This is a separate parameter variation that we will examine in Ch. 5.

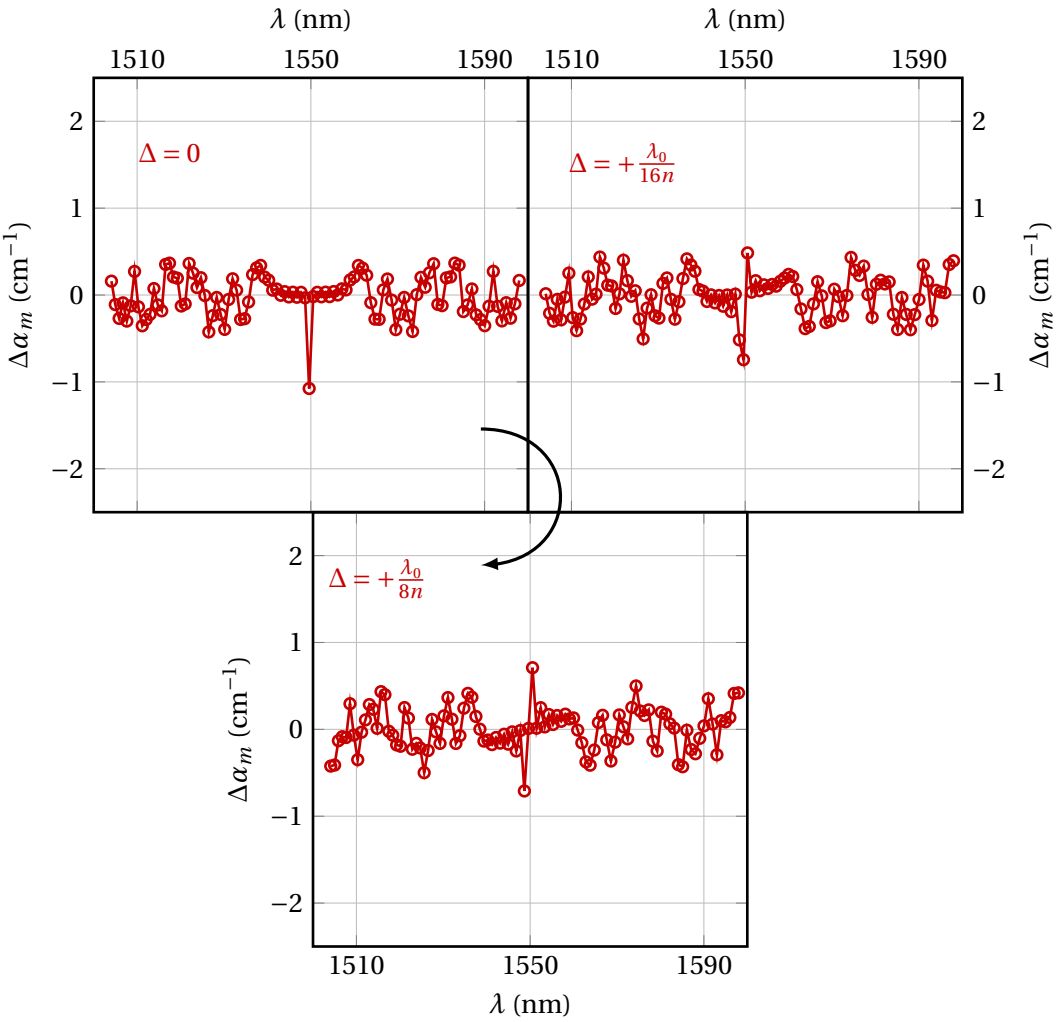


FIGURE 4.9: The f_1 function, tracking the change in mirror gain threshold function with Δ shift in grating position. Modelled using parameters in Tab. 4.2.

Panel c) in Fig. 4.2, Fig. 4.4 and Fig. 4.6 show the in-phase or cosine modal mirror loss patterns for the exemplar functions, and Fig. 4.8 shows the out-of-phase or sine transform of the functions. Fig. 4.10 shows the magnitude of the modal selectivity and the relative mode number selected for the intermediate phase positions. Analysing these graphs, we can see that selecting a design function with clear single-mode selectivity in the sine and cosine transforms is much more likely to produce a lasing device within the range of $m_{0\pm1}$ than a function that does not. The functions with greater modal selection, f_2 and f_3, show sharper points of inflection in the selectivity versus grating-facet phase traces, Fig. 4.10 a) and b). f_3 also shows strong selectivity against competing modes for the wider fifty-mode range.

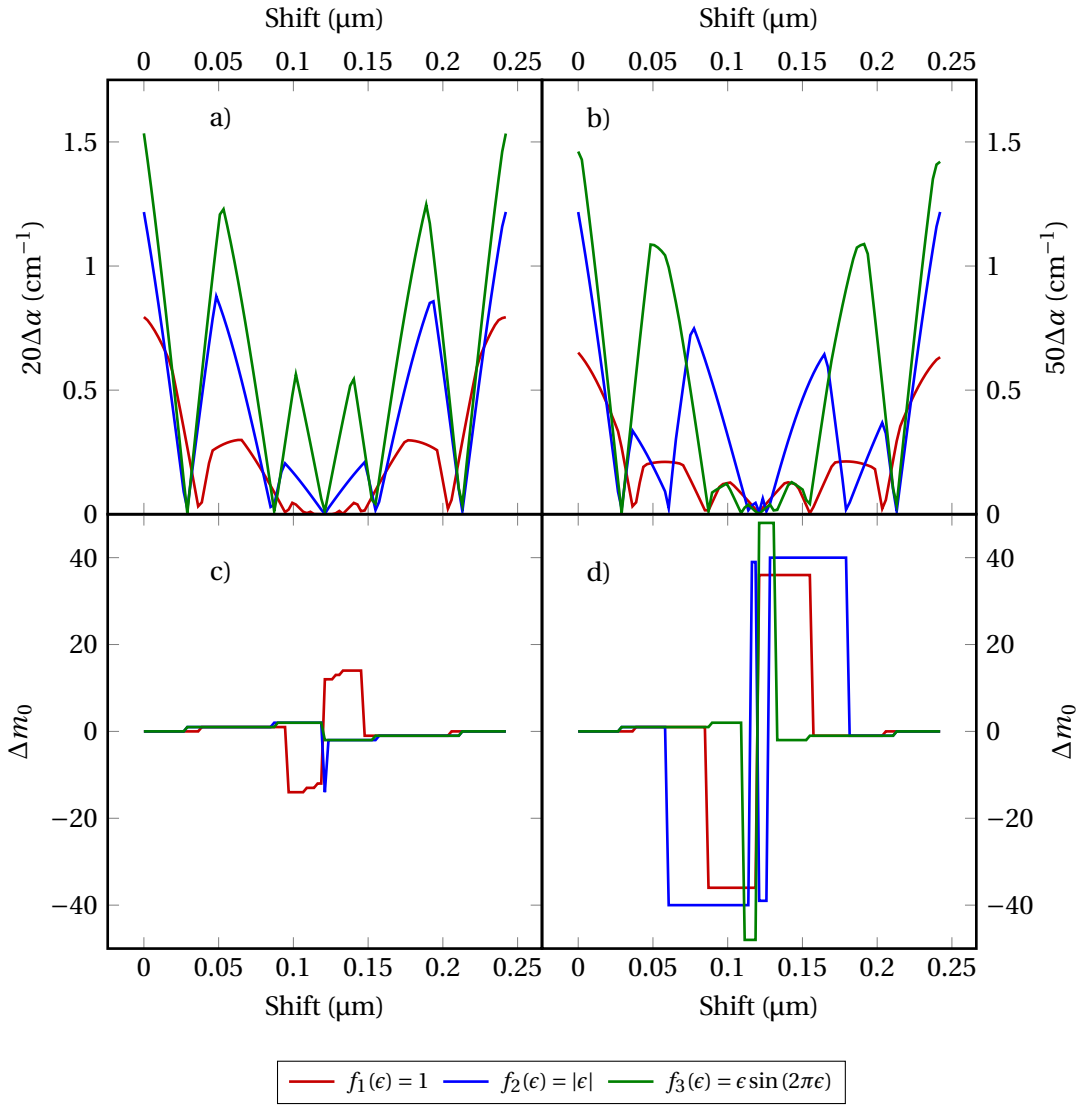


FIGURE 4.10: Calculated mode selectivity and mode number selected as the perturbations are cycled through a $+\frac{\lambda_0}{2n}$ phase range with a twenty-mode mask ($20\Delta\alpha$) a) and c) and a fifty-mode mask ($50\Delta\alpha$) b) and d). Modelled using parameters in Tab. 4.2.

4.2.5.1 Large changes in the relative grating-facet position

What is also important in terms of manufactured devices is the impact of grating-facet position changes on the order of micrometres due to errors during facet cleaving. In Fig. 4.11, the grey-shaded area represents the amount of cavity length lost in a ~ +10 µm cleave error to the "Right facet". To simulate this in the model, we add +10 µm to the position of each slot in the grating and repeat the sub-wavelength phase scan of selectivity. The cavity remains 400 µm in length and only the grating is moved. We also calculated a −10 µm change to simulate a cleave on the "Left facet" of the laser, not shown in Fig. 4.11.

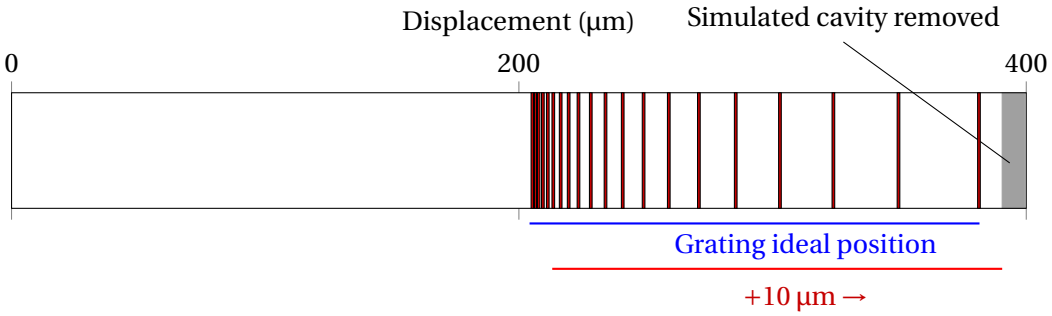


FIGURE 4.11: Diagram of the shift in the grating position to simulate a section of misaligned cleave to the "Right facet", removing 10 µm of the cavity.

The results shown in Fig. 4.12 and Fig. 4.13 remain very similar to those of Fig. 4.10 for f_2 and f_3, with f_1 showing a stronger variation due to the large density of features close to $\epsilon = 0$. The selectivity of the function f_1 improves significantly for the shift +10 µm, but it degrades significantly for the shift −10 µm. This is in agreement with the importance of weighted-average perturbation position highlighted by Eq. 4.5. We also note that f_3 is more robust to facet cleaving errors when taking into account the safety margin between the last perturbation in the grating and the facet. A +10 µm grating shift removes one of the slots in f_2, which means that this function is less resistant to cleaving errors.

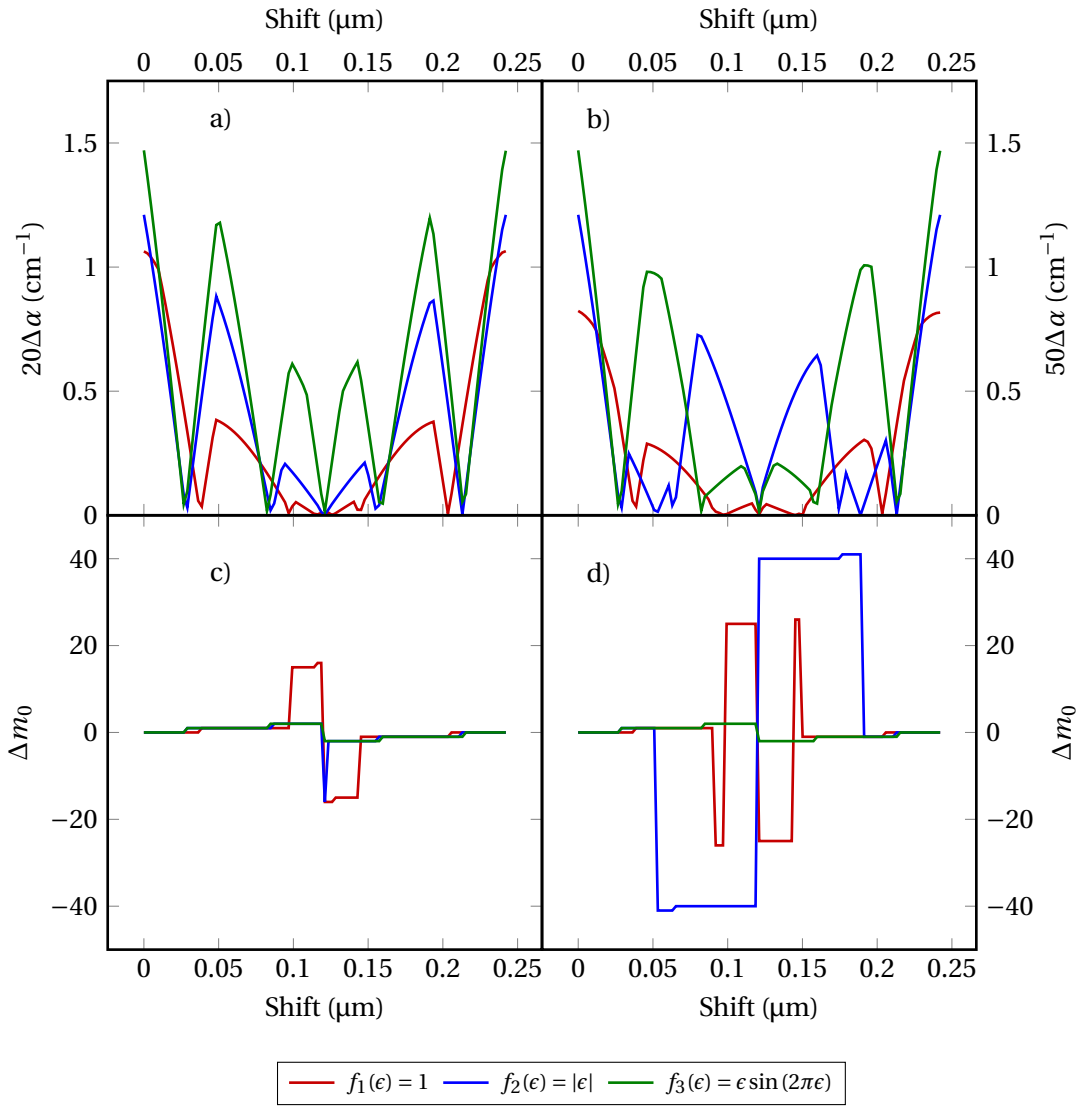


FIGURE 4.12: Mode selectivity and mode number selected as the slots are cycled through a $+\frac{\lambda_0}{2n}$ phase range, with respect to the facet position, with an additional +10 μm grating position change. Calculations are made with a twenty-mode mask in a) and c) and a fifty-mode mask in b) and d). Modelled using parameters in Tab. 4.2.

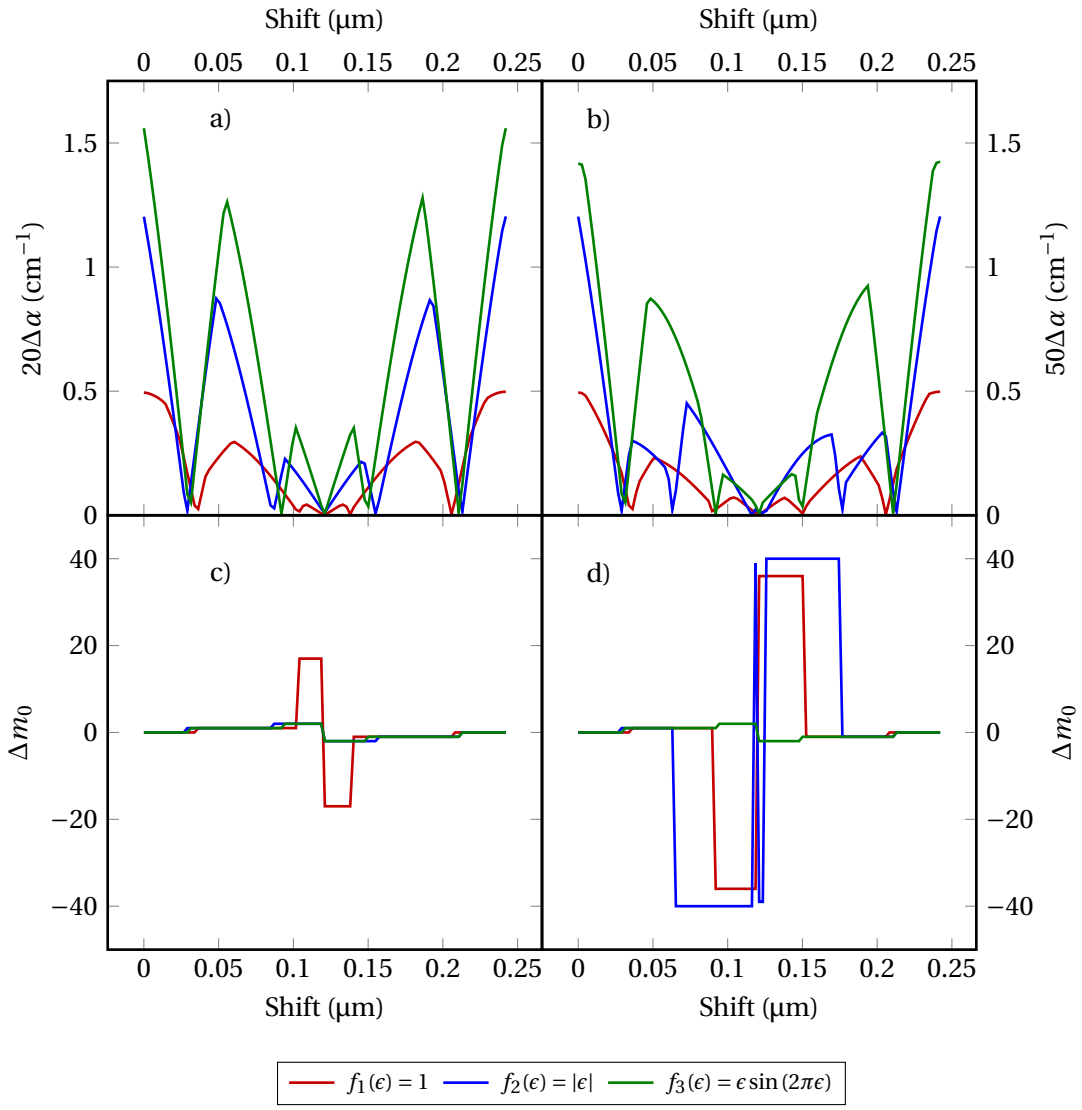


FIGURE 4.13: Mode selectivity and mode number selected as the slots are cycled through a $+\frac{\lambda_0}{2n}$ phase range, with respect to the facet position, with and additional −10 μm grating position change. Calculations are made with a twenty-mode mask in a) and c) and a fifty-mode mask in b) and d). Modelled using parameters in Tab. 4.2.

4.3 Analysis

4.3.1 Mode selectivity with weighted-average slot position

In Tab. 4.3 we compare our selectivity metrics for the exemplar gratings. The function f_3 outperforms f_2 and f_1 in the in-phase selection characteristics, and is only equalled by f_2 in terms of selectivity against cavity mirror loss. Tab. 4.3 verifies the benefits for m_0 selectivity of not placing slots near the cavity centre due to the $w(\epsilon) = 2|r|\sinh(\alpha_f \epsilon L)$ weighting for a laser with equal reflectivity facets.

Function	$\Delta\alpha_{m_0}$ (cm^{-1})	$\Delta\alpha_{nn}$ (cm^{-1})	$20\Delta\alpha$ (cm^{-1})	$50\Delta\alpha$ (cm^{-1})	$\Delta\alpha_{m_0}$ Eq. 4.5 (cm^{-1})
f_1	1.1	1.0	0.8	0.7	0.8
f_2	2.1	1.2	1.2	1.2	2.0
f_3	2.1	1.5	1.5	1.5	2.0

TABLE 4.3: Comparison of the selection performance of each function when the grating is perfectly aligned to the facet, including the estimated selection calculated using Eq. 4.5. Functions in Tab. 4.1 modelled using parameters in Tab. 4.2.

The first column in Tab. 4.3 shows the calculated values using Eq. 4.1, which explicitly takes into account the positions of the perturbations. We can compare this with the final column showing the maximum reduction in mirror loss for mode m_0, calculated using our mathematical analysis of mode selection in Sec. 4.1.1. For f_1 we place the perturbations between ϵ_{min} and $\epsilon = \frac{1}{2}$, for which the ratio of the two integrals in Eq. 4.5 is $\frac{\frac{1}{2}-\epsilon_{min}}{-\ln(2\epsilon_{min})}$. This gives an estimated m_0 mirror loss modulation of 0.8 cm^{-1}, lower than the fully calculated value of 1.0 cm^{-1}. The integral approach provides an excellent estimate of the reduction in mirror loss for the functions f_2 and f_3, but is less accurate for f_1 due to the divergence in the perturbation distribution function, $h(\epsilon)$, as $\epsilon \to 0$. Nevertheless, the model provides a clear explanation for the smaller threshold reduction observed for f_1, where the integrated impact value does not adequately capture the impact of slots on a divergent section of a function.

The function $\sinh(\alpha_f \epsilon L)$ can be approximated as linear, as demonstrated in Fig. 4.14. Therefore, we can let $w(\epsilon) = \alpha_f \epsilon L$, where $\alpha_f L = 2\ln\left(\frac{1}{|r|}\right)$ [24]. This makes the calculation of Eq. 4.5 analytical. For the functions f_2 and f_3 we get

$$\Delta\alpha_{m_0} = \frac{\int_0^{1/2} f(\epsilon)\,d\epsilon}{\int_0^{1/2} \frac{f(\epsilon)}{w(\epsilon)}\,d\epsilon}\left(\frac{N\Delta n}{Ln}\right) = \frac{\alpha_f L}{2}\left(\frac{N\Delta n}{Ln}\right) \tag{4.6}$$

or 2.0 cm^{-1} which is consistent with Eq. 4.1. The 2.0 cm^{-1} value shows the maximum cavity threshold selectivity for a grating pattern with a relatively even-covering of half the length of a cavity with $L = 400$ µm, using the cavity parameters in Tab. 4.2.

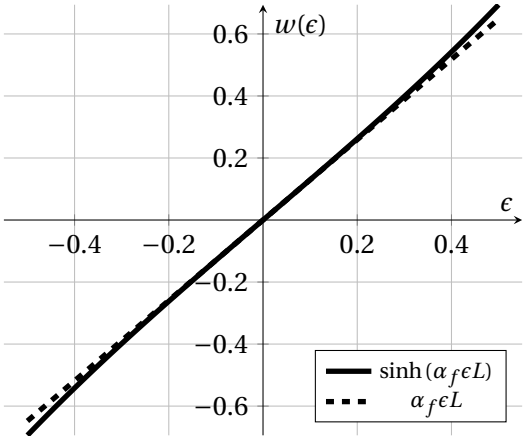


FIGURE 4.14: Comparison of the $w(\epsilon)$=$\sinh(\alpha_f \epsilon L)$ and $w(\epsilon)$=$\alpha_f \epsilon L$, for the device parameters in Tab. 4.2 ($L = 400$ µm, $\alpha_f = 32.2$ cm^{-1}).

4.3.2 The Fourier properties of index-patterned gratings

Panels b) and c) in Fig. 4.2, Fig. 4.4, and Fig. 4.6 show the perturbation distribution patterns for the three exemplar design functions and their respective corresponding modal mirror loss spectra in the ideal case. We see that f_2 and f_3 select the $\Delta m = \pm 1$ modes more strongly compared to f_1. For f_2, the selection ratio is $\frac{0.8\text{cm}^{-1}}{2.1\text{cm}^{-1}} = 38\%$, and $\frac{0.5\text{cm}^{-1}}{2.1\text{cm}^{-1}} = 24\%$ for f_3. This is expected from the Fourier transforms listed in Tab. 4.1 $\left(\frac{4}{\pi^2}\right.$ and $\left.\frac{1}{4}\right)$, respectively). The side-mode selectivities were calculated taking the average of the two side-modes of m_0. This value will be closer to the cosine transform value—averaging out any sine transform components.

For the function f_2, the gaps between the slots are very close to constant. Assume a grating of twenty equally spaced slots, where the p^{th} slot position is at

$$\epsilon_p = 0.025p - 0.0125. \tag{4.7}$$

To simplify the example further, assume that we are operating on mode 1600. There are then 1600 half-wavelengths along the cavity, 800 of them between 0 and 0.5. The length of each half-wavelength is $\frac{0.5}{800} = 6.25 \times 10^{-4}$. The left face of the first slot is at 0.0125 — there are then $\frac{0.0125}{0.000625} = 20$ half-wavelengths between 0 and the first slot left face, or $820 + 20 = 840$ full half-wavelengths from the "Left facet" of the cavity. There are a further $\frac{0.025}{0.000625} = 40$ half-wavelengths between the left face of the p^{th} and $(p+1)^{st}$ slots. In this simple example that we have set up, we get a constructive mode selection from each slot for $m_0 = 1600$.

If we now consider mode 1640, then there are 820 half-wavelengths between 0 and 0.5, with each half-wavelength of length $\frac{0.5}{820} \simeq 6.0976 \times 10^{-4}$. The first slot is at 0.0125, so that there are $\frac{0.0125}{(0.5/820)} = 20.5$ half-wavelengths between 0 and the left face of the first slot, or $820 + 20.5 = 840.5$ half-wavelengths from the "Left facet" of the cavity, i.e., we now have an odd number of quarter wavelengths to the "Left facet" from the left face of the slot. There are a further $\frac{0.025}{(0.5/820)} = 41$ half-wavelengths between the left faces of the p^{th} and $(p+1)^{st}$ slots. In this example, we get destructive mode suppression from each slot for $m = 1600 \pm 40 = 1560$ and 1640.

If we had this exactly evenly spaced slot pattern for our devices, then the modes 1692 and 1612 should each have a negative selection exactly equal and opposite to the positive selectivity of the mode 1652. In the weighting-function design approach, we do not have a perfectly regular slot pattern, which means that modes 1692 and 1612, are selected by ~ 80% of m_0. Similar unintended Bragg reflections at modes with large Δm can also occur for other functions, e.g., f_3 beyond 1590 nm; but the overall scale of the effect is generally not as large as for the perfectly regular case. A large modal modulation at $\Delta m = \pm 40$ can potentially lead to low SMSR, if there is variation in the cavity temperature.

It is known that the Fourier series converges slowly when there is a discontinuity in the value of the function that is approximated by the Fourier series. We are approximating the Fourier transform not by including a finite number of Fourier terms but rather by approximating the function by a finite number of delta functions, i.e., each slot facet is a discrete single point of design function sampling. It is likely that this also converges more slowly when the delta functions approximate to a situation where the weighted function is diverging at $\epsilon = 0$. There are three features of our results that display this aspect. One, the strong sensitivity of f_1 m_0 selectivity to large shifts ($\sim \pm 10$ µm) in the grating to/from centre. Two, the fact that the integral approximation works less well for f_1 than for f_2 and f_3. Three, the increase in "noise" in the mirror loss spectrum as one increases the magnitude of Δm and moves away from m_0.

The small change in selectivity for f_2 and f_3, when the facets are shifted by as much as 10 µm, can be understood by considering how the Fourier transforms in Tab. 4.1 are modified if the pattern is changed, and therefore the limits of integration are changed. As an example, if f_2 is shifted to start at $\epsilon = a$ rather than 0, then the Fourier transform in Tab. 4.1 is modified by shifting the integration range of the Fourier transform from $\epsilon = 0 \rightarrow 0.5$ to $\epsilon = a \rightarrow 0.5$

$$\frac{\sin(\pi\Delta m)}{\pi\Delta m} + \frac{\cos(\pi\Delta m) - 1}{(\pi\Delta m)^2} \rightarrow \frac{1 - a\pi\Delta m \sin(a\pi\Delta m) - \cos(a\pi\Delta m)}{(\pi\Delta m)^2}. \tag{4.8}$$

This introduces a correction of order a^2 to the calculation for modes close to the selected mode $m_{0\pm1}$, as long as the number of perturbations N remains unchanged. We can also see the functions displaying Fourier properties out-of-phase; f_1 in Fig. 4.8 resembles the sine transform for the "Top-hat" function in Fig. 4.15.

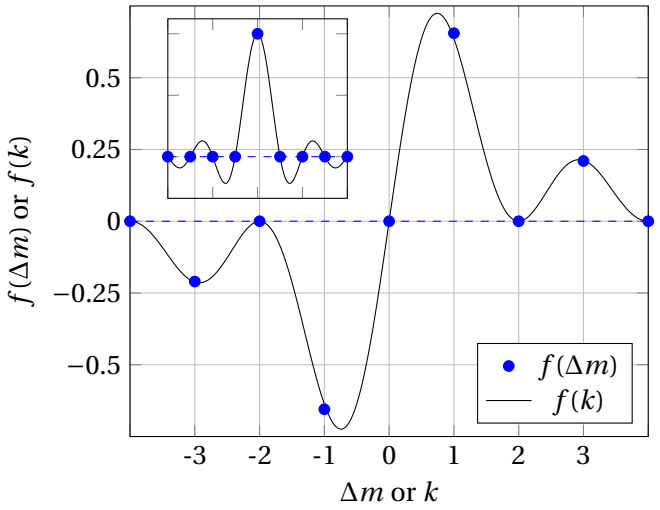


FIGURE 4.15: The sine transform of the "Top-hat" function in Fig. 3.4 a) (inset).

4.3.3 Grating-facet phase and yield

We can see how well f_3 performs in the out-of-phase scenario in Tab. 4.4; with an even greater improvement over f_1 and f_2 than in the in-phase case, Tab. 4.3. We saw in Sec. 4.2.5 that modes that are strongly suppressed in the in-phase case can be strongly selected out-of-phase. Therefore, you do not want strongly modulated modes outside of $m_{0\pm1}$. $m_{0\pm1}$ is a tolerable band of mode selection for most applications, and it is difficult to design gratings not to select the $m_{\pm1}$ modes as the grating-facet phase changes, given their Fourier nature.

Function	$\Delta\alpha_{m_0}$ (cm^{-1})	$\Delta\alpha_{nn}$ (cm^{-1})	$20\Delta\alpha$ (cm^{-1})	$50\Delta\alpha$ (cm^{-1})
f_1	0.7	0.7	0.3	0.2
f_2	1.3	0.7	0.7	0.0
f_3	1.6	1.0	1.0	1.0

TABLE 4.4: Comparison of the spectral performance out-of-phase, i.e. a $\frac{\lambda_0}{8n}$ step has been added to each ideal slot position. Functions in Tab. 4.1, modelled using parameters in Tab. 4.2.

As an example of the yield improvements offered by changing the design function, we set a baseline selectivity of 0.35 cm^{-1} for the mode with the lowest mirror threshold over a $\frac{\lambda_0}{2n}$ grating-facet phase cycle. 0.35 cm^{-1} was chosen, as it was a selectivity value that had previously delivered SMSR > 40 dB [111]. The function f_3 gave a ×3 improvement in yield over f_1, while f_2 gave a ×2 improvement over f_1. The mode number with the lowest mirror loss does vary in this calculation. As can be seen in Fig. 4.10, for f_3 this is significantly more likely to remain on $m_{0\pm1}$ due to its Fourier properties.

In Fig. 4.12 and Fig. 4.13, f_3 maintains good single-mode selectivity even with large changes in the grating position. It can also be seen that f_3 has good selectivity as the mode selection mask increases to fifty-modes, which means that f_3 should be resistant to large temperature variations even as the distance between the grating and the facet varies significantly. In general f_3 is a more robust design function.

Function	Yield %
f_1	22.3
f_2	48.1
f_3	66.3

TABLE 4.5: A $20\Delta\alpha$ mode selectivity yield for a baseline of 0.35 cm^{-1}. Functions in Tab. 4.1, modelled using parameters in Tab. 4.2. Mode number selected not necessarily m_0.

4.3.4 Thermal analysis; gain-bandwidth case study

We have treated the threshold gain level as independent of wavelength. In practice, the gain spectrum shows a peak at a particular wavelength, which is temperature-dependent. To illustrate the impact that this can have on mode selection we take, as an example, the applied modal gain spectrum function, Γg_m, fitted for a multiple quantum well structure in Ref. [112]. The structure in the paper used 10.5 nm InGaAsP quantum wells, targeted at 1500 nm. In the next chapter, we implement our slotted laser designs on AlGaInAs targeted to 1550 nm using 6 nm width quantum wells. We added the modal mirror modulation function to the Ref. [112] gain spectrum

$$\Delta g_m = \Gamma g_m + \alpha_m. \tag{4.9}$$

We then zero against the maximum threshold gain modulation

$$\Delta G_m = \Delta g_m - \min(\Delta g_m), \tag{4.10}$$

to show the relative selection of each mode. Our chosen wavelength, λ_0, is at 1540 nm. Tab. 4.6 shows the modified parameters used in this section. The mode selectivity parameters are modelled to remain the same as in Tab. 4.3 with the wavelength change.

λ_0 (nm)	1540
m_0	1662
slot width (μm)	0.121

TABLE 4.6: Changed modelling parameters used in the gain-bandwidth case study. All other parameters remain the same as Tab. 4.2.

The left column of Fig. 4.16 shows the relative modal gain selectivity spectra when the gain-bandwidth peak is at 1532 nm. The 1540 nm mode is clearly selected for f_2 and f_3, but not for f_1. If we shift the gain-bandwidth peak by 18 nm relative to the selected mode to 1550 nm, then the mode at 1540 nm is selected in each case as in the right column of Fig. 4.16. This mimics the key effect of temperature, that is, the gain-bandwidth peak shifts to a longer wavelength as the temperature increases. In practice, the width of the gain-bandwidth spectrum increases and the wavelength of the selected mode also shifts (more slowly) to a longer wavelength, with a typical relative change in the separation between the gain-bandwidth peak and the selected mode of 0.4 nm°C^{-1} (including refractive index change) [99].

A detailed simulation based on a method, such as that in Ref. [20], would be required to calculate the lasing spectrum and the value SMSR. Based on the results in Fig. 4.16, and ignoring the temperature dependence of the gain-bandwidth spectral width and any wavelength-dependent losses, we can nevertheless estimate that lasing on m_0 should be achievable over a temperature range of order 45°C for function f_2 and 46°C for function f_3, with a net mode selectivity of > 0.25 cm^{-1}. There is insufficient information in the model to convert this selectivity value to SMSR. Function f_1 will stop lasing on m_0 after a 38°C temperature increase.

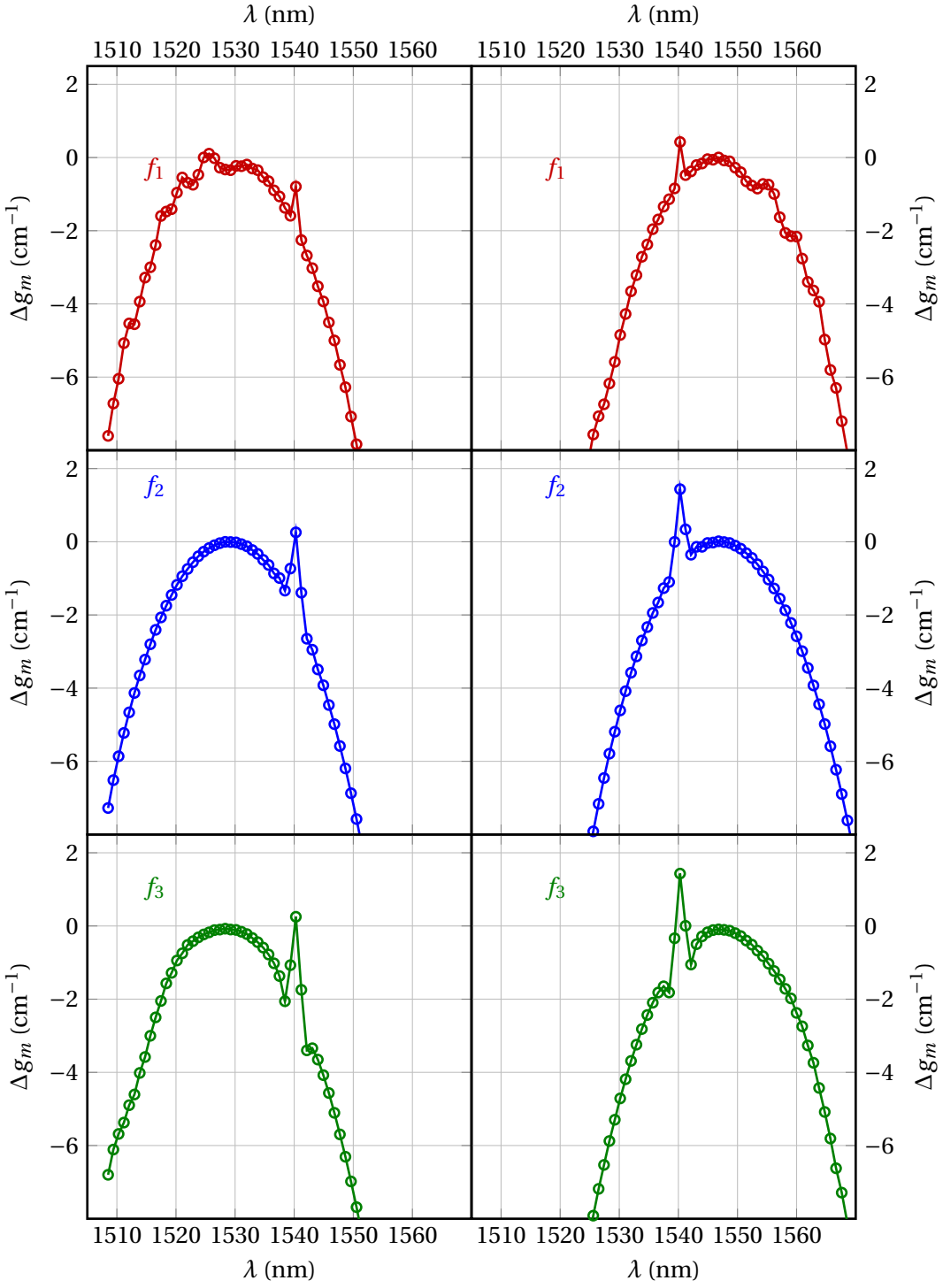


FIGURE 4.16: Left column, relative modal selectivity spectra with a function peak at 1540 nm fitted with a gain spectrum centred at 1532 nm. Right column, an 18 nm thermal shift applied to the peak energy in each device. Functions in Tab. 4.1, modelled using parameters in Tab. 4.2 and Tab. 4.6.

4.4 Discussion

We performed a Fourier analysis of three exemplar design functions to gain insight into the physics of index-patterned devices. The key findings of this chapter are; the weighted-average of the slot position in the grating can be used to improve the selectivity of the m_0 mode, and the sine transform of the slot pattern can be used to analyse the reduction in yield from incorrect facet positioning. We also demonstrated many of the Fourier properties of index-patterned lasers, further justifying this modelling method. We have seen how greater mode selectivity against cavity threshold gave greater thermal stability, and how gratings with constant spacing can be more susceptible to temperature changes in the cavity from modal pattern repetition. We verified our first-order Fourier model for devices with equal facet reflectivities by comparing it with an equivalent SMM structure. The first-order model can sufficiently position perturbations in terms of phase to create a specific mode pattern in the spectrum. In Ch. 5 and Ch. 6, we will see that this is sufficient to create devices with $>$ 40 dB SMSR and $>$ 10 mW output power at 100 mA ($\sim 5 \times I_{th}$).

We have used our exemplar functions to analyse mode selectivity against mirror threshold and against competing modes in the spectrum, and also how the selectivity depends on the grating-facet phase. We have only studied a small number of possible design patterns, manually changing the parameters. Maximising device performance can only be done iteratively with a computer algorithm. The results of this chapter could be used to guide a search algorithm. Targeting patterns with high-weighted-average slot position will restrict the search space of possible patterns. Targeting functions with strong $m_{0\pm1}$ selectivity in the sine transform will improve the yield of the device. Adjusting the grating structure, using an SMM to all orders of scattering, could allow one to further improve the mode selectivity parameters of a grating.

In the next chapter, we apply design functions similar to the exemplar ones to investigate how Fourier-based theory and analysis compare with real devices. Ch. 6 analyses how applying a HR facet affects index-patterned devices using our Fourier method.

Chapter 5

Implementation of Fourier designed gratings

5.1 Introduction

This chapter reports the experimental results of our grating designs for uncoated devices from our partners at Eblana Photonics Ltd., and matching modelled data. Sec. 5.1.1 discusses the approach taken for this experimental portion of the investigation. In Sec. 5.2.1 we will see how the experimental distributions of lasing modes change with the grating design and compare to the initial Fourier-modelled data. In Sec. 5.2.2 we will see how the general performance of the device is improved by changing the design function. Sec. 5.3.1 will examine how changes can be made to the Fourier model to physically explain the differences between the initial Fourier-modelled results and the experimental data. Sec. 5.3.2 makes a general analysis of the experimental device performance; with Sec. 5.3.2.1 analysing mode selectivity, Sec. 5.3.2.2 looks at grating loss, and Sec. 5.3.2.3 analysing the implications for the device yield of using different design functions.

We will demonstrate the ability of the first-order Fourier method to predict the spectra of experimental devices with uncoated facets. We will see evidence for our assertion that increasing the distance between the grating and the "Left facet", away from the centre of the cavity, can be used to increase single-mode selectivity [25]. Increasing single-mode selectivity will improve most of the device operational parameters; SMSR, slope efficiency, and output power. As highlighted in the previous chapter and in the literature [26, 20], the random distribution of the grating-facet phase during manufacturing reduces the yield of index-patterned devices. We will capture this effect experimentally and match it to the predictions of the Fourier model. We will explore how changing mode resonances with cavity length can select or suppress modes, and how variations in the cavity refractive index can change the wavelength position of the mode-selection patterns.

5.1.1 Design of experiment

The devices were designed for manufacture and testing at Eblana Photonics Ltd., using the functions presented in Tab. 5.1, and the cavity parameters in Tab. 5.2. The general wafer structure for the 1550 nm device is outlined in Ref. [29]. We will compare the device performance experimentally and using the Fourier method. The 275 µm cavity length was the length being implemented in this process run, meaning we had to conform to it. Approximately one hundred and eighty devices were characterised for each of the four designs. The large number of devices gives sufficient data to assess the performance of the different patterns when considering the random distribution of the grating-facet phase. The devices were tested for single-facet output power and SMSR at 100 mA, and for threshold current.

No.	Function	$\Delta\alpha_{m_0}$ (cm^{-1})	$\Delta\alpha_{nn}$ (cm^{-1})	$20\Delta\alpha$ (cm^{-1})
f_1	$f(\epsilon) = 1$	1.3	1.4	0.8
f_4	$f(\epsilon) = \epsilon \sin^2(2\pi\epsilon)$	2.9	2.3	2.3
f_5	$f(\epsilon) = \sin^2\left(\frac{3}{2}\pi\epsilon\right)$	2.9	2.2	2.2
f_6	$f(\epsilon) = \sin^2(\pi\epsilon)$	3.2	2.0	2.0

TABLE 5.1: Design functions used for experimental devices, and their Fourier-calculated mode selection metrics, modelled using parameters in Tab. 5.2 and slot patterns in Fig. 5.2.

L (µm)	275
λ_0 (nm)	1550
m_0	1652
N	20 or 16 for f_1
R_l, % power	~ 30
R_r, % power	~ 30
Slot r, % amplitude	1.2
α_f (cm^{-1})	47.3
d (µm)	~ 0.9

TABLE 5.2: Design parameters for devices in this chapter.

Fig. 5.1 shows the design functions after weighting, $h(\epsilon)$. This time four functions were selected, as this balanced the number of designs versus the number of devices we had available to implement our designs on. We wanted enough design variation to fully analyse the effect of changes in slot density along the cavity while having enough devices to get reliable statistical measurements each design. We did not use the same functions as in Ch. 4, as the results in this chapter are more so being used to verify our conclusions, where as Ch. 4 was more theoretical exploratory investigation, so we had different goals for our function comparison. $f_1(\epsilon) = 1$ was the only function that we took directly from Ch. 4 [24]. Its large $h(\epsilon)$ amplitude close to $\epsilon = 0$ results in the bunching of slots near the centre of the cavity, as in Fig. 5.2, making it an ideal experimental comparison for the effect of weighted-average slot position. It was also a function previously studied before, making it generally a good basis to compare against. $f_2(\epsilon) = |\epsilon|$ was not included, as the grating it produces is similar to a Bragg type grating with fixed slot spacing, and is a design that has been manufactured several times before [19] — f_1 is already providing a basis comparison function. $f_4(\epsilon) = \epsilon \sin^2(2\pi\epsilon)$ was chosen instead of $f_3(\epsilon) = \epsilon \sin(2\pi\epsilon)$. f_3 and f_4 have the same general parabolic shape, with both functions starting and returning to zero in the $\epsilon = 0 \rightarrow 0.5$ range, as in Fig. 4.6 a) and Fig. 5.1. Squaring the sine term reduces the span of the function peak and selection of the $m_{\pm 1}$ modes in the model, as in Fig. 4.6 c) and Fig. 5.3. This should result in a clearer increase in SMSR over the other functions.

The function $f_5(\epsilon) = \sin^2\left(\frac{3}{2}\pi\epsilon\right)$ has a similar shape to f_4, with a wider span, and does not return to zero before $\epsilon = +0.5$. This results in a wider spread of slots than f_4, as can be seen in Fig. 5.2. $f_6(\epsilon) = \sin^2(\pi\epsilon)$ is similar to f_4 and f_5, but the function is truncated at $\epsilon = 0.5$, near its maximum amplitude. f_6 has an increased weighted-average slot position compared to the other three functions, as can be seen in Fig. 5.2. This should increase the selectivity of m_0 against the mirror loss threshold of the device.

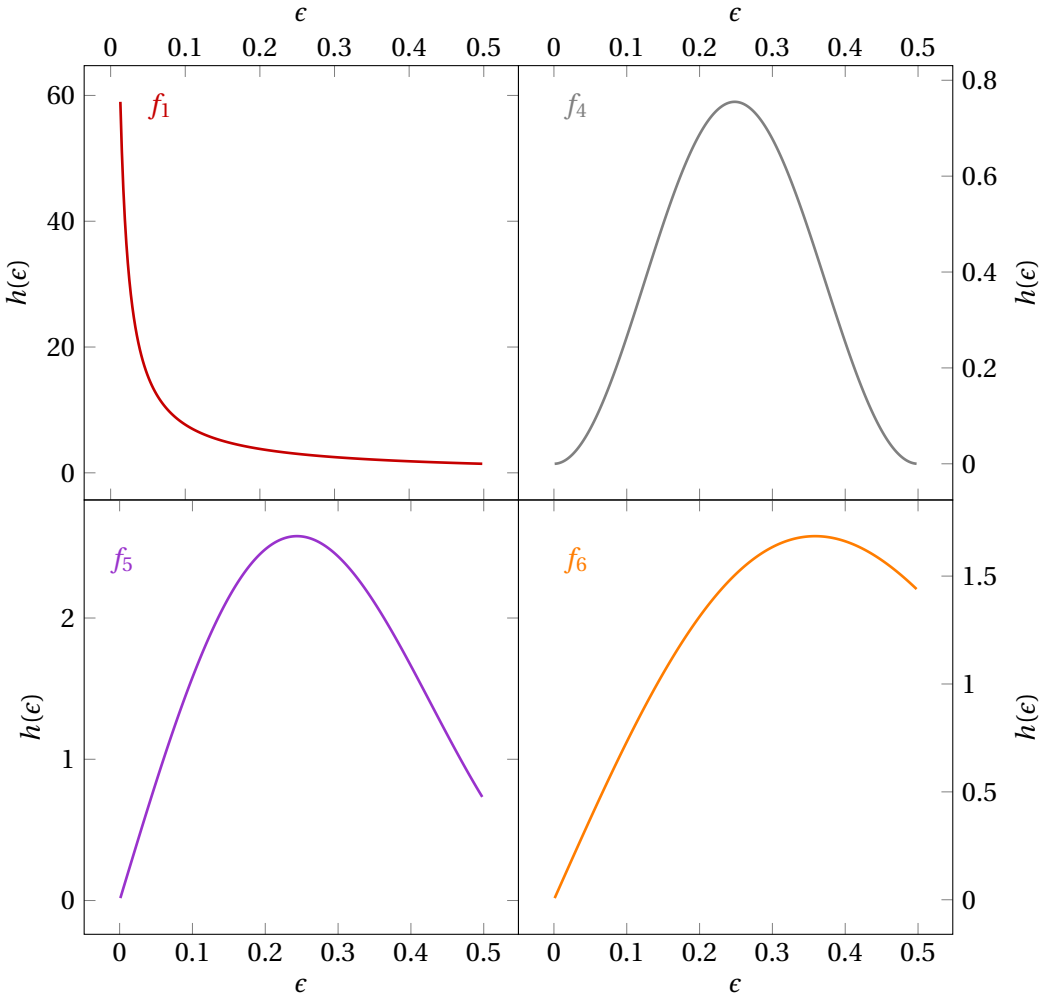


FIGURE 5.1: The weighted design function, $h(\epsilon)$, for functions in Tab. 5.1, using parameters in Tab. 5.2. f_1 for $\epsilon = 0.0125 \rightarrow 0.5$ and f_4, f_5 and f_6 for $\epsilon = 0.0 \rightarrow 0.5$.

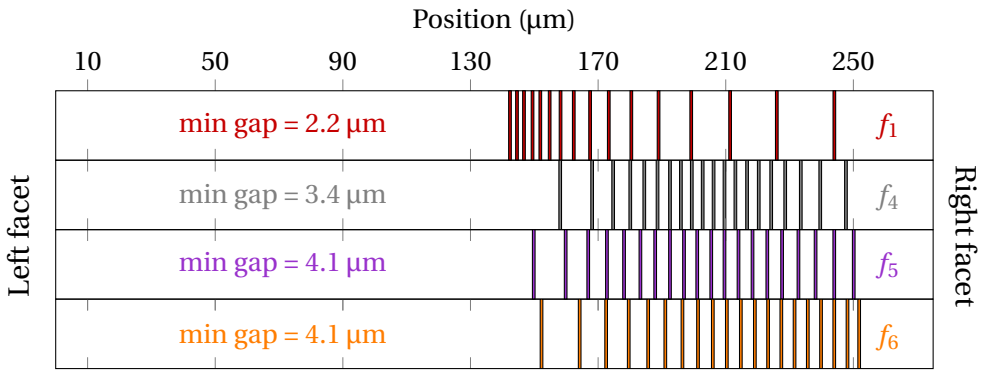


FIGURE 5.2: Slot positions for functions in Tab. 5.1, using the design parameters in Tab. 5.2; including the minimum gap between slots for each pattern. Sixteen slots for f_1 sampled in the range $\epsilon = 0.0125 \rightarrow 0.43$, and twenty slots for f_4, f_5 and f_6 sampled in the range $\epsilon = 0 \rightarrow 0.43$. Slots have not been placed within 20 μm of the "Right facet"

In order not to have slots too close to the "Right facet" that could be removed during cleaving, we only sampled the functions up to $\epsilon =\sim 0.43$. This resulted in f_4, f_5 and f_6 being more similar than desired when selecting their design functions in the full $\epsilon = 0 \rightarrow 0.5$ range. For an uncoated device, it is possible to place slots on either the left or right hand side of the device. However, given the accuracy with which slots can be placed relative to the facets no benefit is gained by placing some of the slots on one side and the remainder to the other side of the centre of the device. Even with restricting the sampling of f_1 to the range $\epsilon = 0.125 \rightarrow 0.43$, this was still a difficult design to manufacture given the intense bunching of slots near the centre of the cavity. To remedy this, we removed four slots in the range $130 \rightarrow 170$ μm. For f_1 in Fig. 5.3, we compare the reduced sixteen-slot with the complete twenty-slot mirror threshold spectrum. It has also been previously established in the literature that the position of the perturbation in the cavity is related to the magnitude of the modal selectivity [9, 25]. Removing the four slots for f_1 should have minimal impact on the device spectrum.

We can see in Fig. 5.4 a) that f_4, f_5 and f_6 should also give greater modal selectivity as the grating-facet phase changes; which should result in an increased yield over f_1. They should have tighter distributions of performance metrics for manufactured devices compared to f_1, as these functions are more likely to select modes close to m_0, Fig. 5.4 b).

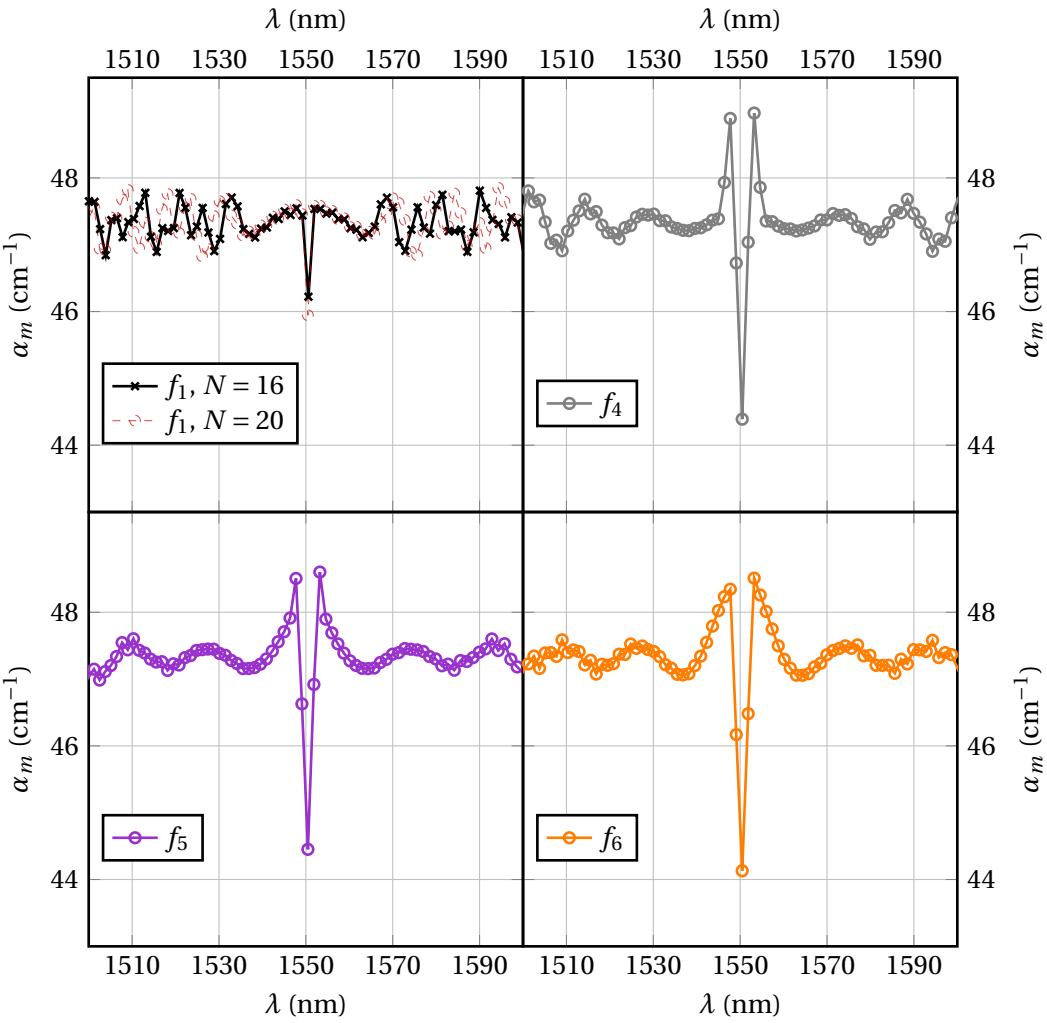


FIGURE 5.3: Fourier-calculated modal mirror loss spectra for gratings in Fig. 5.2, modelled using parameters in Tab. 5.2.

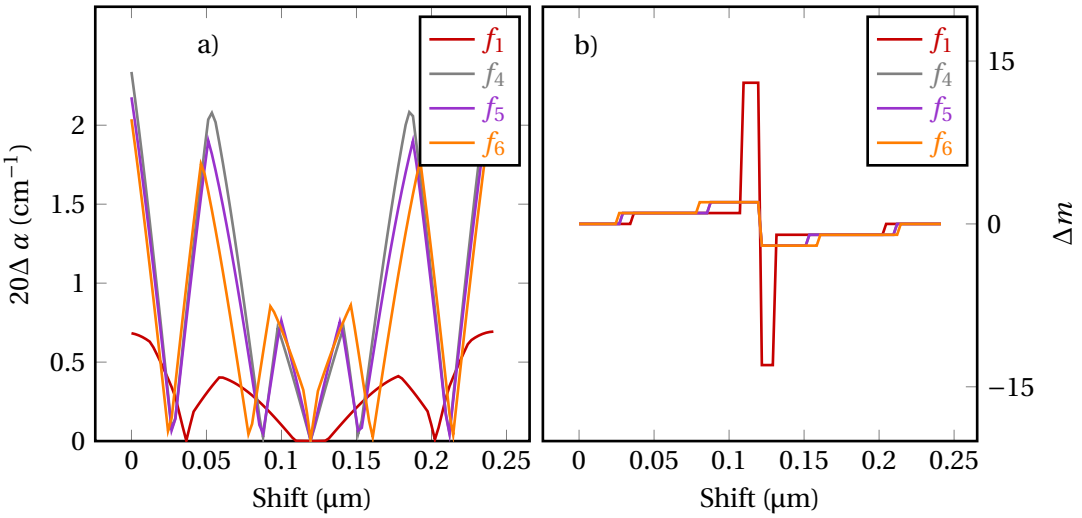


FIGURE 5.4: The impact of changing grating-facet phase on: a) mode selectivity against a twenty-mode bandwidth, b) change in mode number selected. For gratings in Fig. 5.2, modelled using parameters in Tab. 5.2.

5.2 Results

The devices in this section were manufactured and tested by Eblana Photonics Ltd., Dublin; with the data then forwarded for analysis in this thesis. The devices were tested at bar-level for output power and SMSR at 100 mA, and threshold current. In Fig. 5.3 we have plotted the spectrum for the device with the highest SMSR for each function. We can see that each function clearly selects a single mode in the spectrum.

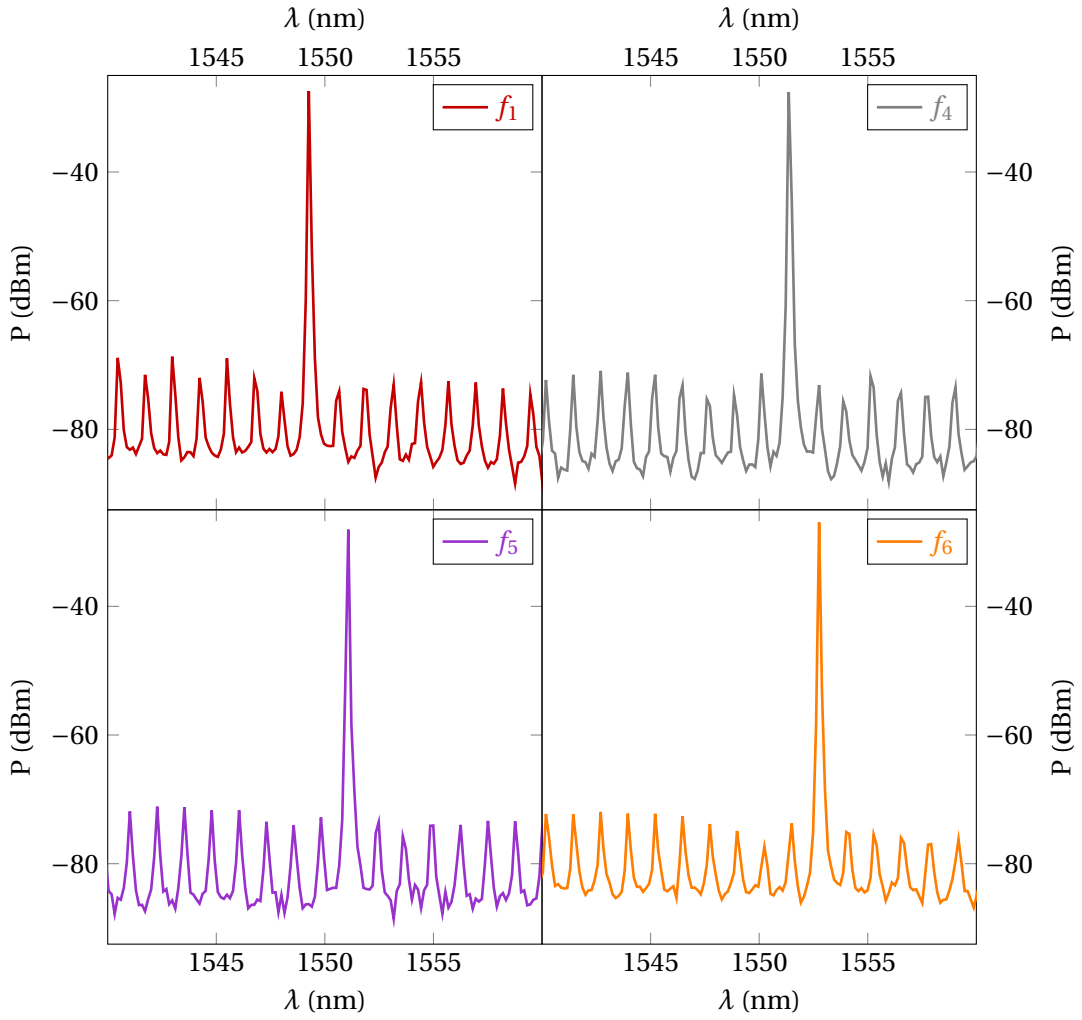


FIGURE 5.5: Experimental spectra for the device with the highest SMSR in the data for each function at 100 mA forward current, for gratings in Fig. 5.2, designed using parameters in Tab. 5.2.

5.2.1 SMSR versus wavelength distribution

To analyse the laser mode distributions statistically, we plotted the experimental and modelled SMSR versus lasing mode wavelength for each function. To model SMSR versus wavelength, we take each function grating and cycle it through a phase $\frac{\lambda_0}{2n}$ rotation using Eq. 3.23, as in Sec. 4.2.5. We calculated a modal mirror selectivity, $\alpha_{\Delta m}$, for each mode in a twenty-mode band around m_0 at each phase position. We then converted to mode number, m, to calculate the wavelength of each mode. We then applied a simple parabolic gain level adjustment [74]

$$\Delta g_m = \alpha_m - \alpha_f \left(\frac{\Delta \lambda_0}{\delta \lambda} \right)^2 \text{ cm}^{-1}, \tag{5.1}$$

assuming a gain-bandwidth centred at m_0, with a full width at half-maximum of $\delta\lambda = 70$ nm [112]. We used a parabolic band approach here as opposed to fitting an experimental gain-bandwidth, as in Sec. 4.3.4, as we did not have a gain-bandwidth trace for these devices, and the parabolic approach allows for easier fitting to the data. We calculated the selectivity of each mode, ΔG_m, baselined against the selectivity of the mode with the lowest mirror threshold, as in Eq. 4.10. To convert to SMSR, we apply [20, 64, 113]

$$SMSR_m \approx 10 \log_{10} \left(\frac{\Delta G_m}{\delta_G} + 1 \right) \text{ dB}. \tag{5.2}$$

δ_G is related to the gain necessary for the mode to overcome its cavity loss and lase

$$\delta_G = \alpha_m \beta_{sp} \eta_r \frac{I_{th}}{I - I_{th}} \text{ cm}^{-1}. \tag{5.3}$$

where β_{sp} is the spontaneous emission factor and η_r is the radiative efficiency. β_{sp} and η_r are unknown values for us, however an approximation is typically applied [20]

$$\delta_G \sim 1 \times 10^{-3} \frac{I_{th}}{I - I_{th}} \text{ cm}^{-1}. \tag{5.4}$$

The drive current is $I = 100$ mA, and I_{th} is the median value of the threshold current for each function from the experimental data in Tab. 5.3. Eq. 5.2 and Eq. 5.4 also highlight the relationship between mode selectivity, mirror loss, and SMSR, e.g., a doubling of mode selectivity will lead to a 3 dB increase in SMSR. Also, from Eq. 2.9, there is a linear inverse relationship between cavity length and mirror loss, i.e., doubling cavity length increases SMSR by 3 dB, provided mode selectivity remains constant. The fact that each mode is ratioed to the mode with the highest selectivity gives the highest selectivity mode an SMSR of 0 dB. m_0 is ~ 0.5 nm from 1550 nm, as the mode spacing is large for the 275 µm resonator, and the laser can only lase on the nearest allowed mode of the cavity. The number of phase points was chosen to match the number of experimental devices in each distribution. SMSR for a given grating position was the minimum SMSR value in a twenty-mode bandwidth around m_0.

The SMSR versus wavelength distributions of the experimental data in Fig. 5.6 show the devices lasing around specific wavelengths. The pattern of these wavelengths closely resembles what is predicted by the Fourier model in Fig. 5.4. Strongly selected modes in the Fourier calculation, as in Fig. 5.3, correlate with high SMSR lasing modes in the experimental data, usually $m_{0\pm1}$. This selected mode changes as the grating-facet phase changes, which is why multiple lasing wavelengths appear in the experimental devices. We can see that f_1 has three prominent modelled lasing modes, where the other devices have five. This is a result of the number of modes that the Fourier transform of each design function selects as it changes phase.

The experimental devices tend to have a range of wavelengths around a set mode to lase on. Devices lase on modes allowed by the grating; however, variation in the cavity refractive index between devices means that the wavelengths of the allowed modes vary. We can see for f_6 in Fig. 5.6, that the modes are in less structured patterns. This could be the result of damage to these devices. For the function f_1 there are lasing modes < 1545 nm. As the selectivity of m_0 for f_1 is low, it has a low net selectivity against modes across the gain-bandwidth. This makes the modes outside of $m_{0\pm2}$ more likely to lase compared to the other three functions. The low SMSR points for the selected modes in the distributions ($\sim m_{0\pm2}$) in Fig. 5.6 are due to the modal competition with the variation of the grating-facet phase. We can also see the similarity of the f_4, f_5 and f_6 distributions, which could be the result of compressing the gratings for manufacture, i.e., the gratings had to be fitted to $\epsilon = 0 \rightarrow 0.43$ instead of $\epsilon = 0 \rightarrow 0.5$—as they had been designed using the Fourier model.

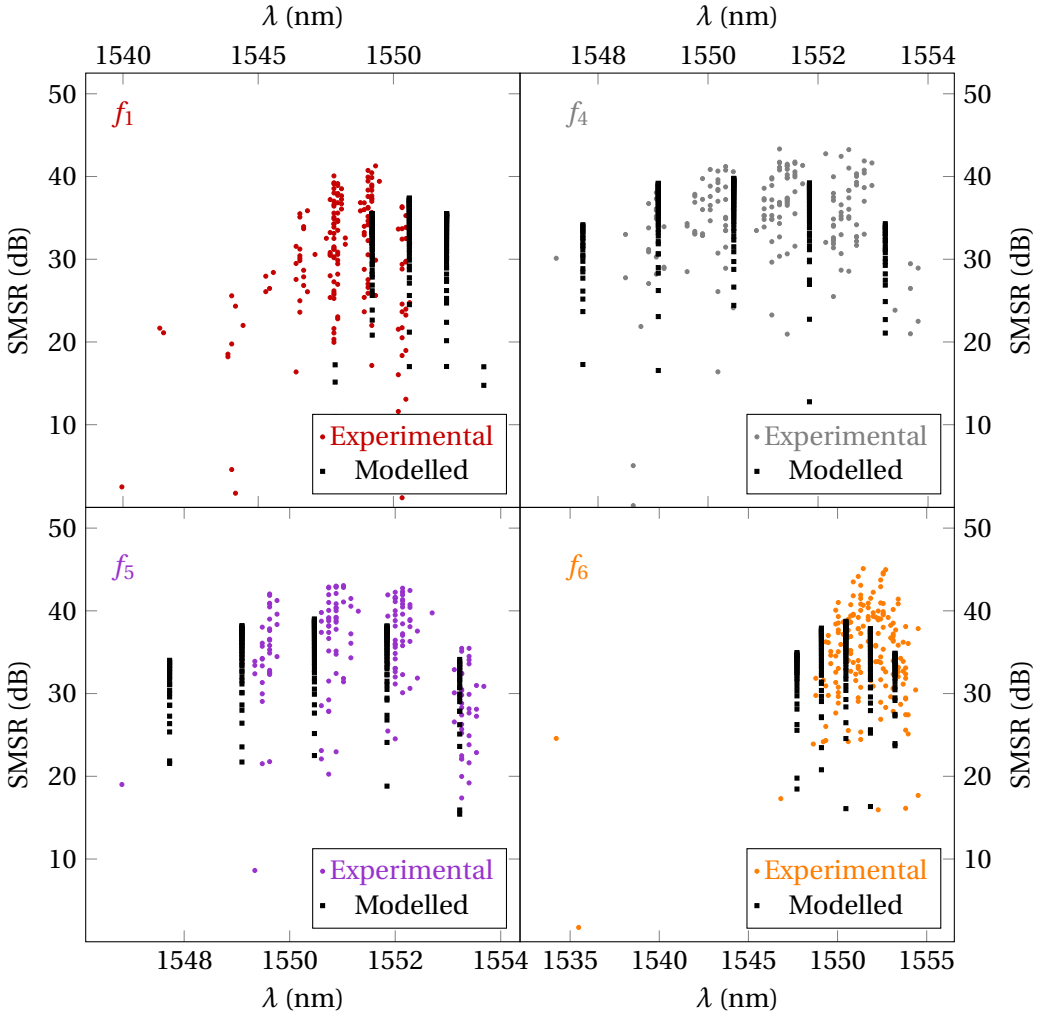


FIGURE 5.6: SMSR versus wavelength distributions for experimental and modelled data. For gratings in Fig. 5.2, designed and modelled using parameters in Tab. 5.2.

The Fourier model underestimates the SMSR of these devices. One reason for this, as we will analyse further in Sec. 6.3.2, may be that SMSR is sensitive to the depth of the etch of the slot, which is difficult to tightly control. We can also attribute some of the discrepancy to the approximate nature of Eq. 5.4 and Eq. 5.2. Another is that we do not include inter-slot scattering in the modelled data and are likely to be underestimating the slot reflectivity [84]. Also, we take a median value for the threshold current in the SMSR calculation, not allowing for the fact that current thresholds will be reduced when the slots are aligned with the facets of the cavity. This will be a small effect given the logarithmic factor in the current threshold to the SMSR relationship. The biggest discrepancies between the modelled and experimental data are that there appears to be one extra or one less mode comparing the modelled and experimental results for each function and an offset in the mode positions between the experimental and modelled data, as will be discussed further Sec. 5.3.1.

5.2.2 General performance parameters

Fig. 5.7 shows the box plots of SMSR and single-facet output power at 100 mA, and the threshold current for the four different design functions with uncoated facets. SMSR is generally measured by coupling the laser light to an optical spectrum analyser and comparing the power in the modes of the spectrum. Power is measured by coupling the light from each mode into a photodetector at a set drive current for the laser diode and measuring the photocurrent generated. Threshold current is calculated by ramping up the drive current to the laser diode and measuring the corresponding photocurrent captured. From this trace, the point at which stimulated emission dominates over spontaneous emission can be extracted [114]. We do not know the details of the set-up used by Eblana Photonics Ltd., but it would have followed these general principles.

SMSR for f_1 is lower, and SMSR is relatively constant between f_4, f_5, and f_6. The output power is higher for f_4, but is relatively constant between f_1, f_5, and f_6. We can also see in Fig. 5.7 c) that f_4 has a lower threshold current than the other three functions. There is a large distribution of values for each parameter for each function. For SMSR, the f_1 distribution is larger than for the other functions. For power, the distribution of power is over a smaller range for f_4. For the threshold current, f_6 has the largest distribution. In Tab. 5.3 we compared the median values for each of the performance parameters for each function. In the third column of Tab. 5.3, we have combined the median single-facet output power, P, and the threshold current, I_{th}, to calculate the slope efficiency, η, using the equation

$$\eta = \frac{2P}{I - I_{th}}. \tag{5.5}$$

We double the single-facet output power to estimate the total power output of the device. The Fabry-Pérot devices do not have the additional loss from the grating slots, therefore their threshold current is lower and output power and slope efficiency is higher.

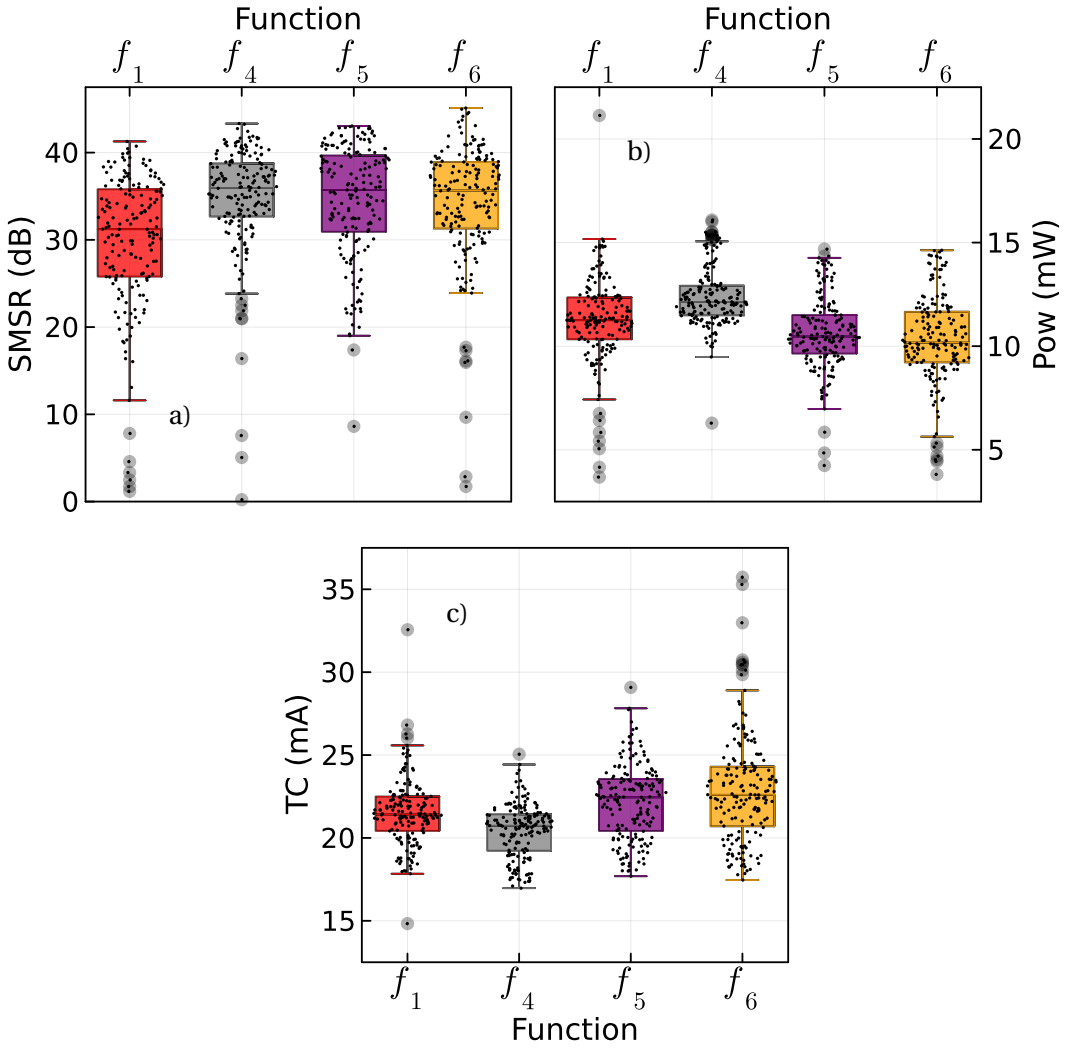


FIGURE 5.7: Box plots: a) SMSR and b) single-facet optical power at 100 mA, and c) threshold current. For gratings in Fig. 5.2, designed using parameters in Tab. 5.2. Large black dots are data points outside inter-quartile range.

Function	P at 100 mA (mW)	I_{th} (mA)	η (W/A)	SMSR (dB)
f_1	11.3 ± 2.2	21.4 ± 2.0	0.29 ± 0.06	31.2 ± 7.9
f_4	12.1 ± 1.7	20.7 ± 1.6	0.31 ± 0.05	35.9 ± 6.3
f_5	10.5 ± 1.9	22.5 ± 2.3	0.27 ± 0.06	35.7 ± 6.5
f_6	10.2 ± 2.2	22.6 ± 3.3	0.26 ± 0.07	35.7 ± 6.8
Fabry-Pérot	23.1 ± 2.7	14.2 ± 1.9	0.54 ± 0.1	

TABLE 5.3: Comparison of experimental performance metrics, for gratings in Fig. 5.2, and unetched Fabry-Pérot cavities on the bars. Designed using parameters in Tab. 5.2.

5.3 Analysis

We divide the analysis into two parts. The first looks at the changes that can be made to the Fourier calculation to improve the fit between the experimental and modelled data in Fig. 5.6. The second makes a more general analysis of the device performance after the merit of the Fourier calculation has been established.

The most notable difference between the modelled and experimental results in Fig. 5.6 is that some modes appear to be suppressed or added when comparing the two data sets. We identify the main reason for this as the change in mode wavelength as the laser cavity changes length with facet cleaving. We will model this effect and make a mathematical analysis of the process. We will also see how changing the cavity refractive index in the Fourier model can explain the offset in wavelength between the modelled and experimental device modes.

5.3.1 Fourier model fitting

5.3.1.1 Modal excitation and suppression from cavity resonances

As a laser cavity length varies with cleaving, the phase change for the cavity modes at the device facets causes a change in the mode wavelengths supported by the cavity. The slot spacing in the gratings is designed for a specific wavelength, and this spacing does not change with cleaving. There can then be a mismatch between the modes supported by the cavity and those supported by the grating.

Here we will use the Fourier method to model this effect and overlay it on the experimental data. Take for example, an additional $\frac{\lambda_0}{4n}$ error to the end of the cavity

$$L_{err} = L + \frac{\lambda_0}{4n}. \tag{5.6}$$

We calculate a fractional error, F_{err}, of this new erroneous cavity length, L_{err}, to the ideal cavity length

$$F_{err} = \frac{L_{err}}{L}. \tag{5.7}$$

We then apply this fractional error to the chosen wavelength

$$\lambda_{err} = \lambda_0 F_{err}. \tag{5.8}$$

Device design calculations are made for the erroneous wavelength, λ_{err}, and cavity length, L_{err}, before the erroneous slot positions, ϵ_{err}, are then re-aligned to the ideal λ_0 mode

$$\epsilon_{pos} = \frac{\epsilon_{err}}{F_{err}}, \tag{5.9}$$

to make the modal mirror loss calculation, using Eq. 3.23. This simulates the effect of having an actual cavity length error, rather than simply moving the device gratings relative to the facets, as we had done in Sec. 4.2.5. A demonstration of this calculation can be seen in Fig. 5.8; with errors $\frac{\lambda_0}{8n}$, $\frac{\lambda_0}{4n}$, $\frac{3\lambda_0}{8n}$ added to the cavity length of the f_1 grating device in Fig. 5.2. The grating-facet phase change calculation is re-performed for each separate cavity length. We chose a ±5 modal range, as modes outside this range are not likely to lase with the roll-off in spectral gain. We can see how f_1 goes from selecting mostly three modes in the ideal case to selecting four modes when the cavity is not perfectly half-wave resonant. The mode hopping around the 0.17 µm grating shift position is as a result of the deviation from the ideal grating, i.e., third-order Bragg reflection slots and the compressed grating.

In Fig. 5.9 we overlay the experimental data with the modelled cavity length change for f_1 data, using the SMSR conversion in Sec. 5.2.1. In Fig. 5.6 we see that there are four prominent lasing modes, where only three are predicted by the model when the cavity is the correct number of half-wavelengths. We can then see in Fig. 5.9 how a fourth mode is selected as the cavity moves away from the ideal resonance. We can see that the $\frac{\lambda_0}{8n}$ modal distribution is most similar to the experimental data.

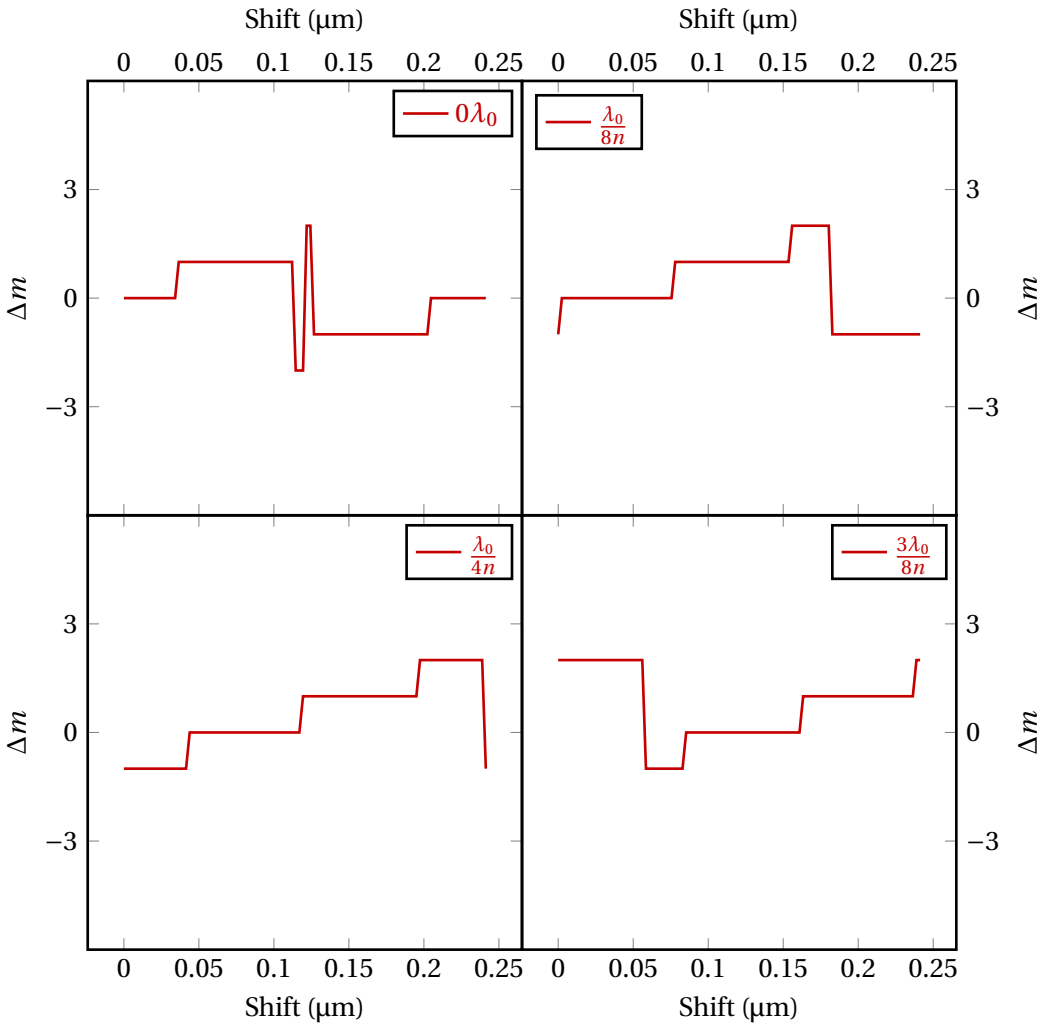


FIGURE 5.8: Modelled change in mode selection with facet position and cavity length error for the $f_1(\epsilon)$=1 grating in Fig. 5.2, modelled using parameters in Tab. 5.2.

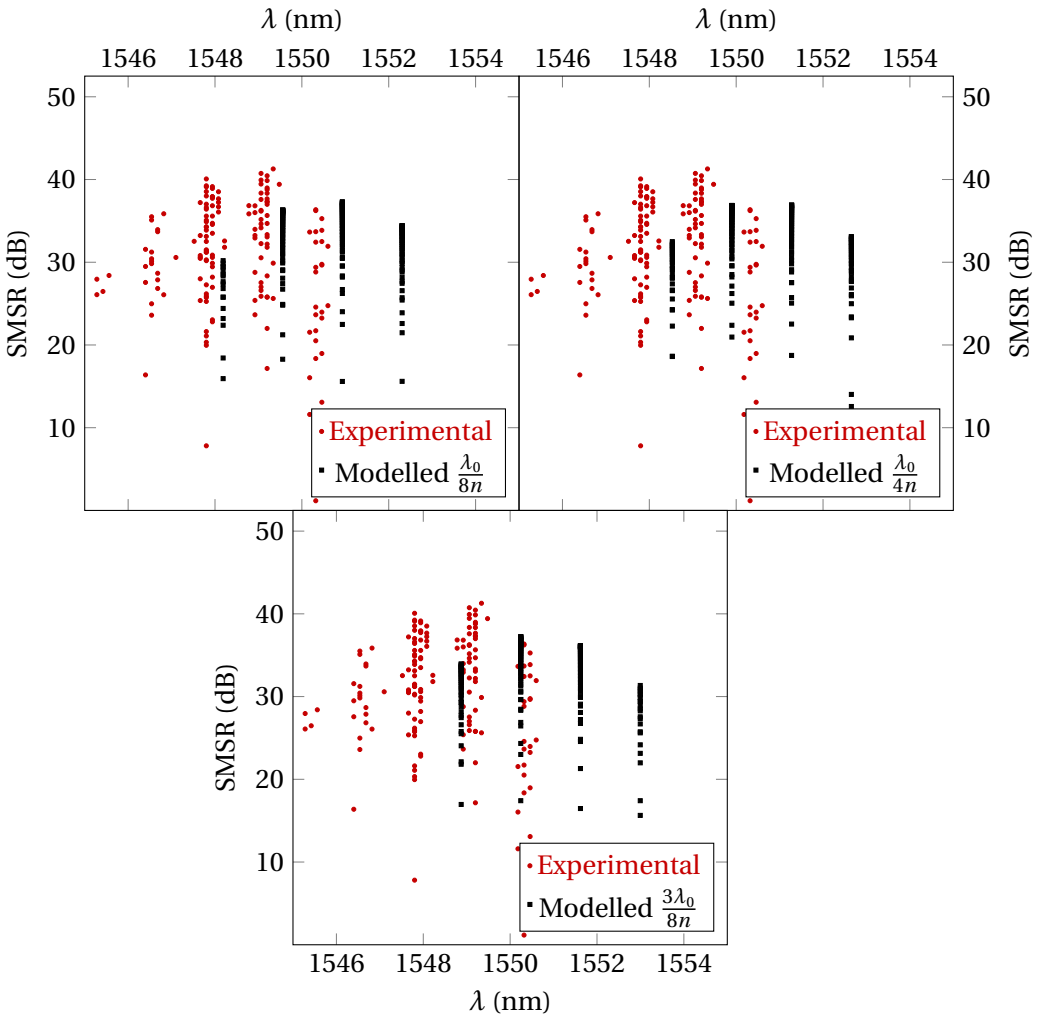


FIGURE 5.9: SMSR versus wavelength for f_1 grating in Fig. 5.2 as cavity resonance changes with sub-wavelength changes in cavity length. Using the parameters in Tab. 5.2.

We will now look at the suppression of a mode in the distribution due to this effect. In Fig. 5.10 we have calculated how the selected mode changed with the grating-facet phase for f_5, in the ±5 mode range for $\frac{\lambda_0}{8n}$, $\frac{\lambda_0}{4n}$ and $\frac{3\lambda_0}{8n}$ cavity length errors. We can see how five modes being selected in the ideal case can be reduced to four. For f_5 in Fig. 5.6, we see that a mode is predicted near 1548 nm in the modelled data, but is not present in the experimental results. This is not due to a lack of spectral gain, as f_1 in Fig. 5.6 has a significant number of lasing devices around 1548 nm. In Fig. 5.11 we can see how the fifth mode is reduced in the distribution as the cavity resonances change. For the $\frac{\lambda_0}{8n}$ and $\frac{\lambda_0}{4n}$ cavity errors, this is for highest mode number, which should result in the lowest wavelength mode being suppressed. This is consistent with what is observed in Fig. 5.11, although we note that a small decrease in refractive index can also move the pattern to longer wavelengths.

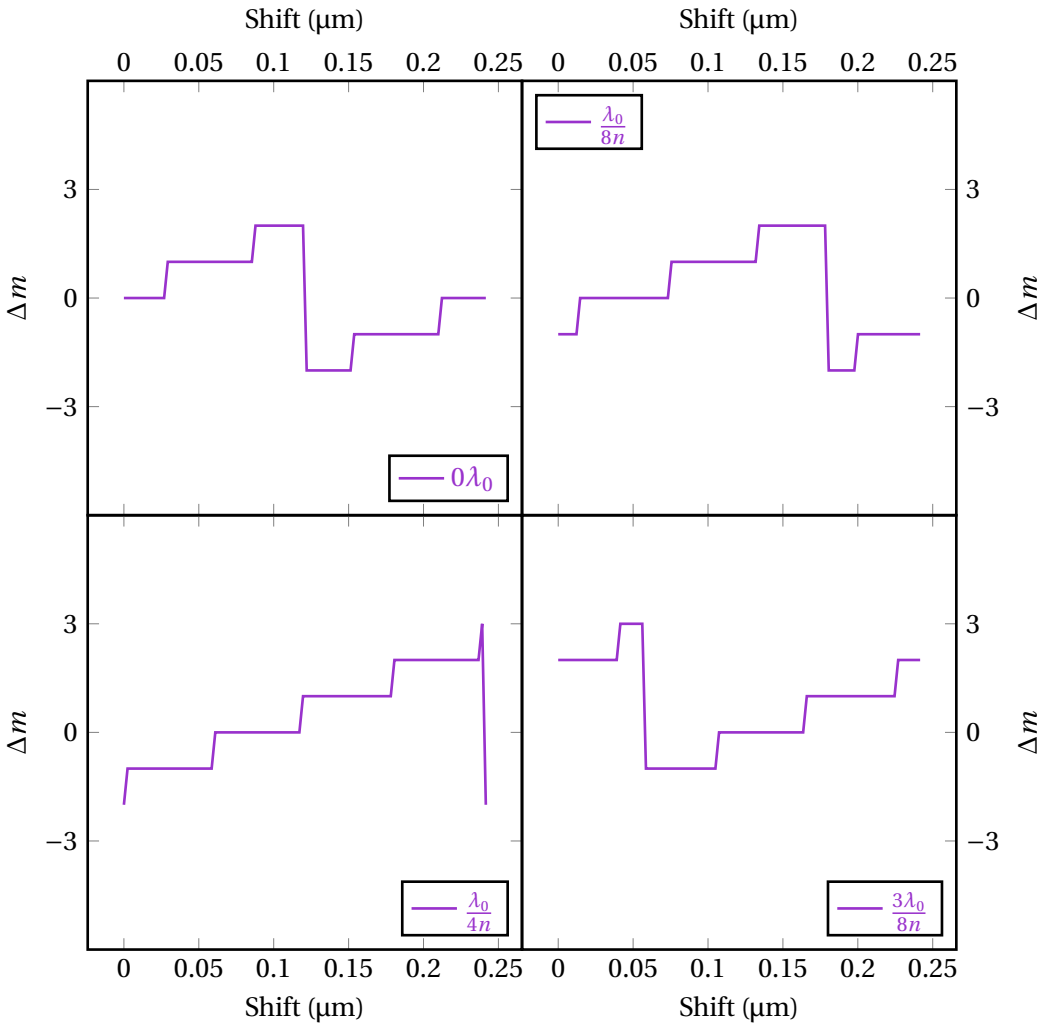


FIGURE 5.10: Modelled change in mode selection with facet position and cavity length error for the $f_5(\epsilon) = \sin^2\left(\frac{3}{2}\pi\epsilon\right)$ grating in Fig. 5.2, using the parameters in Tab. 5.2.

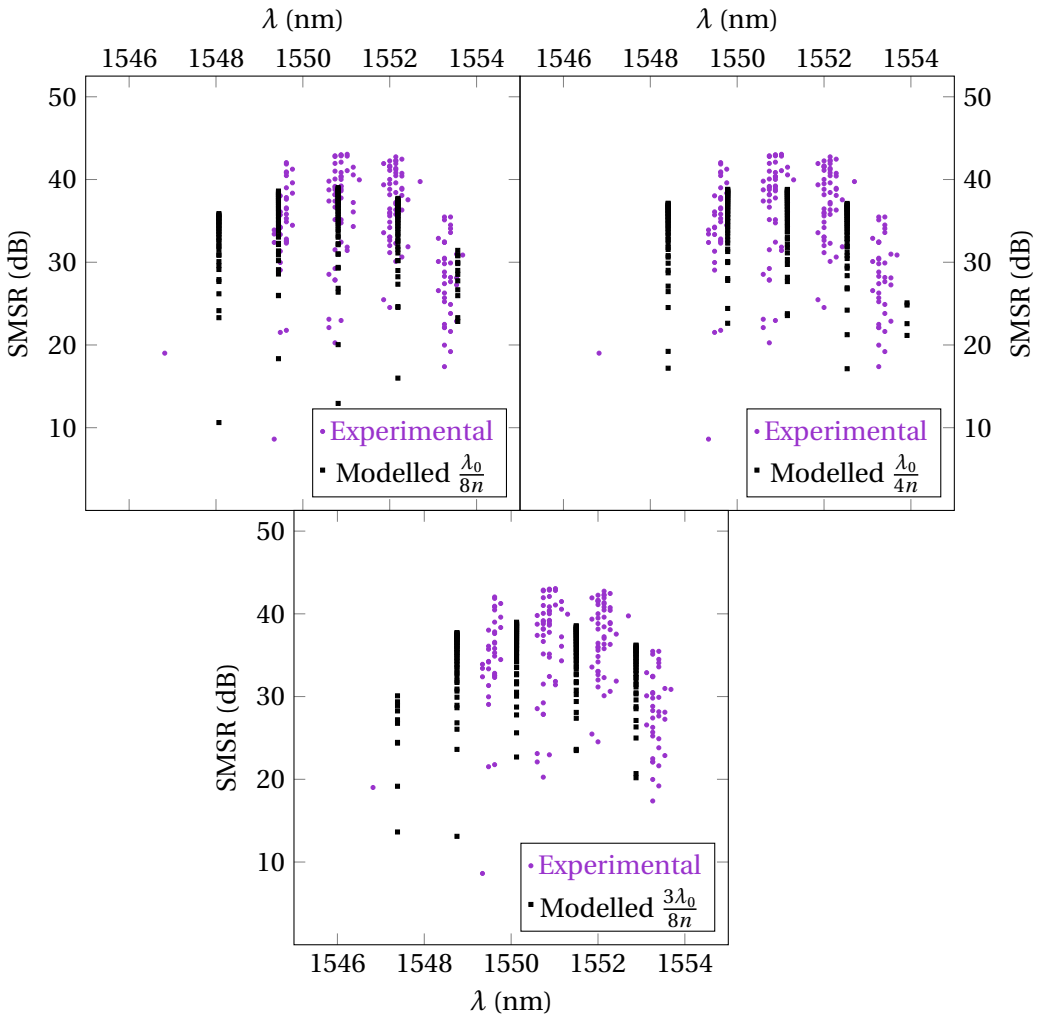


FIGURE 5.11: SMSR versus wavelength for f_5, for modelled cavity length and resonance changes. For grating in Fig. 5.2, using the parameters in Tab. 5.2.

When designing an index-patterned laser, a fixed cavity length and refractive index is assumed, and the laser is designed to operate on mode m_0 of the cavity, where

$$m_0 = \frac{2Ln}{\lambda_0}, \tag{5.10}$$

for a laser without perturbations. The wavelength is then adjusted to take into account the change in the cavity effective refractive index after grating introduction. To date, all analysis of index-patterned lasers has assumed that when the laser facets are formed, the cavity is of a specific length where the ratio $\frac{2Ln}{\lambda_0}$ is an integer, m. However, the likelihood that this is the case is minimal. We therefore now extend the previous Fourier analysis to take account of the situation where the design as implemented selects a non-integer real number

$$M = \frac{2Ln}{\lambda_0}, \tag{5.11}$$

as the target mode number. We can expand $\sin(2\pi m\epsilon) = \sin(2\pi m_0\epsilon + 2\pi\Delta m\epsilon)$ as in Sec. 3.2.4

$$\sin(2\pi m_0\epsilon + 2\pi\Delta m\epsilon) = \sin(2\pi m_0\epsilon)\cos(2\pi\Delta m\epsilon) + \cos(2\pi m_0\epsilon)\sin(2\pi\Delta m\epsilon). \tag{5.12}$$

When the slots are all placed so that the "Left facet" is a whole number of half-wavelengths from the left face of each slot, then $\cos(2\pi m_0\epsilon) = 0$; the second term disappears on the right-hand side of Eq. 5.12 and we find that the mode selectivity is given by the weighted Fourier transform ($\cos(2\pi\Delta m\epsilon)$) of the slot positions. Consider now the case where all slots are positioned so that for wavelength $\lambda = \frac{2Ln}{M}$, the left face of each slot has the same phase with respect to the "Left facet" of the laser. It is then advantageous to rewrite m as

$$m = M + (m - M). \tag{5.13}$$

In this case we expand $\sin(2\pi m\epsilon) = \sin(2\pi M\epsilon + 2\pi(m-M)\epsilon)$ as

$$\sin(2\pi M\epsilon + 2\pi(m-M)\epsilon) =$$
$$\sin(2\pi M\epsilon)\cos(2\pi(m-M)\epsilon) + \cos(2\pi M\epsilon)\sin(2\pi(m-M)\epsilon). \tag{5.14}$$

When all slots are placed so that their left face is a whole number of half-wavelengths, $\lambda = \frac{2Ln}{\lambda}$, from the "Left facet" of the cavity, then $\cos(2\pi M\epsilon) = 0$. The second term disappears on the right-hand side of Eq. 5.14, and we find that the selectivity of the mode is given by the weighted Fourier transform $\left(\cos(2\pi(m-M)\epsilon\right)$ of the slot positions. Inserting the changes between Eq. 5.14 and Eq. 5.12 into Eq. 5.13, and replacing $\cos(m_0\pi)\cos(\Delta m\pi)$ by $\cos(m\pi)$ then gives the expression of how the change in mirror loss, $\Delta\alpha_{m-M}$, depends on the difference between the mode number m and the design value, M

$$\Delta\alpha_{\Delta m-M} = \frac{2\Delta n}{Ln}\cos(m\pi)\times \sum_{j=1}^{N}\sinh(\alpha_f\epsilon_j L)[\sin(2\pi M\epsilon)\cos(2\pi(m-M)\epsilon)+\cos(2\pi M\epsilon)\sin(2\pi(m-M)\epsilon)]. \quad (5.15)$$

If we take the example of the distribution function $f(\epsilon) = 1$, for which the ideal change in mirror loss for mode m is proportional to the sinc function, $f(k) = \frac{\sin(\pi(m-m_0))}{\pi(m-m_0)}$, where m_0 is an integer (and where in implementation we note that, in addition, every second term changes sign). In the case of real M, we now have the change in the threshold gain proportional to the values of the sinc function at points displaced from the values $p\pi$, where p is an integer to the points $(p+\zeta)\pi$, where $0<\zeta<1$, as can be seen in Fig. 5.12.

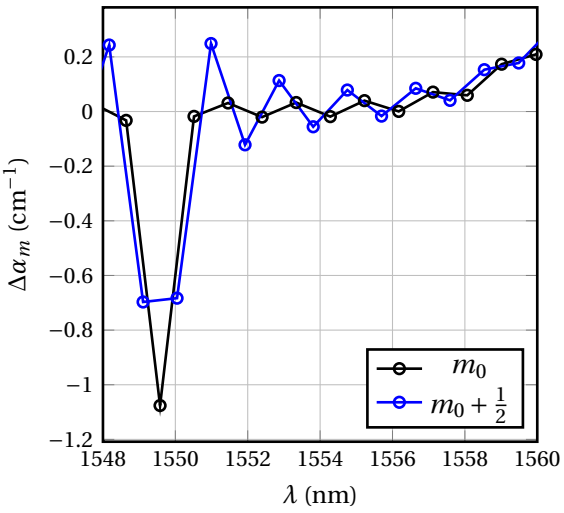


FIGURE 5.12: $f(\epsilon)$=1 mirror loss modulation spectrum when the cavity is m_0 resonant (Black points); and the cavity is $m_0+\frac{1}{2}$ resonant (blue points). For an ideal $\left(d=\frac{\lambda_0}{4(n-\Delta n)}\right)$ twenty slot grating, modelled using the parameters in Tab. 4.2.

5.3.1.2 Variation in cavity refractive index

We can see in Fig. 5.6 and Sec. 5.3.1.1 that the modal pattern can be largely predicted by the Fourier model but not necessarily the wavelength position of the modes. The wavelength of a mode is based on its effective refractive index in the cavity of the device. In Fig. 5.13 we can see that a change in the refractive index of −0.108% or $\Delta n = -3.4 \times 10^{-3}$ can shift the mode pattern by one whole mode spacing to longer wavelengths. We note that experimental devices are subject to varying cavity refractive index as a result of variation in the current density in the cavity and changing temperature during operation. A refractive index change of 0.108% is well within the limits of what is possible in terms of varying carrier concentration [115]; and temperature, with $\frac{dn}{dT} \sim 2 \times 10^{-4} \mathrm{K}^{-1}$ for indium phosphide devices [116, 117]. Both of these factors can explain the offset in the mode positions in the experimental data in Fig. 5.6. Note that changing cavity resonances can also affect the wavelength position of the modes, but to a smaller extent. Changing the temperature of the cavity will also change the gain-bandwidth peak position and cavity length, which we do not consider here. We are only modelling changing cavity refractive index. This does occur with temperature tuning.

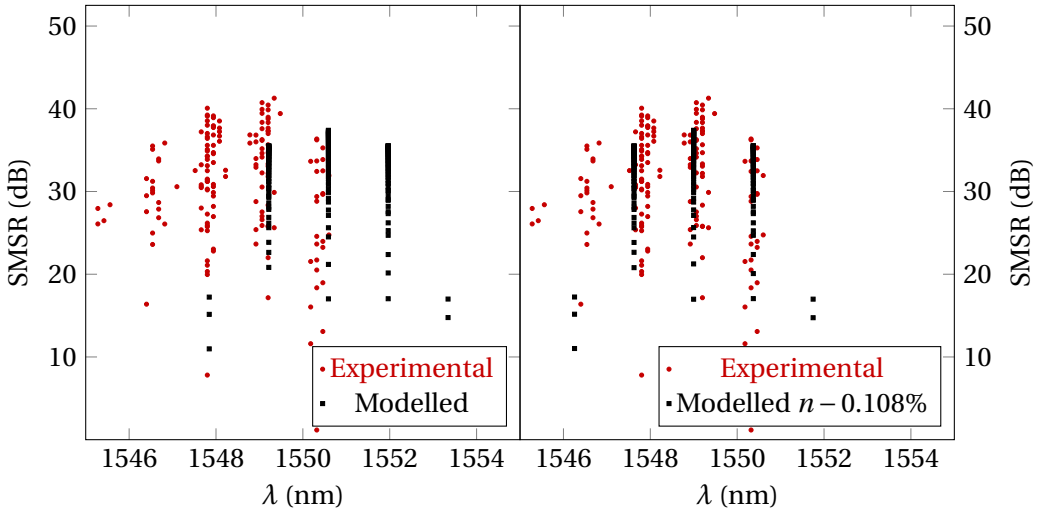


FIGURE 5.13: SMSR versus wavelength fitting for f_1 with a −0.108% refractive index change. For grating in Fig. 5.2, using the parameters Tab. 5.2.

5.3.2 General performance analysis

5.3.2.1 Mode selectivity

In Tab. 5.3 we can see the median SMSR for each of the design functions. Note that f_4, f_5 and f_6 have similar median SMSR values and the f_1 value is lower. This is in agreement with the assumption from the Fourier model that slots near the cavity centre have minimal impact on mode selection. Although the f_1 device has four less slots, this was modelled not to have a significant impact on m_0 selectivity; as the slots that were removed were close to the centre of the cavity. Although this is a circular argument, we can see from Sec. 5.2.1 and Sec. 5.3.1 that there is good agreement between the selectivity calculated by the first-order Fourier method and the SMSR of the experimental devices with uncoated facets. We have also seen in Sec. 4.2.4 that the Fourier model agrees well with the separate SMM calculation, and in Ref. [25] the importance of slot position in the cavity on modal selection is also established.

5.3.2.2 Loss

We see from the median results in the first and second columns of Tab. 5.3 that f_4 has 1.9 mW or ~ 20% more optical power than f_6 at a forward current of 100 mA, and a 1.9 mA or ~ 10% lower threshold current. To calculate the grating loss, α_g, we use [118, 9]

$$\alpha_g = \frac{hf\eta_i\alpha_f}{\eta q} - \alpha_f - \alpha_p, \tag{5.16}$$

where h is Plank's constant, f is the lasing-mode frequency, q is the elementary charge, and η_i is the current injection efficiency and is assumed to be one. α_p was calculated for these devices by adding unetched Fabry-Pérot structures to the bars, and calculating the propagation loss for these cavities using Eq. 5.17 and setting α_g equal to zero

$$\alpha_p = \frac{hf\eta_i\alpha_f}{\eta q} - \alpha_f. \tag{5.17}$$

α_f was taken to be 47.3 cm^{-1}. The unetched Fabry-Pérot device had a median single-facet output power of 23.1 ± 2.7 mW and a median threshold current of 14.2 ± 1.9 mA. We then calculated a slope efficiency of 0.54 ± 0.1 W/A and a waveguide background propagation loss of 23.0 cm^{-1}, using Eq. 5.17. In columns two and five of Tab. 5.4, we show the calculated loss of each grating and the total propagation loss of the cavity. In the third column, we ratio the loss to the number of slots in each grating. In the fourth column, we include the median slot gap for each grating.

Function	α_g (cm^{-1})	Loss per slot (cm^{-1})	Median slot gap (μm)	α_p
f_1	61.3	3.8	5.1	84.3
f_4	53.7	2.7	3.9	76.7
f_5	69.4	3.5	4.6	92.4
f_6	73.3	3.7	4.4	96.3
Fabry-Pérot				23.0

TABLE 5.4: Comparison of calculated grating losses (Eq. 5.17), loss per slot, and median slot gap. For gratings in Fig. 5.2, designed using the parameters in Tab. 5.2.

The function f_4 experiences the lowest loss per slot. We can see in Tab. 5.4 that the grating loss between f_5 and f_4 has been reduced by 15.7 cm^{-1}. This shows the range of modulation of loss that is possible by changing the slot pattern. We did not use f_6 for this comparison, as these devices are potentially damaged, but note that their median performance values are similar to f_5.

We see a general trend of increasing grating loss with an increasing median gap between slots. A similar result was obtained theoretically in Ref. [9]. Here, devices with different grating order, i.e., the gap between the slots, are modelled using a 2D SMM and experimentally compared. A 2D SMM includes the vertical scattering of light out of the slots, which should be the most significant path of optical loss out of the grating.

5.3.2.3 Grating-facet phase and yield

The lasing-mode distributions are in broad agreement with our assertion that the span of possible mode threshold spectra for a given design function and grating-facet phase can be calculated by taking a linear combination of the sine and cosine transforms of our design function for a full phase-cycle. This demonstrates the out-of-phase capabilities of the Fourier method and the ability to design functions resistant to facet position errors. As an example of the improvement in experimental device yield; in Tab. 5.5, we see that if we take a baseline specification for SMSR of 35 dB, f_1 would have a yield of 29.8%, while f_4 would have a yield of 56.1%.

Function	% > 35 dB
f_1	29.8
f_4	56.1
f_5	54.2
f_6	53.3

TABLE 5.5: Experimental yield comparison for uncoated facet devices. For gratings in Fig. 5.2, designed using the parameters in Tab. 5.2. The wavelength selected is not necessarily λ_0.

5.4 Discussion

We used the first-order Fourier method to design device grating patterns. The devices were manufactured and tested by Eblana Photonics Ltd.. The experimental results are in general in agreement with the predictions of the first-order Fourier method. We see evidence to support our assumption that gratings with a weighted-average slot position further from the "Left facet" and not near the centre of the cavity select the lasing mode more strongly; and the cosine and sine transforms of the grating pattern can be used to calculate the lasing threshold for any facet position along the cavity. The experimental results also provide us with further insight into the operation of index-patterned devices, i.e., changing resonances with cavity length can suppress or select lasing modes.

Although the function f_4 was modelled then chosen to have the best SMSR metrics, the fact that the gratings had to be fitted to $\epsilon = 0 \rightarrow 0.43$ instead of $\epsilon = 0 \rightarrow 0.5$, converged the Fourier transforms and therefore the spectra for f_4, f_5 and f_6, resulting in no significant SMSR difference between these three functions. We did see a performance boost in terms of excess grating loss, and this parameter is modulatable with grating design. Grating loss appears to be more sensitive to the design of the grating than SMSR, and it is possible to increase both simultaneously [9, 119]. Reducing the optical loss experienced by a device cavity may increase the operating lifetime of the device, as it will require less drive current to meet a set output power. Reducing loss will also reduce the linewidth of the device [120].

This chapter analyses how effectively the Fourier design method [24, 26, 86] translates into real device performance for devices with uncoated facets and serves as a stand-alone experimental analysis of the effects of changing perturbation distributions on device behaviour. We have seen devices with an SMSR median below 40 dB (Fig. 5.7 a)). To consistently deliver devices with SMSRs > 40 dB, a HR coating is applied, which typically improves each of the cavity selection factors; $\Delta\alpha_{m_0}$, $20\Delta\alpha$, and α_f. In the next chapter, we will explore both theoretically and experimentally the implications of applying a HR coating to each of these design functions.

Chapter 6

High-reflectivity facet index-patterned devices

6.1 Introduction

This chapter will analyse the effect of applying a high-reflectivity (HR) coating to the "Left facet" of an index-patterned laser. In Sec. 3.2.3 we discussed the weighting of the grating design function to account for the change in the amplitude of the E-field along the cavity — this chapter looks at the effect a HR coating has on an index-patterned laser, largely from the point of view of the cavity weighting effect. Three sets of experimental data are reported, using the same four experimental design functions as in the previous chapter. One set of $L = 275$ µm devices with uncoated facets. One set with the same $L = 275$ µm devices after a HR coating is applied — these device gratings do not have the optimal weighting for the change in E-field amplitude along the cavity. There is then a separate set of devices with longer cavities, $L = 350$ µm, with gratings ideally weighted for a HR coating. Comparing the three data sets will give us insight into the operation of index-patterned lasers in the HR regime.

In Sec. 6.1.1 we will theoretically analyse how the design function weighting and modal mirror loss spectra change when the "Left facet" of an index-patterned device is HR coated. Sec. 6.1.2 will mathematically analyse how HR coating affects m_0 mode selectivity against cavity threshold, $\Delta\alpha_{m_0}$. Sec. 6.1.3 will detail the experimental approach used in this chapter. Sec. 6.2.1 will compare the modelled and experimental SMSR versus wavelength distributions for the three data sets. In Sec. 6.2.2 we will compare the general performance of the different device designs. Sec. 6.3.1 analyses loss from the cavity gratings. Sec. 6.3.3 will analyse how m_0 selectivity changed experimentally with HR coating. Sec. 6.3.2 will look at the effect of the slot reflectivity on SMSR. Finally, Sec. 6.3.4 will analyse yield changes with HR coating.

A HR coating is typically applied to one side of an edge-emitting laser to ensure that the majority of the optical power is emitted from the opposite facet, increasing power coupling from the device. In index-patterned devices, it has the additional benefit of improving SMSR by increasing mode selectivity, Sec. 6.1.1, and reducing the mirror loss of the cavity. The specific effects of applying a HR coating to an index-patterned laser have not been analysed before, particularly using our first-order Fourier method. In the Fourier approach, a change in cavity facet reflectivity changes the weighting of the design function and the selectivity of the modes in the spectrum. Applying a cavity-specific weighting is an important step in the design process to ensure that the desired Fourier transform of the design function is recreated in the mirror threshold spectrum of the laser. Although this step is important for the development of high-performance devices, we will see that, for most devices, not having the ideal weighting can still result in SMSR > 40 dB.

6.1.1 Change in weighting and design function after HR coating

For unequal facet reflectivities we can revert to using the full design function weighting expression

$$w(\epsilon) = \frac{1}{2}\left\{\sqrt{\frac{r_l}{r_r}}\exp(\alpha\epsilon L) - \sqrt{\frac{r_r}{r_l}}\exp(-\alpha\epsilon L)\right\}, \tag{6.1}$$

rather than the reduced version $w(\epsilon) = \sinh(\alpha\epsilon L)$, when $r_l = r_r$. $w(\epsilon)$ is the change in the mode selectivity that a slot has at position ϵ in the cavity. $w(\epsilon)^{-1}$ is how much a grating design function must be weighted at a point ϵ to maintain the integrity of its Fourier transform. In Figs. 6.1 a) and b) we can see how $w(\epsilon)$ and $w(\epsilon)^{-1}$ change, respectively, between when a device is uncoated (UC, $R_l \sim 30\%$, $R_r \sim 30\%$) and when a HR coating is applied to the "Left facet" ($R_l \sim 95\%$, $R_r \sim 30\%$).

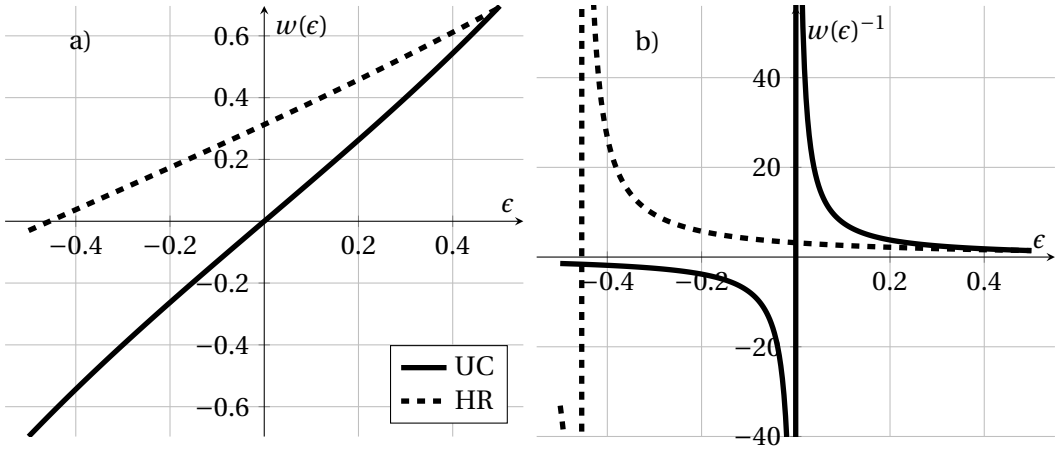


FIGURE 6.1: a) $w(\epsilon)$ weighting function, and b) its inverse $w(\epsilon)^{-1}$ in the range ϵ=−0.5→0.5 for the 275 µm device parameters in Tab. 6.3. For UC: $R_l = 30\%$,$R_r = 30\%$, and HR: $R_l = 95\%$,$R_r = 30\%$.

In Fig. 6.1 a), we see that the shape of $w(\epsilon)$ remains largely unchanged after HR coating. However, we see that the function has shifted upward, moving the zero of $w(\epsilon)$ near $\epsilon = -0.5$. This means that there is no longer a region of low slot impact near to where the slots are placed in the cavity. We can see how, for a slot at $\epsilon = 0$, $w(\epsilon)$ increases from 0 to ~ 0.3. We can also see that $w(\epsilon)$ remains the same at ~ 0.65 for a slot at $\epsilon = 0.5$. Slots near the cavity centre increase in selectivity, but slots near the facet do not with HR coating.

In Fig. 6.1 b), we can see how the weighting $w(\epsilon)^{-1}$ changes after HR coating. The region of diverging weighting has moved to beside the "Left facet", away from the slots. The profile of region $\epsilon = 0 \rightarrow 0.15$ in Fig. 6.1 b) changes significantly from a decreasing $\frac{1}{\epsilon}$ shape for uncoated facets to a gentle negative slope in the HR regime. Functions with most of their slots in this region will be distorted in terms of their spectra after the HR coating. The region $\epsilon = 0.15 \rightarrow 0.5$ remains relatively unchanged in terms of amplitude and shape for $w^{-1}(\epsilon)$ after coating. Functions with most of their slots in this region will have largely unchanged spectra after facet coating.

In Fig. 6.2 we can see how the design weighting function, $h(\epsilon)$, changes after HR coating for our experimental designs. The biggest change is for f_1, which is expected due to the change in the weighting function close to $\epsilon = 0$. f_1 now consists of an approximately linear gentle negative slope, as opposed to a $\frac{1}{\epsilon}$ steep decay prior to coating. For f_5 and f_6 we can see that the peak in $h(\epsilon)$ has moved closer to the "Right facet". For f_4, the general parabolic shape of the function remains similar. We can see the reduction in the maximum of $h(\epsilon)$ for each function going from uncoated to coated, which will result in a larger spacing between the slots in the gratings. We can see in general that applying a HR coating tends to move slots closer to the right facet in this design approach.

In the HR regime, the penalty for having slots near the centre in terms of m_0 selectivity is significantly less, which means that there is a much larger space of functions to search to maximise SMSR. The minimum offset for the grating positions for $f_1(\epsilon) = 1$ is also no longer required, since $w^{-1}(\epsilon)$ no longer goes to infinity at $\epsilon = 0$.

No.	Function
f_1	$f(\epsilon) = 1$
f_4	$f(\epsilon) = \epsilon \sin^2(2\pi\epsilon)$
f_5	$f(\epsilon) = \sin^2\left(\frac{3}{2}\pi\epsilon\right)$
f_6	$f(\epsilon) = \sin^2(\pi\epsilon)$

TABLE 6.1: Design functions used in this chapter.

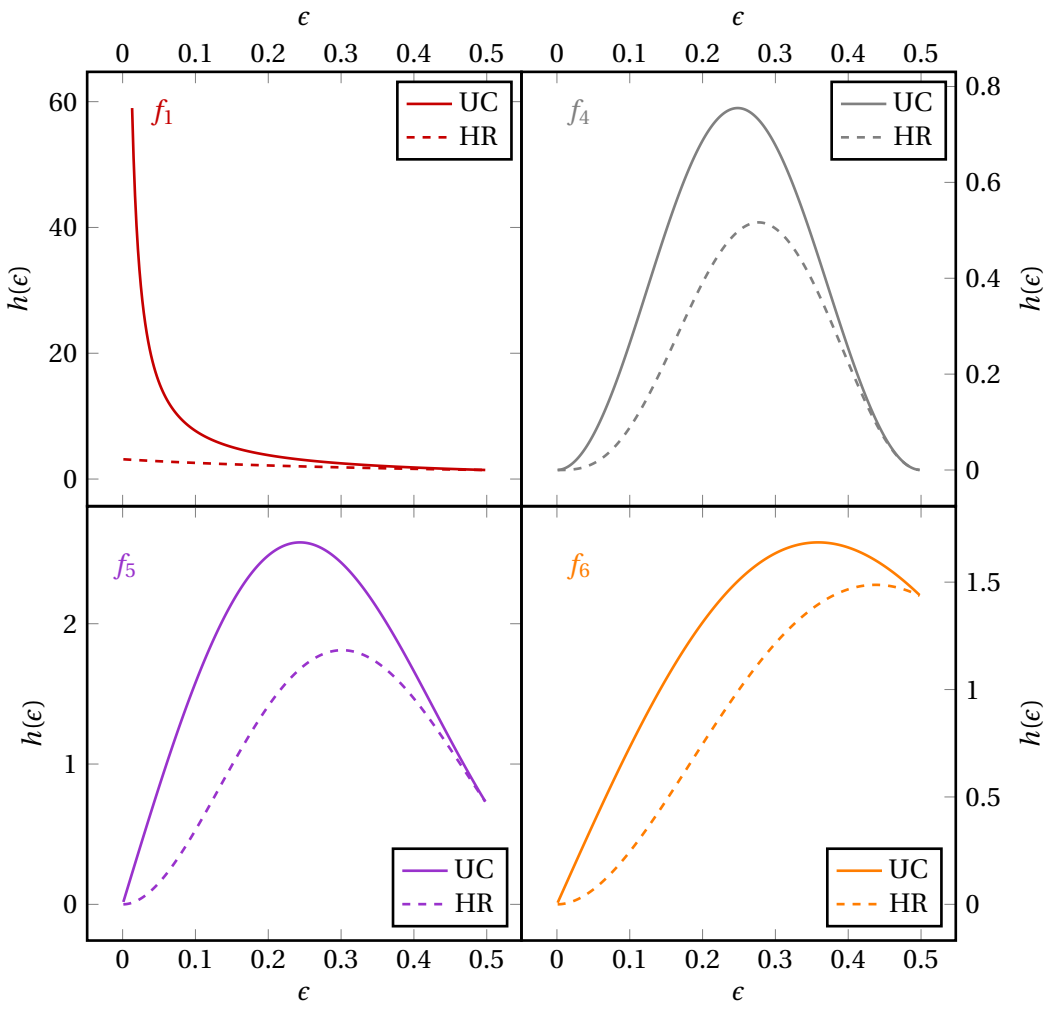


FIGURE 6.2: Change in weighted design function, $h(\epsilon)$, for functions in Tab. 6.1, modelled using the 275 µm parameters in Tab. 6.3. Solid lines show $h(\epsilon)$ with a 30% power reflectance on both facets. The dashed lines show $h(\epsilon)$ after a 95% power reflectance coating the "Left facet". f_1 for $\epsilon = 0.0125 \rightarrow 0.5$ uncoated and the remaining functions and coatings in the range $\epsilon = 0.0 \rightarrow 0.5$.

6.1.2 Chosen mode selectivity after HR coating

If we assume $f_U(\epsilon)$ as the real-space Fourier transform for a given uncoated laser, then the slot distribution is designed to approximate the weighted function, $h(\epsilon) = \frac{f_U(\epsilon)}{w_U(\epsilon)}$; where $w_U(\epsilon) = \sinh(\alpha_U \epsilon L)$ is the cavity weighting function, and α_U is the mirror loss per unit length for the uncoated device.

When one facet is coated, we still have the same weighted design function, $h(\epsilon)$, but now $h(\epsilon) = \frac{f_H(\epsilon)}{w_H(\epsilon)}$, where $f_H(\epsilon)$ is the real-space Fourier transform for the coated laser, and $w_H(\epsilon)$ is the weighting function for the coated device. We therefore have $f_H(\epsilon) = \frac{f_U(\epsilon)}{w_U(\epsilon)} w_H(\epsilon)$. We can then calculate $\Delta\alpha_{m_0}$ when a HR coating is applied to an uncoated device which was originally designed to have $f_U(\epsilon)$ as its real-space Fourier transform by modifying our previous Eq. 4.5

$$\Delta\alpha_{m_0} = \frac{N\Delta n}{Ln} \frac{\int_0^{1/2} h(\epsilon) \left\{ \sqrt{\frac{r_l}{r_r}} \exp(\alpha_H \epsilon L) - \sqrt{\frac{r_r}{r_l}} \exp(-\alpha_H \epsilon L) \right\} d\epsilon}{\int_0^{1/2} h(\epsilon)\, d\epsilon}, \tag{6.2}$$

where the factor two is omitted since the term in parentheses reduces to $2\sinh(\alpha_U \epsilon L)$ when $r_l = r_r$, and α_H is the mirror loss per unit length of the coated device. We can use Eq. 6.2 to estimate $\Delta\alpha_{m_0}$ for any input design function, with any facet reflectivity. In Tab. 6.2 we compare our analysis with Eq. 4.1 where we explicitly take into account the position of the slots. We make the calculations for the 275 µm gratings in Fig. 6.3 using the HR parameters in Tab 6.3. We can see a good convergence between the values.

Function	$\Delta\alpha_{m_0}$ Eq. 6.2 (cm^{-1})	$\Delta\alpha_{m_0}$ Eq. 4.1 (cm^{-1})
f_1	2.9	3.0
f_4	4.5	4.5
f_5	4.5	4.4
f_6	4.6	4.6

TABLE 6.2: Comparison of mode selectivity of the Fourier calculation, Eq. 4.1, and integral approximation, Eq. 6.2. For functions in Tab. 6.1, modelled using 275 µm HR parameters in Tab. 6.3. f_1 for $\epsilon = 0.0125 \rightarrow 0.43$ and f_4, f_5 and f_5 for $\epsilon = 0.0 \rightarrow 0.43$.

6.1.3 Design of experiment

In this chapter, we conduct two experiments. First, where the 275 µm UC devices were tested, then a HR coating was applied to the "Left facet", R_l =~ 30% → 95%, and the devices re-tested. Second, where the grating is correctly weighted for a HR coating. The device design parameters for each set of devices are compared in Tab. 6.3. We can see how cavity mirror loss approximately halves with HR coating. Fig. 6.3 shows a comparison of the grating designs between the two different lengths of the cavity. The gratings are only sampled up to $\epsilon \sim 0.43$ to avoid having slots too close to the "Right facet" (~ 20 µm) — to potentially be removed during facet cleaving. The slot spacing for the 275 µm devices is smaller compared to the 350 µm devices. For f_1 this was mainly due to the change in the design function after weighting due to the change in facet reflectivities, and for the remaining functions, the change in the cavity length of the devices.

Device set	275 µm UC	275 µm HR	350 µm HR
L (µm)	275	275	350
λ_0 (nm)	1550	1550	1650
m_0	1129	1129	1343
N	20 or 16 for f_1	20 or 16 for f_1	20
R_l,% power	~ 30	95	97
R_r, % power	~ 30	~ 30	~ 30
Slot r, % amplitude	1.2	1.2	1.2
α_f (cm^{-1})	47.3	24.6	19.1
d (µm)	~ 0.9	~ 0.9	~ 0.9

TABLE 6.3: Design parameters for the three sets of devices modelled and experimentally compared in this chapter.

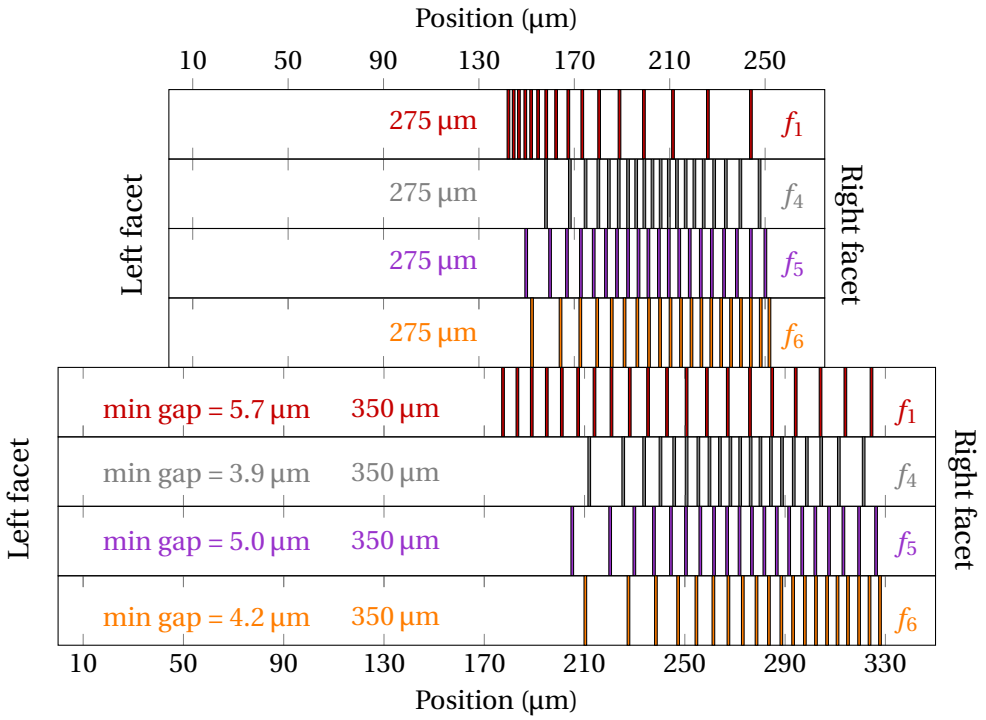


FIGURE 6.3: Slot positions for functions in Tab. 6.1, for the three different data sets; 275 μm (UC and HR), and 350 μm HR. Slots have not been placed within 20 μm of the "Right facet". Designed using parameters in Tab. 6.3. Minimum gap between slots included, with the 275 μm values being the same as in Fig. 5.2

The shape of the modelled modal mirror loss function does not change significantly between having uncoated and coated facets, and different cavity lengths for f_4, f_5 and f_6. These gratings are short and most of their slots are near $\epsilon = 0.75$. We have seen in Sec. 6.1.1 that weighting in this region of the cavity does not change significantly after HR coating. We can see that f_1 changes noticeably. This is a result of f_1 producing a longer grating for the 350 μm HR cavity, and the function places slots at positions that change significantly in terms of weighting after coating.

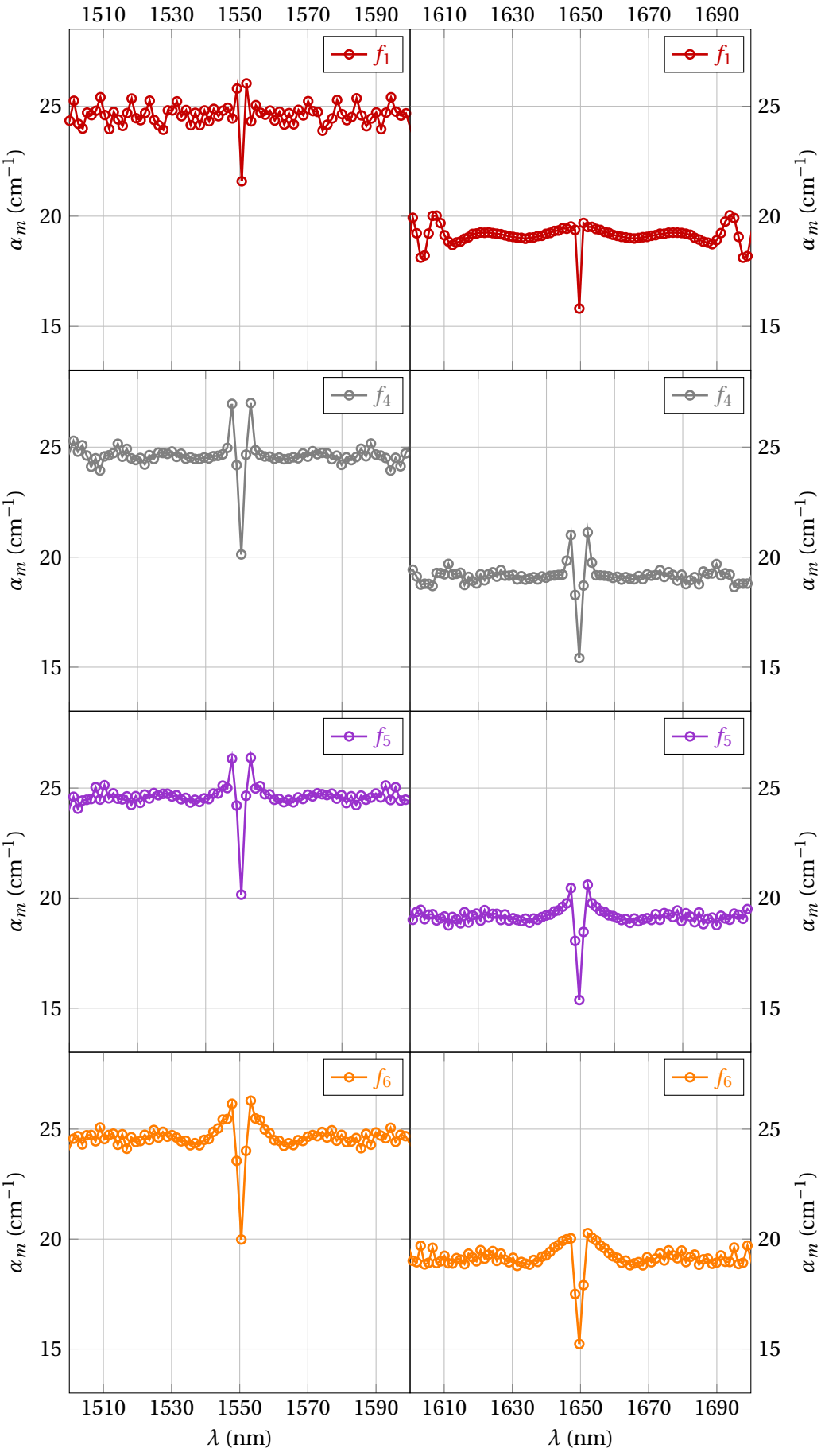


FIGURE 6.4: Fourier calculated mirror loss threshold, for gratings in Fig. 6.3 and HR parameters in Tab. 6.3. 275 µm HR devices in the left column and the 350 µm HR devices on the right.

Tab. 6.4 shows the relevant Fourier-calculated mode selection metrics for the 275 µm HR and the 350 µm HR devices. These values can also be compared with the metrics of the 275 µm UC devices in Tab. 5.1. It can be seen in Tab. 6.4 that many of the best Fourier-calculated mode selection parameters are for shorter cavity lengths. This is a result of the $\frac{1}{L}$ dependence of the mode selectivity in Eq. 4.1. The change in m_0 selectivity scales with cavity length, i.e., $\Delta\alpha_{m_0} \times \frac{275\ \mu m}{350\ \mu m}$. For example f_4 is $4.5\ cm^{-1} \times 0.8 = 3.6\ cm^{-1}$ and for f_6 $4.6\ cm^{-1} \times 0.8 = 3.7\ cm^{-1}$, going from 275 → 350 µm. The values are not exact, as we must account for the fact that the slots are not optimally placed in the two cavities due to incorrect weighting and reduction in grating length. The $L = 275$ µm devices will also have a higher mirror loss, limiting their SMSR improvement in a real device.

Comparing the 275 µm UC devices in Tab. 5.1 with the 275 µm HR devices in Tab. 6.4, we can see that the mode selection metrics improve with HR facet application separately from the reduction in cavity mirror loss, despite the weighting not being optimised to generate the desired Fourier threshold spectrum. This is expected considering our analysis in Sec. 6.1.1.

	275 µm HR			350 µm HR		
No.	$\Delta\alpha_{m_0}$ (cm^{-1})	$\Delta\alpha_{nn}$ (cm^{-1})	$20\Delta\alpha$ (cm^{-1})	$\Delta\alpha_{m_0}$ (cm^{-1})	$\Delta\alpha_{nn}$ (cm^{-1})	$20\Delta\alpha$ (cm^{-1})
f_1	3.0	4.2	2.3	3.3	3.6	3.2
f_4	4.5	4.1	4.1	3.7	2.9	2.9
f_5	4.4	4.1	4.1	3.8	2.7	2.7
f_6	4.6	3.6	3.6	3.9	2.3	2.3

TABLE 6.4: Fourier calculated selectivity performance for gratings in Fig. 6.3 and parameters in Tab. 6.3. Unshaded cells on the left are for the 95% HR 275 µm devices. Shaded cells on the right are for the 97% HR 350 µm devices.

In Fig. 6.5 a) and b), and Fig. 5.4, we can see that there is a significant improvement in the modelled yield characteristics with the application of a HR coating. Increasing the maximum 20 $\Delta\alpha$ selectivity means that more devices are likely to meet the minimum selectivity required to reach an SMSR of 40 dB as the grating-facet phase changes. There is also the added benefit of reducing the cavity mirror loss α_f, increasing the $\frac{\Delta\alpha_{m_0}}{\alpha_f}$ and the $\frac{20\ \Delta\alpha}{\alpha_f}$ factors. Comparing the 275 µm HR devices in Fig. 6.5 a) and b), and the 350 µm HR devices in Fig. 6.5 c) and d), we can see that most of the improved performance is again with shorter cavity length devices. The $\frac{1}{L}$ mode selectivity dependence also means a shorter cavity is more likely to produce a greater cavity threshold selectivity as the grating-facet phase changes. The Fourier method tends to have high selectivity over a fixed number of modes, proportional to the number of slots, this then tends to give mode high selectivity over a wider wavelength range in a shorter cavity.

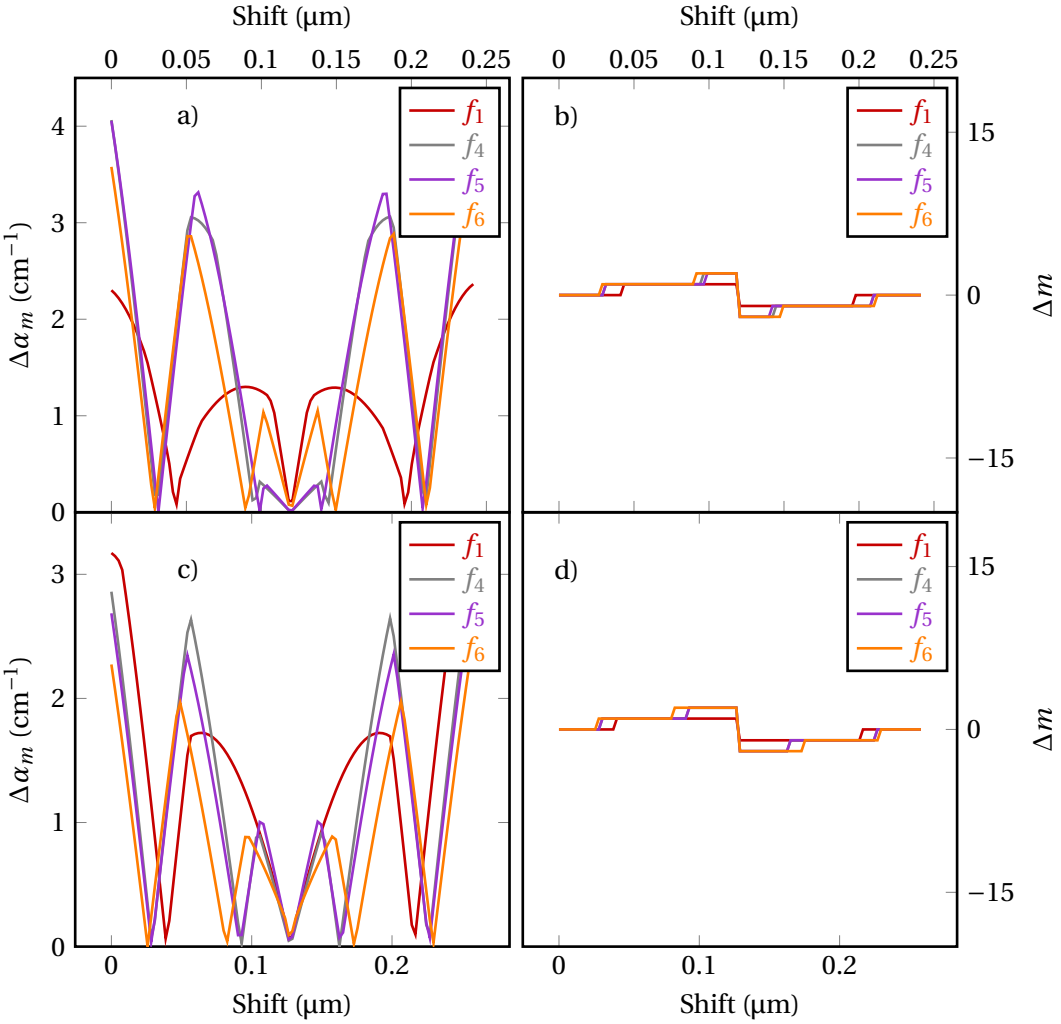


FIGURE 6.5: Fourier modelled mode selectivity and change in mode number selected with changing grating-facet phase for gratings in Fig. 6.3 and HR parameters in Tab. 6.3. Calculations are made over a twenty-mode bandwidth. a) and b) is for the 275 μm HR devices and c) and d) are for the 350 μm HR devices.

6.2 Results

The devices in this section were manufactured and tested by Eblana Photonics Ltd., Dublin — with the results forwarded for analysis in this thesis. The devices were tested at bar-level for SMSR, single-facet output power, and threshold current. The 275 µm devices were tested at 100 mA, which means that after HR coating, the devices are operating further above the threshold current. The 350 µm devices were tested at 50 mA ($\sim 3 \times I_{th}$, Tab. 6.7) forward current. The 275 µm devices in this chapter are from the same process run but a different wafer as the 275 µm devices in Ch. 5. Approximately one hundred and sixty devices for each 275 µm pattern and approximately one hundred for each 350 µm pattern are presented.

6.2.1 SMSR versus wavelength distribution

This section looks at the overlaid experimental and modelled SMSR versus wavelength distributions. The first part analyses how distributions change before and after a HR coating is applied. The second part will look at the HR-weighted grating patterns.

6.2.1.1 275 µm **UC → HR**

In Fig. 6.6 we can see a general increase in SMSR for each function after coating. The patterns of modes do not change significantly after coating but they do shift to longer wavelengths. As the "Left facet" power reflectance has changed significantly from 30% → 95% we can say that the spectral properties of index-patterned lasers are largely insensitive to changes in the "Left facet" reflectance. We can still see modes being added and removed from the distributions with changing cavity resonances after HR coating, as in Sec. 5.3.1.1. The SMSR for the uncoated f_4 devices was ~ 4 dB less than the Ch. 5 devices, indicating a processing variation between the wafers in this run.

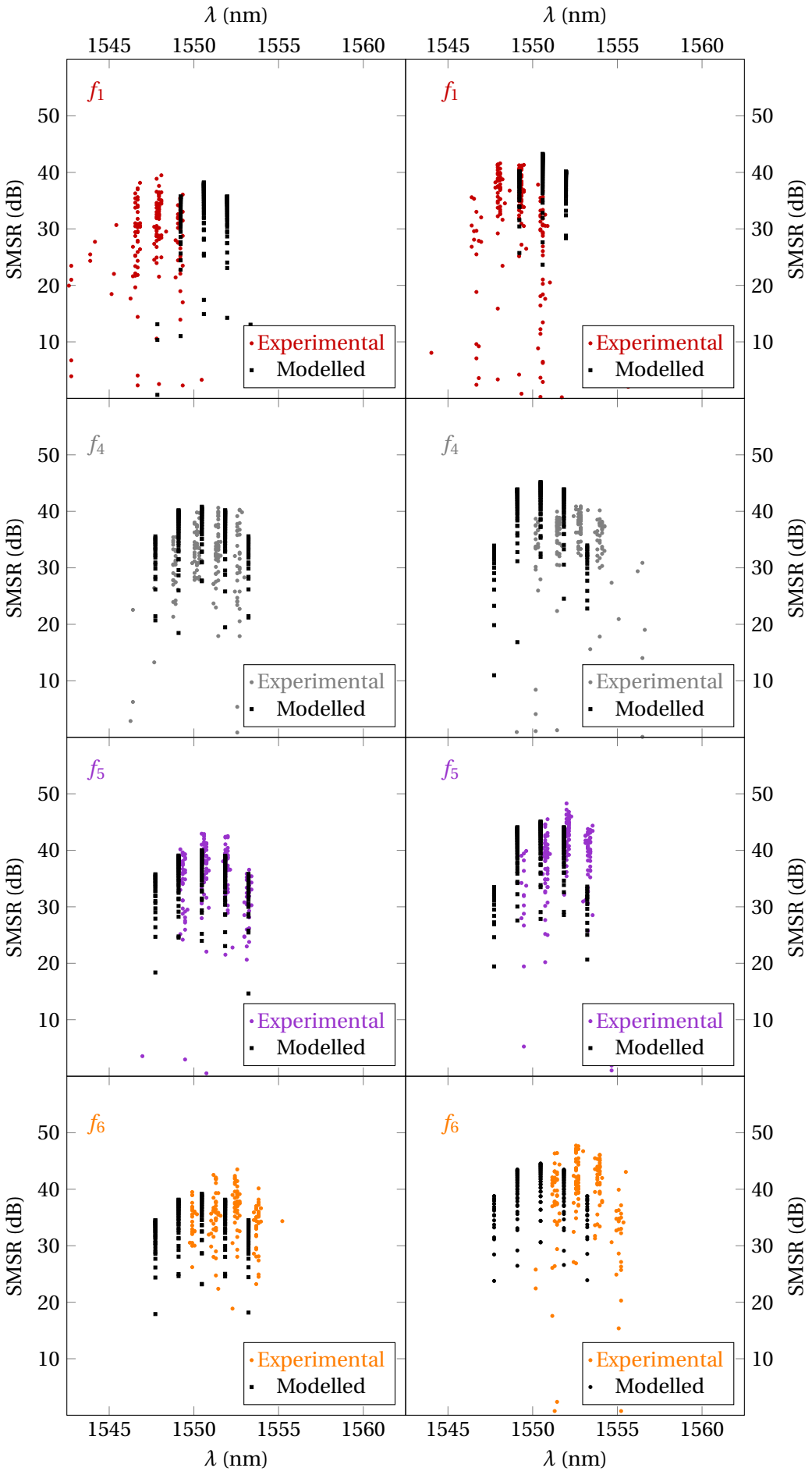


FIGURE 6.6: SMSR versus wavelength at 100 mA for the 275 µm gratings in Fig. 6.3, parameters in Tab. 6.3. Left column before and right after coating.

6.2.1.2 350 µm **HR**

In Fig. 6.7 we can see, as an example, the spectrum for the device with the highest SMSR for each function in the 350 µm HR data set. In Fig. 6.8 we can see the overlaid experimental and modelled SMSR versus wavelength distributions. We can see that the SMSR is significantly higher than what the Fourier model predicts, particularly for f_1. We also see a large increase in SMSR compared to the 275 µm HR devices, in Fig. 6.6. This is the opposite trend to what the Fourier model predicts. The selected modes are predicted by the Fourier model and remain similar to the $L = 275$ µm devices. However, the breadth of wavelengths for each selected mode is wider, and the range of SMSR values is smaller.

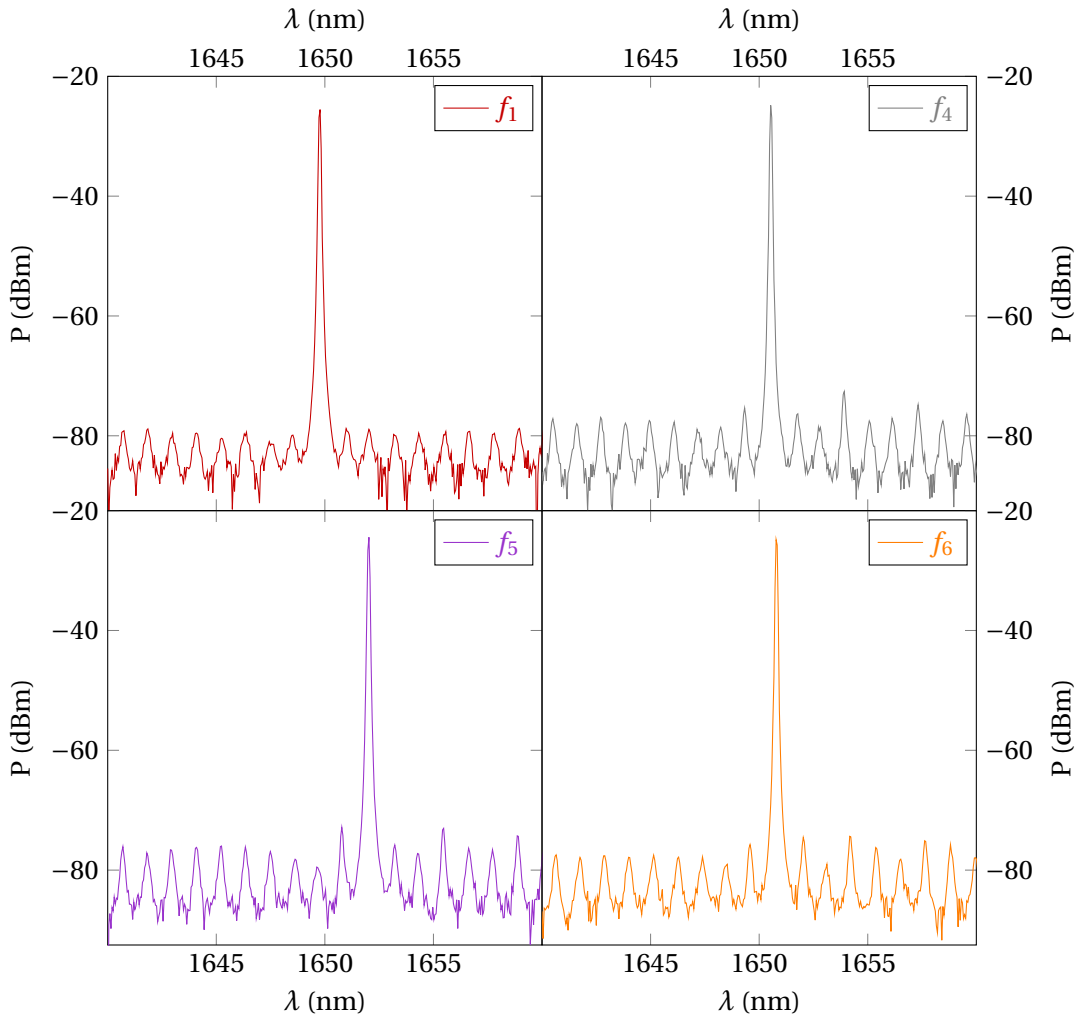


FIGURE 6.7: Experimental spectra with the device with the highest SMSR in the data at 50 mA forward current. For the 350 µm HR gratings in Fig. 6.3, designed using parameters in Tab. 6.3.

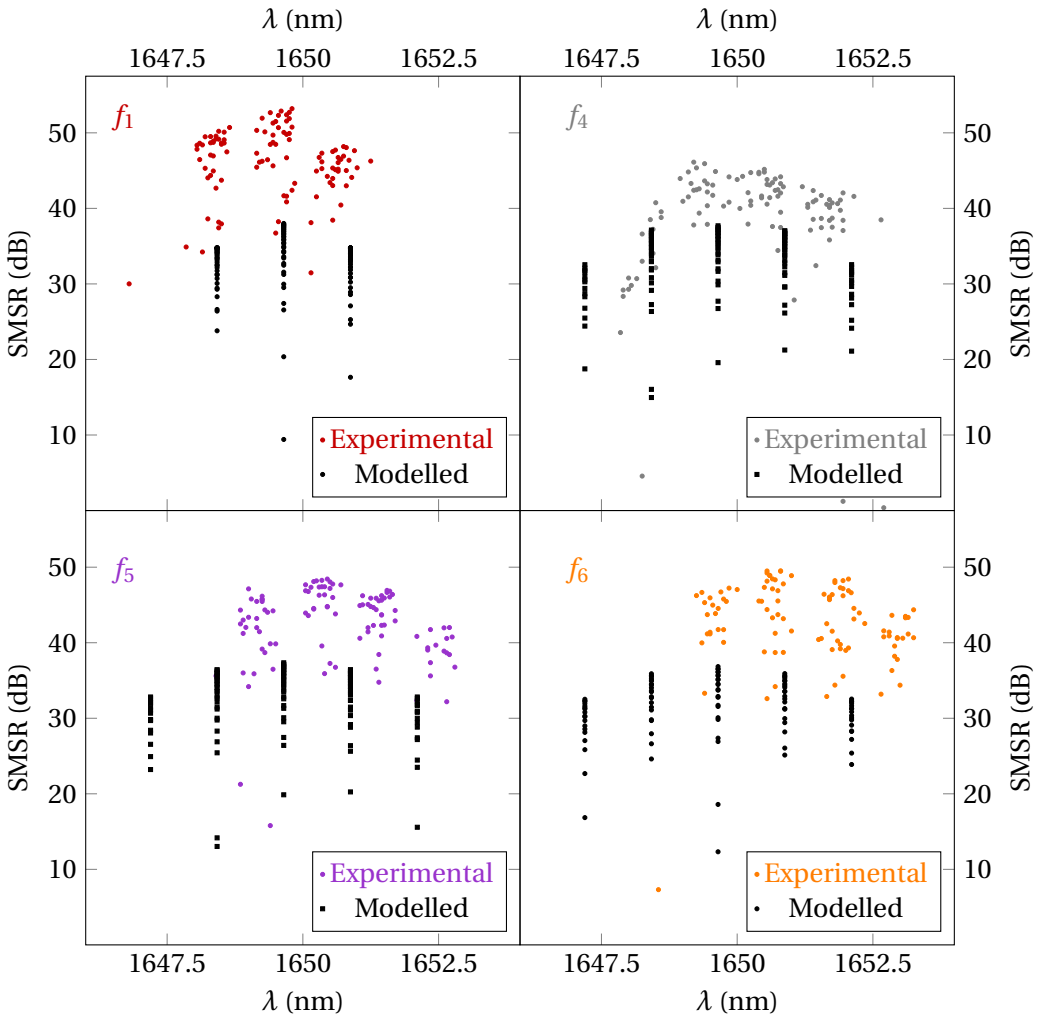


FIGURE 6.8: SMSR versus wavelength at 50 mA for the 350 µm HR gratings in Fig. 6.3, parameters in Tab. 6.3.

6.2.2 General performance

6.2.2.1 275 µm **UC → HR**

Comparing the box plots of the performance parameters for the uncoated to coated 275 µm devices in Fig. 6.9; the SMSR and the single-facet output power at 100 mA, and the threshold current all improve with HR coating. Each of these factors is related to the mirror loss threshold. The improvement is expected for the output power and threshold current; however, as a change in mirror loss changes the shape of the modal mirror loss function and the spectral gain peak position, this improvement was not predicted for SMSR. The inter-quartile range of most of the performance metrics is reduced, meaning device performance is more predictable after HR coating, and HR coating can improve the yield for other performance metrics as well as SMSR. There tend to be more inter-quartile range outliers (large black dots) after HR coating. Testing devices, then applying a HR coating at a later date and re-testing, is more likely to result in damage to the device causing performance issues.

Tab. 6.5 and Tab. 6.6 compare the median performance values uncoated to coated devices for each function, with a slope efficiency calculated using the procedure in Sec. 5.2.2. However, for the HR coated devices, we had to account for the difference in output power (P_l, P_r) from the "Left" and "Right" due to the difference in power reflectance (R_l, R_r) of the two facets [121]

$$P_l = P_r \sqrt{\frac{R_r}{R_l}} \left(\frac{1 - R_l}{1 - R_r} \right). \tag{6.3}$$

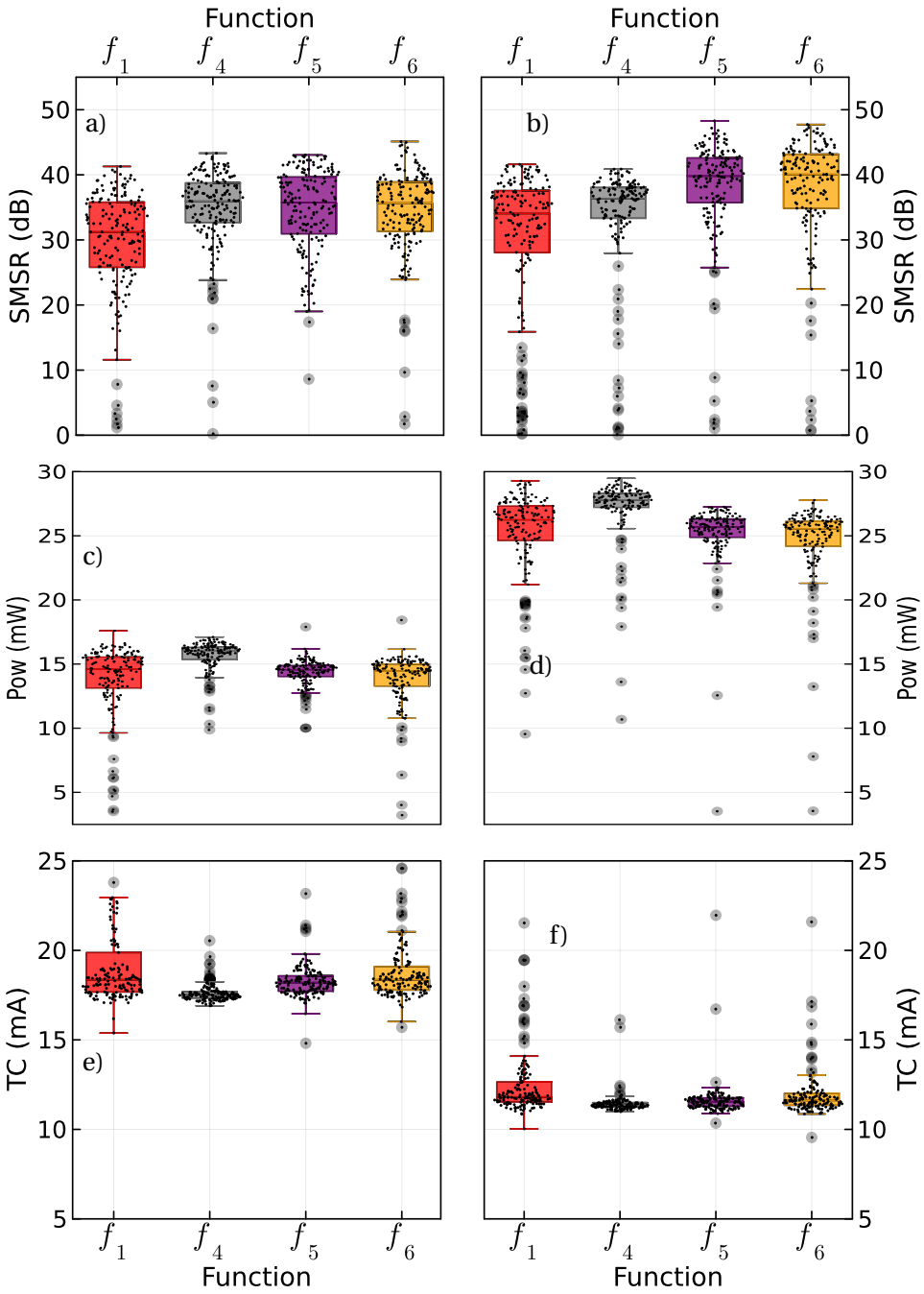


FIGURE 6.9: Box plots: SMSR (a) and b)) and power output (c) and d)) at 100 mA, and threshold currents (e) and f)) for the 275 µm gratings in Fig. 6.3, design parameters in Tab. 6.3. Left column is before and right is after coating. Large black dots are data points outside the inter-quartile range.

Function	P (mW) @ 100 mA	I_{th} (mA)	η (W/A)	SMSR @ 100 mA (dB)
f_1	14.6 ± 3.0	18.4 ± 3.4	0.36 ± 0.1	30.3 ± 7.6
f_4	16.0 ± 1.2	17.5 ± 0.8	0.39 ± 0.03	32.3 ± 6.7
f_5	14.6 ± 1.4	18.2 ± 1.2	0.36 ± 0.04	35.4 ± 6.8
f_6	14.4 ± 2.0	18.4 ± 1.8	0.35 ± 0.06	35.7 ± 4.3
Fabry-Pérot	21.8 ± 4.0	14.5 ± 3.1	0.51 ± 0.14	

TABLE 6.5: 275 µm UC experimental median device performance comparison. For 275 µm gratings in Fig. 6.3, including a Fabry-Pérot cavity, designed using parameters in Tab. 6.3.

Function	P (mW) @ 100 mA	I_{th} (mA)	η (W/A)	SMSR @ 100 mA (dB)
f_1	26.2 ± 3.3	11.8 ± 2.1	0.31 ± 0.07	34.1 ± 11.0
f_4	27.8 ± 2.6	11.4 ± 0.6	0.33 ± 0.03	36.4 ± 8.8
f_5	25.7 ± 2.5	11.6 ± 1.0	0.3 ± 0.04	39.8 ± 8.0
f_6	25.6 ± 3.0	11.6 ± 3.0	0.3 ± 0.09	40.1 ± 8.9

TABLE 6.6: 275 µm HR coated experimental median device performance comparison. For 275 µm gratings in Fig. 6.3, designed using parameters in Tab. 6.3.

6.2.2.2 350 µm **HR**

The median performance values for the 350 µm HR devices are listed in Tab. 6.7, with slope efficiency calculated as in the previous section, accounting for the two different facet reflectivities. Going from 275 → 350 µm cavity length HR devices, Fig. 6.9→Fig. 6.10; the median SMSR and threshold current have both increased and the single-facet output power has decreased. The median values for SMSR and output power between data sets cannot be compared as the 350 µm HR devices are biased at a lower current. The threshold current is dependent on the cavity length, the wavelength of the device, and the cavity material, so these median values cannot be compared either.

The spread in values is similar for SMSR but increases for the threshold current and output power from 275 µm HR to 350 µm HR. The spread in these values can be related to grating effects, and are a meaningful comparison. We can also see that the number of outliers has reduced for the 350 µm HR compared to the 275 µm HR devices.

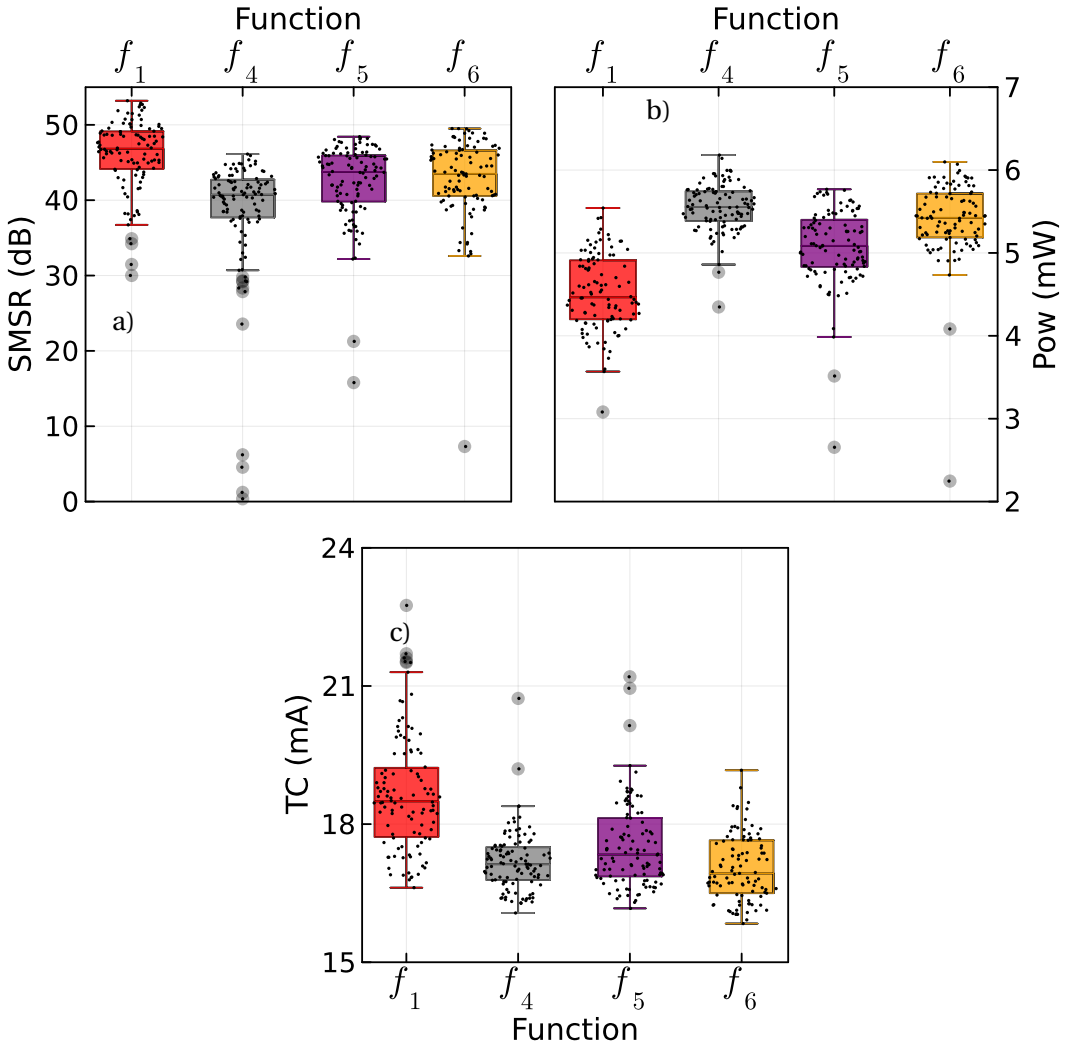


FIGURE 6.10: Box plots: a) SMSR and b) power output at 50 mA, and c) threshold current for the 350 µm HR gratings in Fig. 6.3 and design parameters in Tab. 6.3. Large black dots are data points outside the inter-quartile range.

Function	P (mW) @ 50 mA	I_{th} (mA)	η (W/A)	SMSR @ 50 mA (dB)
f_1	4.5 ± 0.5	18.5 ± 1.2	0.15 ± 0.02	46.8 ± 4.6
f_4	5.6 ± 0.3	17.1 ± 0.7	0.17 ± 0.01	40.7 ± 8.2
f_5	5.1 ± 0.5	17.3 ± 1.6	0.16 ± 0.02	43.8 ± 5.2
f_6	5.4 ± 0.5	16.9 ± 1.5	0.17 ± 0.02	43.5 ± 5.5
Fabry-Pérot	11.4 ± 0.2	13.5 ± 0.1	$0.32 \pm 6 \times 10^{-3}$	

TABLE 6.7: 350 µm HR coated experimental median device performance comparison. For 350 µm HR gratings in Fig. 6.3, including a Fabry-Pérot cavity, designed using parameters in Tab. 6.3.

6.3 Analysis

Here we will analyse the effect of HR coating the "Left facet" on optical grating loss, mode selectivity, and SMSR yield. The most striking aspect of the comparison of the SMSR versus wavelength distributions in Sec. 6.2.1 is the > 10 dB underestimation of SMSR by the Fourier model for the 350 µm HR devices; we will investigate the impact of slot over etching on this result.

6.3.1 Loss

We performed the same loss calculations as in Sec. 5.3.2.2, for the three data sets in this chapter. For the 275 µm devices we used the Fabry-Pérot structures dispersed along the bars of devices to calculate a background waveguide propagation loss of 26.9 cm^{-1} for a median single-facet output power of 21.8 ± 4.0 mW and a median threshold current of 14.5 ± 3.1 mA. This is 3.9 cm^{-1} higher than the devices in Sec. 5.3.2.2.

Function	α_g (cm^{-1})	Loss per slot (cm^{-1})	Median slot gap (µm)	α_p (cm^{-1})
f_1	31.6	2.0	5.6	58.5
f_4	23.4	1.2	4.1	50.3
f_5	31.8	1.6	5.4	58.7
f_6	33.0	1.7	5.4	59.9
Fabry-Pérot				26.9

TABLE 6.8: 275 µm UC function comparison for calculated grating loss, loss per slot, median slot gap, and total propagation loss for cavity. For the 275 µm gratings in Fig. 6.3, designed using parameters in Tab. 6.3. Loss was calculated using median values in Tab. 6.5.

For the 275 µm HR devices, the mirror loss value decreased from 47.3 cm^{-1} to 24.6 cm^{-1}. We used the same waveguide propagation loss as the uncoated devices, 26.9 cm^{-1}, as the coated Fabry-Pérot cavity results were not available. In Tab. 6.9 we can see that the slot loss has approximately halved for each function. A loss change on this scale cannot be explained by experimental variation. This indicates that the slot loss decreases after HR coating the "Left facet" for index-patterned devices. Comparing the grating loss for 275 µm UC devices in this chapter with the 275 µm UC devices in the previous chapter, we can see that this value has also approximately halved.

Function	α_g (cm^{-1})	Loss per slot (cm^{-1})	Median slot gap (µm)	α_p (cm^{-1})
f_1	12.4	0.8	5.1	39.3
f_4	9.0	0.5	3.9	35.9
f_5	13.8	0.7	4.6	40.7
f_6	14.1	0.7	4.4	41.0

TABLE 6.9: 275 µm HR function comparison for calculated grating loss, loss per slot, median slot gap, and total propagation loss for the cavity. For the 275 µm gratings in Fig. 6.3, designed using parameters in Tab. 6.3. Loss was calculated using the median values in Tab. 6.6.

For the 350 µm HR devices, the background waveguide propagation loss of the Fabry-Pérot structures was calculated to be 25.9 cm^{-1} for a median single-facet power output of 11.4 ± 0.2 mW, accounting for unequal facet reflectivity using Eq. 6.3, and a median threshold current of 13.5 ± 0.1 mA. The mirror loss was changed to 19.1 cm^{-1}, and the frequency, f, was changed to match the 1650 nm lasing wavelength of the device. We can see a significantly higher grating loss for each of the gratings compared to the 275 µm HR devices.

Function	α_g (cm^{-1})	Loss per slot (cm^{-1})	Median slot gap (µm)	α_p (cm^{-1})
f_1	53.4	2.7	7.6	79.3
f_4	37.5	1.9	4.7	63.4
f_5	45.1	2.3	5.5	71
f_6	41.1	2.1	5.0	67.0
Fabry-Pérot				25.9

TABLE 6.10: 350 µm HR function comparison for calculated grating loss, loss per slot, median slot gap, and total propagation loss for cavity. For gratings in Fig. 6.3, designed using the 350 µm HR parameters in Tab. 6.3. Loss was calculated using the median values in Tab. 6.7.

Refs. [84, 122, 91] highlight that loss and reflectivity are sensitive to the etch depth at the slot reflectivities for which our devices were designed, $r = 1.2\%$. An increase in the depth of the slot of ~ 0.1 µm can double its loss and reflectivity. Given a typical range for InP etch rate, dry or chemical, is $0.1 \rightarrow 10$ µm/ min [123, 124, 125] a variation of this magnitude is possible when processing index-patterned gratings. We have seen how large increases in grating loss do not necessarily have a detrimental effect on slope efficiency, i.e., in Ch. 5 we can see the f_1 grating pattern with a median loss per slot of 3.8 cm^{-1} and a median slope efficiency of 0.29 W/A. These devices could potentially pass a minimum specification yield test, making them viable devices despite the cavity variation. We have also seen that loss is sensitive to the grating design and to changes in facet reflectivity. More research on the loss processes in index-patterned lasers is required, decoupling the effect of slot over etching.

6.3.2 SMSR sensitivity to slot depth

A doubling in slot reflectivity can be caused by a +0.1 µm increase in slot depth [91, 84]. In Fig. 6.11 the effect this has on the mode selectivity is modelled using the same procedures as in Sec. 5.2.1. To double the slot reflectivity we doubled its refractive index step reduction, Eq. 2.8; along with the necessary phase adjustments for the cavity modes to account for the decreased cavity effective refractive index, as in Eq. 3.19, causing the wavelength of the m_0 mode to change. The SMSR is calculated for the f_1 function at a 50 mA forward current and a threshold current value of 18.5 mA, since it is the median threshold current for this design.

We see a > 3 dB increase in SMSR for a doubling of slot reflectivity. Reflectivity increases in this range are possible, as although loss scales with reflectivity, loss increases of the magnitude required to double slot reflectivity may not have a detrimental effect on the device's operating parameters. Although an etch discrepancy could account for ~ 5 dB of additional SMSR, a ~ 0.35 µm over-etch to generate an additional ~ 10 dB SMSR is unlikely. However, doubling the mode selectivity would potentially mean that the device begins to operate differently from the perturbation grating regime. This requires further research. Although the threshold current is likely to increase with the depth of the slot, small variations do not significantly affect SMSR, given its logarithmic relationship with the threshold current, as can be seen in Eq. 5.2 and Eq. 5.4. For example, for a m_0 selectivity against the cavity threshold of 3.3 cm^{-1}, f_1 350 µm HR in Tab. 6.4, the SMSR for $I = 50$ mA and $I_{th} = 18.5$ mA is calculated to be 37.5 dB. If we decrease I_{th} to 15.5 mA, the SMSR increases to 38.7 dB or +1.2 dB. An $I_{th} = 15.5$ mA is lower than the lowest observed I_{th} but is a useful extreme value to demonstrate the maximum error. Although the varying threshold current contributes to a measurable change in SMSR, this effect is not large enough to account for the > 10 dB discrepancy.

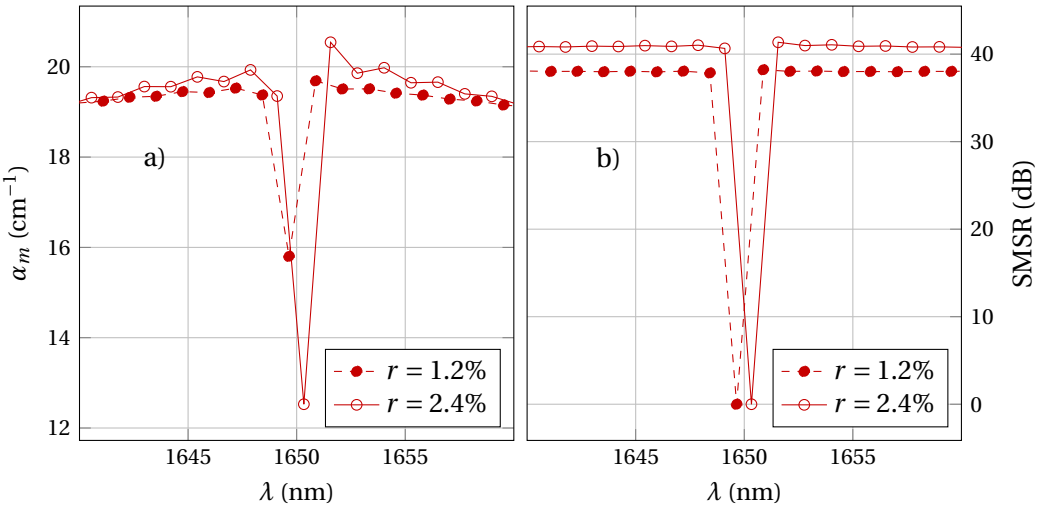


FIGURE 6.11: Comparison of a) the modal mirror loss, b) SMSR for the 350 µm HR f_1 grating in Fig. 6.3, with a doubling of slot refractive index step to double reflectivity. The rest of the parameters remain the same as in Tab. 5.2.

6.3.3 275 µm UC → HR mode selectivity

In Sec. 6.2.2.1 we can see that the experimental SMSR parameters improve with HR coating the "Left facet", even when the grating does not have its weighting adjusted for the facet reflectivity, see Tab. 5.1 and Tab. 6.4. This is happening for three reasons. One, in Sec. 6.1.1 we saw how m_0 selectivity increases for a grating with HR facet application. Two, we saw in Sec. 6.1.1 that the Fourier weighting does not change significantly if the grating slots are not near the centre of the cavity, i.e., if a grating is clearly selecting a mode against competing modes ($20\Delta\alpha$) before applying the HR coating, then the selectivity is likely to increase after the HR coating. Three, there is a decrease in α_f that increases the selectivity ratios $\frac{20\Delta\alpha}{\alpha_f}$ and $\frac{\Delta\alpha_{m_0}}{\alpha_f}$.

6.3.4 Yield

In Tab. 6.11 we have calculated the yield for the three data sets for a 40 dB SMSR minimum specification. For the 275 µm devices, we can see the importance of HR coating, with significantly more devices achieving 40 dB SMSR, despite the fact that the grating was not adjusted for the reflectivity of the facet. Further research is required on the cause of the high SMSR 350 µm HR devices, as this effect appears to contribute significantly to the SMSR yield of the device. Note for Tab. 6.11, this is only focusing on SMSR yield; a manufactured device will have to meet additional specifications, e.g., output power.

Function	275 µm UC % > 40 dB @ 100 mA	275 µm HR % > 40 dB @ 100 mA	350 µm HR % > 40 dB @ 50 mA
f_1	0.0	10.4	88.7
f_4	1.9	5.3	59.8
f_5	13.2	48.2	73.1
f_6	9.5	51.3	78.2

TABLE 6.11: Experimental SMSR yield comparison for gratings in Fig. 6.3, designed using parameters in Tab. 6.3. The wavelength selected is not necessarily λ_0.

6.4 Discussion

This chapter used our Fourier-based approach to analyse the behaviour of index-patterned lasers with a HR coating applied to the "Left facet". The device manufacture and experimental measurements were performed by Eblana Photonics Ltd..

Fourier modelling had shown that applying a HR coating to an unoptimised grating still resulted in devices with high SMSR (> 40 dB). We were able to confirm this experimentally and to analyse the reasons for it. We also saw how the grating loss decreased after HR coating. SMSR improved between the 350 μm HR and the 275 μm HR devices, in contrast to what the first-order Fourier method predicted. Although the Fourier method has predicted many of the device phenomena in this thesis, it is only modelling reflections from the slots to the cavity facets, i.e., one specific mode selection process. We used a 1D SMM semi-analytical code to assist in grating design and cavity analysis. Although useful, it only additionally captures reflections between the slots, and not other possible mode selection processes. More complete laser models including higher-dimensions (2D/3D SMM) and/or travelling waves are necessary to explore these other possible processes. The Fourier method can be accurate in the HR regime, but the accuracy of the Fourier method depends on its input parameters, which can vary significantly.

The spectrum of the index-patterned grating is relatively insensitive to changes in facet reflectivity and remains mostly unchanged after HR coating application if the grating does not have many slots near $\epsilon = 0$. We saw an increase in the impact of the slots near $\epsilon = 0$ with HR coating. We saw that this increase gets smaller the closer we get to the "Right facet", but slots near the "Right facet" still have a greater impact on mode selectivity. Overall, having a HR "Left facet" increases the number of possible high-SMSR slot patterns that can be generated.

The next chapter will demonstrate some of the ways we can take the learnings from this chapter and this thesis and apply them to maximise the performance and yield of index-patterned lasers.

Chapter 7

Conclusions & outlook

7.1 Introduction

This thesis has sought to increase the understanding of index-patterned Fabry-Pérot lasers using a Fourier-based approach to model the device cavities. We found many useful insights that can be used to improve index-patterned laser design. In Sec. 7.2 we will summarise this thesis, distil the main outcomes, and compare them to our research goals. Sec. 7.3 will discuss the paths to applying this research to maximising the performance and yield of index-patterned devices. Sec. 7.4 will explore some of the avenues for future research of index-patterned lasers, particularly from the point of view of device modelling.

Several grating designs were examined theoretically and implemented experimentally in this thesis. Based on theoretical analysis, the design function $f_6(\epsilon) = \sin^2(\pi\epsilon)$ appeared to offer the best characteristics. However, in our actual implementation of each design we were advised not to include slots within 20 μm of the end facets. In addition, it has previously been shown [9] that scattering losses from slots are reduced when slots are placed closer together. Based on these considerations, our thesis highlights a useful function, $f_4(\epsilon) = \epsilon \sin^2(2\pi\epsilon)$, to implement for index-patterned lasers. It demonstrates: strong m_0 cavity threshold selection and selection against a wide bandwidth of surrounding modes, it maintains good selection for a wide range of grating-phase angles, and has low grating loss. It has good all-round performance as opposed usefulness for a very specific design case. We note also that although the function $f_1(\epsilon) = 1$ performed least well in the case of uncoated facets, it had the best overall SMSR performance when a HR coating was applied, but at the expense of an increased threshold current and reduced output power, reflecting the wider separation of slots when function f_1 is implemented.

7.2 Summary and research outcomes

Ch. 1 started the thesis with a topical description of the index-patterned laser and a view of how it could develop with further research in the next few years. We wanted to highlight how useful the index-patterned laser is and how useful it could be in the many advancing areas of optoelectronics. We particularly mentioned silicon photonics, as this is the fastest growing area of the technology, and the index-patterned laser has many useful properties for this application.

Ch. 2 described the optical physics involved in a Fabry-Pérot laser, building up to a 1D model of a cavity and the related transfer matrix of an optical element. The goal of this chapter was essentially to describe what happens to light when it is confined in a dielectric waveguide structure, and how it can be approximated as 1D plane waves.

In Ch. 3 we discussed the development of single-wavelength lasers using the physics described in Ch. 2; including an analysis of the competing single-mode lasers, the Bragg-based DFB and DBR lasers. This chapter also explained the Fourier method that we used for index-patterned laser analysis and the SMM that we used as a general cavity analysis tool, with both being based on 1D plane wave calculations.

In Ch. 4 we saw the initial Fourier modelled results of the index-patterned cavities, where we changed the grating pattern to see how that changed the modal mirror loss spectrum of the device. This chapter mathematically proved our initial research idea of increasing the weighted-average perturbation position to increase the single-mode selectivity. We also demonstrated how a combination of sine and cosine Fourier transforms of the device grating could be used to model the mirror loss spectrum for any arbitrary perturbation position in the cavity. This is an important aspect of the research, as currently one of the greatest challenges with index-patterned lasers is the reduction in yield as a result of the random grating-facet phase from facet formation. Although we are not providing a full solution to this problem, this mathematical framework allows for this issue to be studied and potentially mitigated in the future. We also used the semi-analytical SMM to benchmark the Fourier calculation method; theoretically showing that the first-order approximation is sufficient in describing intra-cavity reflections for the perturbation grating in devices with uncoated facets.

In Ch. 5 we saw the experimental device data that supported the results of our Fourier cavity modelling. The data in this chapter also revealed some further aspects of index-patterned lasers. The most significant result was how the differences in the wavelength resonances between the grating and the cavity led to additional mode suppression and excitation. This chapter demonstrated experimentally the effectiveness of the Fourier method for modelling index-patterned devices.

Ch. 6 looked at the effect of applying a HR coating to the "Left facet" of an index-patterned laser. We saw how SMSR could be improved for an index-patterned device with HR coating even if its grating is not correctly weighted for a HR coating. We saw how a device spectrum will not change significantly after HR coating if it does not have slots near the centre of the cavity. We also saw reduced threshold current and increased "Right facet" output power as expected. For the f_1 350 µm HR devices, we saw very high SMSR (> 50 dB), beyond what the 1D Fourier method predicted. The other design functions in this set also had high SMSRs (~ 45 dB) compared to the 275 µm HR devices (~ 40 dB). We looked at the possibility of slot over-etching causing this effect, and a comparison of loss between the uncoated and HR devices revealed that the grating loss increased with HR coating.

7.3 Maximising performance and yield

7.3.1 Performance

We have seen experimentally how changing the design function can modulate SMSR and optical loss in the cavity. It is therefore important to select a design function that balances these two factors, including the particular weighting for the cavity the grating is being implemented on, i.e., facet reflectivity and cavity length. As an example, for SMSR, f_1 went from the worst performing function in the 275 µm UC regime to the best for the 350 µm HR regime, since the cavity weighting changed the spectral properties of the function between the two designs. In the uncoated facet regime, not having slots near the centre of the cavity is an important factor for high SMSR. This becomes less important for coated facets when the selective impact of slots near the centre of the cavity increases from near zero. However, slots near the "Right facet" will still have $\sim 30-40\%$ more selectivity. This means that it is still valuable to have a high density of slots near the "Right facet".

The slot number and the slot size have a maximum ceiling, so as not to incur an excessive propagation loss in the cavity and to be able to dimensionally fit in the cavity. Reducing mirror loss can increase SMSR, given the SMSR $\propto \log_{10}\left(\frac{\Delta\alpha_m}{\alpha_f}\right)$ relationship, in Sec. 5.2.1. Mirror loss can be tailored with cavity length and facet reflectivity, as seen in Eq. 2.9. Increasing the length of the cavity reduces mirror loss; however, this reduces the mode selectivity of the grating as mode selectivity has an inverse relationship with the cavity length, $\frac{1}{L}$ in Sec. 6.1.3. Changing the cavity length will also have design trade-offs in terms of threshold current and output power [126], making it a difficult design parameter to change in terms of maximising the SMSR of the device. Increasing the reflectivity of the "Right facet" also reduces mirror loss, Eq. 2.9, while simultaneously increasing mode selectivity. To maximise SMSR, maximising the "Back facet" reflectivity is vital.

When the device mirror threshold decreases after facet application, the ratio of mode selection to cavity mirror loss increases $\left(\frac{\Delta\alpha_m}{\alpha_f}\right)$, which means that the mirror spectral function has a greater impact on device SMSR than purely m_0 selectivity. This means that selecting the optimal grating pattern becomes more important in the HR regime. We can also conclude that $\frac{\Delta\alpha_{m_0}}{\alpha_f}$ and $\frac{20\Delta\alpha}{\alpha_f}$ are more important numbers to consider when designing high-SMSR lasers than purely $\Delta\alpha_m$ and $20\Delta\alpha$.

Reducing the cavity length also increases the mode spacing, as expressed in Eq. 2.23. As our method fundamentally controls the mode number, increasing the mode spacing will increase the bandwidth of modal control of our grating. In short-cavity devices, when the mode spacing is large, the mode-suppression bandwidth is not as important a factor. The high mirror loss with short cavity length decreases the ratio of modal threshold selectivity to mirror loss, $\frac{\Delta\alpha_{m_0}}{\alpha_f}$. This means having a function with a narrow selectivity bandwidth, but strong m_0 selectivity is required. For devices with long cavities, the opposite becomes true. The devices will naturally have higher $\frac{\Delta\alpha_{m_0}}{\alpha_f}$ factors, but since the mode spacing is small, functions with wider modal control bandwidths are required. The gain-bandwidth is therefore also an important factor to consider when designing the device grating, as suppressing modes more than five modes away from the m_0 device may not be of great importance if there is a steep roll-off in the spectral gain-bandwidth and the laser is operating in a thermally stable environment. More of the spectral content of the design function could be applied to suppress modes within a narrow bandwidth around m_0 to further improve performance.

We have seen how $f(\epsilon) = 1$ is the best performing function for the HR facet 350 µm devices, beyond what our Fourier model can predict. More research is required on the effectiveness of this grating pattern.

7.3.2 Yield

In terms of device yield, functions with greater $m_{0\pm1}$ selectivity in both the in-phase and anti-phase grating positions will have a higher SMSR yield, as well as more uniform threshold current and power output parameters. Modes selected closer to m_0 will be closer in spectral gain, dispersion, and cavity loss compared to the modes at the gain-bandwidth edges. HR application increases the lasing mode selectivity across the grating-facet phase cycle, and therefore also increases the uniformity and minimum in the range of the performance factors which are related to these factors (SMSR, threshold current, and power output).

It has been shown for slots designed to have a reflectivity of about 1.2% that minor changes in slot depth can result in significant variation in terms of modal selectivity, wavelength selected, and grating loss. This is due to the strong dependence of a slot reflectivity/loss on slot depth, Fig. 3 in Ref. [84] and Fig. 2 a) in Ref. [91]. For a predictable manufacturing process, this is not an ideal regime to operate in. Having more predictable reflectivity/loss means more predictable device behaviour, benefitting device yield. There are two potential routes to overcome this. One is increasing the number of slots but making them shallower, which places the device in a more linear section of the reflectivity/loss versus slot depth curve. The other possibility is to use deep holes/pits etched through the device waveguide [127, 32], where the reflectivity and loss are saturated and relatively small changes to the depth of the etch (±0.2 μm) will no longer change reflectivity/loss [15]. Although the depth of etch does not have to be tightly controlled for these index steps, they also show a high optical loss [127, 32].

In addition, the HR 350 μm f_1 function shows a high yield, further research into this device could also significantly improve yield.

7.4 Future modelling paths

We have mentioned several times in the thesis the possibility of using higher-dimensional models to analyse index-patterned lasers, i.e., 2D SMMs [84]. The 1D Fourier and SMM models we used were able to accurately predict many behaviours of index-patterned lasers, but they are heavily prescribed and require the index-patterned cavity to operate within the bounds of the design parameters. 2D SMMs can more naturally incorporate cavity variations, such as grating loss from slot etch depth.

The most pressing effect for higher-dimensional modelling is the behaviour of the mode in the vertical extent, $\hat{y}$ in Fig. 2.3, i.e., the effects of the mode interacting with the ridge slot. Analysis on the vertical, $\hat{y}$ in Fig. 2.3, effects of a single slot in isolation has been done [84, 91]. A 2D SMM including the vertical and longitudinal planes, $\hat{z}$ and $\hat{y}$ in Fig. 2.3, of the complete cavity structure is required. In addition, a combined horizontal and longitudinal model, $\hat{x}$ and $\hat{z}$ in Fig. 2.3, would be useful to analyse the effect of changes in the distribution of the lateral E-field. 2D SMMs are more than a one-order-of-magnitude increase in computational workload; however, these calculations are relatively easy to parallelise [128]. The availability of commercial graphics processing units has increased significantly in recent years, which means that this type of modelling is possible on personal computers and does not require large and expensive computational clusters [129].

In terms of grating design specifically, the Fourier method is a good starting point given how quick it is to make spectral calculations and how accurate it can be to predict the mirror loss threshold spectrum. Higher-dimensional numerical optimisation routines could be applied to the Fourier-designed pattern with smaller movements of the slot position and size to maximise performance [22, 23]. Many grating structures could be quickly modelled with the Fourier method, and the best performing ones could be chosen for further numerical optimisation.

Time-based modelling of the cavity would be particularly useful, as index-patterned lasers are beginning to be exploited for their linewidth properties, which is related to temporal of frequency and power in the steady-state. A time-based SMM could be used [130, 131]. An interesting combination could be the approach used in Ref. [89] with our research approach that compares different design functions. In Ref. [89], the authors changed the slot number and refractive index step for the $f(\epsilon) = 1$ function and studied how this affected the cavity E-field over time. The various functions in this thesis could be applied to this modelling approach to see how changing the density of the slots along the cavity affects active device performance. Grating design functions could be optimised to maximise parameters such as linewidth and direct modulation frequency of the cavity [11, 55]. A time-based calculation could potentially capture more accurately the fields that oscillate in the cavity approaching threshold gain. The SMM calculation we used is based on performing exponential calculations of large numbers for each section of the waveguide. A time-based SMM could break these calculations into smaller steps, putting smaller values into the exponent each time, reducing the risk of an error.

We also highlighted in the thesis the possibility of using other types of refractive index perturbations instead of slots in the ridge. Some of this research will occur naturally, since III-V gain material blended with silicon waveguides for laser sections on a silicon PIC will have a significant deviation from the assumed TE plane wave interacting with a perfect 1D virtual layer that we assume [36]. There are two possible interesting developments from this strand of modelling. One, is the potential reduced cost in manufacturing of index-patterned devices from using different perturbations. Two, is how the active and spectral properties of a device would change as the type of perturbation changes.

References

[1] Ian Smith. *Data centres gobble up 18% of Ireland's electricity as country struggles with climate targets*. Accessed: 24-05-2024. 2023. URL: %7Bhttps://www.euronews.com/green/2023/06/13/data-centres-gobble-up-18-of-irelands-electricity-as-country-struggles-with-climate-target#:~:text=Green%20Green%20News-,Data%20centres%20gobble%20up%2018%25%20of%20Ireland's%20electricity,country%20struggles%20with%20climate%20targets&text=New%20official%20figures%20show%20data,to%20meet%20its%20climate%20targets%7D.

[2] Robert McKenna et al. "Self-heating allows athermal laser diode wavelength control using a thermally insulating sub-mount over a 70°C range". In: *Optics Express* 31.20 (2023), pp. 32058–32066.

[3] Jinwei Gao et al. "TEC power consumption in laser array packaging". In: *Optical and Quantum Electronics* 49 (2017), pp. 1–13.

[4] Wenzhen Liu et al. "High-power 894 nm semiconductor lasers for Cs atom pumping based on surface high-order gratings". In: *Conference on Lasers and Electro-Optics (CLEO)*. 2022.

[5] Pinliang Dong and Qi Chen. *LiDAR Remote Sensing and Applications*. 2017.

[6] Daniel Pérez et al. "Multipurpose silicon photonics signal processor core". In: *Nature Communications* 8.1 (2017), p. 636.

[7] Wim Bogaerts et al. "Programmable photonic circuits". In: *Nature* 586.7828 (2020), pp. 207–216.

[8] Francis Idachaba, Dike U. Ike, and Orovwode Hope. "Future trends in fiber optics communication". In: *Proceedings of the World Congress on Engineering*. Vol. 1. WCE London, UK. 2014, pp. 2–4.

[9] Pijie Ma et al. “Single-mode semiconductor lasers fabricated by standard photolithography for direct modulation”. In: *Optics Express* 27.4 (2019), pp. 5502–5511.

[10] Wei-Hua Guo et al. “Integrable slotted single-mode lasers”. In: *IEEE Photonics Technology Letters* 24.8 (2012), pp. 634–636.

[11] Brian Kelly et al. “Discrete-mode laser diodes with very narrow linewidth emission”. In: *Electronics Letters* 43.23 (2007).

[12] Celine Guignard et al. “Ultra-narrow (sub-MHz) linewidth emission from discrete mode laser diodes”. In: *The European Conference on Lasers and Electro-Optics*. Optica Publishing Group. 2007, CB12_2.

[13] Marta Nawrocka et al. “Widely tunable six-section semiconductor laser based on etched slots”. In: *Optics Express* 22.16 (2014), pp. 18949–18957.

[14] Jack Mulcahy et al. “60 nm widely tunable three section slot laser”. In: *IEEE Journal of Quantum Electronics* 59.6 (2023), pp. 1–6.

[15] Larry A. Coldren et al. “Single longitudinal mode operation of two-section GaInAsP/InP lasers under pulsed excitation”. In: *IEEE Journal of Quantum Electronics* 19.6 (1983), pp. 1057–1062.

[16] Brian Corbett and David McDonald. “Single longitudinal mode ridge waveguide 1.3 μm Fabry-Pérot laser by modal perturbation”. In: *Electronics Letters* 31.25 (1995), pp. 2181–2182.

[17] David A. Kozlowski et al. “Single-mode 1.3 μm Fabry-Pérot lasers by mode suppression”. In: *Electronics Letters* 31.8 (1995), pp. 648–650.

[18] David McDonald and Brian Corbett. “Performance characteristics of quasi-single longitudinal-mode Fabry-Perot lasers”. In: *IEEE Photonics Technology Letters* 8.9 (1996), pp. 1127–1129.

[19] John Patchell et al. “Specifying the wavelength and temperature tuning range of a Fabry-Pérot laser containing refractive index perturbations”. In: *Opto-Ireland*. 2005.

[20] Michael J. Wallace et al. “Genetic algorithm optimization of high order surface etched grating tunable laser array”. In: *Optics Express* 28.6 (2020), pp. 8169–8184.

[21] Daniel Erni, Michael M. Spühler, and Jürg Fröhlich. “Evolutionary optimization of non-periodic coupled-cavity semiconductor laser diodes”. In: *Optical and Quantum Electronics* 30 (1998), pp. 287–303.

[22] Göran Adolfsson, Jörgen Bengtsson, and Anders Larsson. “Spectral engineering of semiconductor Fabry-Pérot laser cavities in the weakly and strongly perturbed regimes”. In: *Journal of Optical Society of America B* 27.1 (2010), pp. 118–127.

[23] Göran Adolfsson et al. “Realization of spectrally engineered semiconductor Fabry-Pérot lasers with narrow geometrical tolerances”. In: *Journal of Applied Physics* 109.9 (2011), p. 093112.

[24] Stephen O’Brien and Eoin P. O’Reilly. “Theory of improved spectral purity in index-patterned Fabry-Pérot lasers”. In: *Applied Physics Letters* 86.20 (2005), p. 201101.

[25] Paul Lambkin, Chris Percival, and Brian Corbett. “Reflectivity measurements of intra-cavity defects in laser diodes”. In: *IEEE Journal of Quantum Electronics* 40.1 (2004), pp. 10–17.

[26] Niall D. Boohan, Brian Corbett, and Eoin P. O’Reilly. “Robust single frequency index-patterned laser design using a Fourier design method”. In: *Optics Express* 31.7 (2023), pp. 11536–11546.

[27] Richard Phelan et al. “Mid-infrared InP-based discrete mode laser diodes”. In: *Optical Fiber Applications*. 2019. Chap. 2.

[28] Jing Li et al. “High-power semiconductor laser fabricated by standard photolithography for direct modulation”. In: *IEEE Photonics Technology Letters* 35.6 (2023), pp. 289–292.

[29] Christopher Herbert et al. “Discrete-mode lasers for communication applications”. In: *IET Optoelectronics* 3.1 (2009), pp. 1–17.

[30] Christopher Percival et al. “Economic single-mode lasers for WDM”. In: *Opto-Ireland*. 2003.

[31] Aritra Roy, Saroj K. Patra, and Tomasz Piwonski. “Design and fabrication of low-cost tunable semiconductor swept-source lasers at 850 nm”. In: *Optical Components and Materials XVIII*. 2021.

[32] Kevin Shortiss et al. “Inverse scattering method design of regrowth-free single-mode semiconductor lasers using pit perturbations for monolithic integration”. In: *IEEE Photonics Journal* 10.5 (2018), pp. 1–10.

[33] Niamh Kavanagh, David Goulding, and Fatima C. Garcia Gunning. “Stable injection locking with slotted Fabry-Pérot lasers at 2 μm”. In: *Journal of Physics: Photonics* 1.1 (2018), p. 015005.

[34] Yongjun Tang et al. “Narrow-linewidth GaN-on-Si laser diode with slot gratings”. In: *MDPI Nanomaterials* 11.11 (2021), p. 3092.

[35] Zhuo Gao et al. “Improved spectral characteristics of 980 nm broad area slotted Fabry-Pérot diode lasers”. In: *Journal of Semiconductors* 33.1 (2012), p. 014007.

[36] Torrey Thiessen et al. “Back-side-on-BOX heterogeneously integrated III-V-on-silicon O-band discrete-mode lasers”. In: *Optics Express* 28.26 (2020), pp. 38579–38591.

[37] Jingzhi Huang et al. “Monolithic Quantum Dot Discrete Mode Laser on SOI”. In: *ACS Photonics* 10.6 (2023), pp. 1813–1820.

[38] John E. Carroll, James Whiteaway, and Richard G.S. Plumb. *Distributed Feedback Semiconductor Lasers*. Vol. 10. 1998.

[39] Jack Mulcahy, Frank H. Peters, and Xing Dai. “Modulators in silicon photonics—heterogenous integration and beyond”. In: *MDPI Photonics* 9.1 (2022), p. 40.

[40] John McCarthy and Frank H. Peters. “On-chip gain switched frequency comb generation using a two sectioned single cavity laser without additional optical injection”. In: *Optics Express* 31.18 (2023), pp. 29619–29626.

[41] Tao Shi et al. “Flip-chip bonded evanescently coupled III-V-on-Si single-mode laser with slotted feedback structure”. In: *IEEE Photonics Technology Letters* 33.14 (2021), pp. 739–742.

[42] Mengke Li et al. “Design and fabrication of 1.55 μm broad area slotted single-mode Fabry-Pérot lasers”. In: *Journal of Semiconductors* 37.3 (2016), p. 034007.

[43] Qiaoyin Lu et al. “Design of slotted single-mode lasers suitable for photonic integration”. In: *IEEE Photonics Technology Letters* 22.11 (2010), pp. 787–789.

[44] Dovydas Mickus et al. “Multi-channel wide range athermal operation of slotted surface grating lasers for athermal DWDM”. In: *Optics Continuum* 1.2 (2022), pp. 345–354.

[45] Michael J. Wallace et al. “Athermal operation of multi-section slotted tunable lasers”. In: *Optics Express* 25.13 (2017), pp. 14414–14426.

[46] Sergey Melnik, Guillaume Huyet, and Alexander V. Uskov. “The linewidth enhancement factor α of quantum-dot semiconductor lasers”. In: *Optics Express* 14.7 (2006), pp. 2950–2955.

[47] Shuai Wang et al. “High-power, narrow-linewidth, and low-noise quantum-dot distributed feedback lasers”. In: *Laser and Photonics Reviews* 17.9 (2023), p. 2200979.

[48] Celine Guignard et al. “Low sensitivity to optical feedback and optical injection of discrete-mode lasers”. In: *Lasers and Electro-Optics Society (LEOS)*. 2006.

[49] Rui Ma et al. “Integrated polarization-independent optical isolators and circulators on an InP membrane on silicon platform”. In: *Optica* 8.12 (2021), pp. 1654–1661.

[50] Azat Abdullaev et al. “Linewidth characterization of integrable slotted single-mode lasers”. In: *IEEE Photonics Technology Letters* 26.22 (2014), pp. 2225–2228.

[51] Zhuqiang Q. Zhong et al. “Photonic millimeter wave generation and stabilization in optically injected discrete-mode semiconductor lasers subject to photonic filter feedback”. In: *Journal of Lightwave Technology* (2023), pp. 1–9.

[52] Cheng-Kai Yao et al. “Microwave signal generation with discrete-mode laser diode”. In: *Laser Physics Letters* 19.5 (2022), p. 056201.

[53] Justin K. Alexander et al. “Monolithically integrated low linewidth comb source using gain switched slotted Fabry-Pérot lasers”. In: *Optics Express* 24.8 (2016), pp. 7960–7965.

[54] Wenle Weng et al. “Gain-switched semiconductor laser driven soliton microcombs”. In: *Nature Communications* 12.1 (2021), p. 1425.

[55] Zhuqiang Zhong et al. “Intermittent dynamical state switching in discrete-mode semiconductor lasers subject to optical feedback”. In: *Photonics Research* 9.7 (2021), pp. 1336–1342.

[56] Da Chang et al. “Flat broadband chaos generation in a discrete-mode laser subject to optical feedback”. In: *Optics Express* 28.26 (2020), pp. 39076–39083.

[57] Da Chang et al. “Microwave photonic signal generation in an optically injected discrete mode semiconductor laser”. In: *MDPI Photonics* 9.3 (2022), p. 171.

[58] Nils Surkamp et al. “Current tuned slotted Y-branch laser for wafer thickness measurements with THz radiation”. In: *Electronics Letters* 57.24 (2021), pp. 936–938.

[59] Minh A. Tran, Duanni Huang, and John E. Bowers. "Tutorial on narrow linewidth tunable semiconductor lasers using Si/III-V heterogeneous integration". In: *APL Photonics* 4.11 (2019), p. 111101.

[60] Rüdiger Paschotta. *Encyclopedia of Laser Physics and Technology*. 2008.

[61] *EP1550 Discrete-Mode Series*. Accessed: 11-09-2023. URL: https://eblanaphotonics.com/products/1550-dm/.

[62] Martin A. Green. *Solar cells: operating principles, technology, and system applications*. 1982.

[63] Susannah C. Heck. "Experimental study of quantum dot and dash lasers". 2009.

[64] Larry A. Coldren, Scott W. Corzine, and Milan L. Mashanovitch. *Diode Lasers and Photonic Integrated Circuits*. Vol. 36. 2. 1997, p. 616.

[65] Paul F. Liao and Paul Kelley. *Quantum well lasers*. Elsevier, 2012.

[66] Maurice G.A. Bernard and Georges Duraffourg. "Laser conditions in semiconductors". In: *physica status solidi (b)* 1.7 (1961), pp. 699–703.

[67] Joachim Piprek. *Semiconductor optoelectronic devices: introduction to physics and simulation*. Elsevier, 2013.

[68] Anthony E. Siegman. *Lasers*. 1986.

[69] Robert B. Leighton and Matthew Sands. *The Feynman Lectures on Physics*. 1965.

[70] Han Dejun and K.T. Chan. "Refractive index of AlInGaAs layers in the transparent wavelength region". In: *Proceedings of LEOS'94*. Vol. 2. IEEE. 1994, pp. 349–350.

[71] Sadao Adachi. "Optical dispersion relations for GaP, GaAs, GaSb, InP, InAs, InSb, Al_x $Ga_{1-x}As$, and $In_{1-x}Ga_xAs_yP_{1-y}$". In: *Journal of Applied Physics* 66.12 (1989), pp. 6030–6040.

[72] Eugene Hecht. *Optics*. Fourth edition. 2002.

[73] David J. Griffiths. *Introduction to Electrodynamics*. Fourth edition.

[74] Govind P. Agrawal and Niloy K. Dutta. *Semiconductor Lasers*. 2013.

[75] Michael J. Adams. *An Introduction to Optical Waveguides*. 1981.

[76] René Dändliker. "The concept of modes in optics and photonics". In: *Education and training in optics and photonics (ETOP)*. 1999.

[77] Anthony E. Siegman. "Excess spontaneous emission in non-Hermitian optical systems. II. Laser oscillators". In: *Physical Review A* 39.3 (1989), p. 1264.

[78] Niall D. Boohan. *On-Chip integration of lasers with photodetectors*. 2017.

[79] Vittorio DeGiorgio and Marlan O. Scully. "Analogy between the laser threshold region and a second-order phase transition". In: *Physics Review A* 2 (4 1970), pp. 1170–1177.

[80] Gareth Michael Lewis et al. "Measurement of transverse electric and transverse magnetic spontaneous emission and gain in tensile strained GaInP laser diodes". In: *Applied Physics Letters* 80.19 (2002), pp. 3488–3490.

[81] Mélanie M. Bay, Silvia Vignolini, and Kevin Vynck. "PyLlama: A stable and versatile Python toolkit for the electromagnetic modelling of multilayered anisotropic media". In: *Computer Physics Communications* 273 (2022), p. 108256.

[82] Raymond C. Rumpf. "Improved formulation of scattering matrices for semi-analytical methods that is consistent with convention". In: *Progress In Electromagnetics Research B* 35 (2011), pp. 241–261.

[83] Hua Yang et al. "Single facet slotted Fabry-Pérot laser and its application in photonic integrated circuits". In: *Semiconductor Lasers and Applications V*. 2012.

[84] Qiaoyin Lu et al. "Analysis of slot characteristics in slotted single-mode semiconductor lasers using the 2D scattering matrix method". In: *IEEE Photonics Technology Letters* 18.24 (2006), pp. 2605–2607.

[85] Herwig Kogelnik and Charles V. Shank. "Coupled-wave theory of distributed feedback lasers". In: *Journal of Applied Physics* 43.5 (1972), pp. 2327–2335.

[86] Stephen O'Brien et al. "Spectral manipulation in Fabry-Pérot lasers: perturbative inverse scattering approach". In: *Journal of Optical Society of America B* 23.6 (2006), pp. 1046–1056.

[87] Kevin Shortiss. "Optical comb injection for optical demultiplexing and harmonic frequency locking". 2020.

[88] Brad Osgood. *Lecture Notes for EE 261 the Fourier Transform and its Applications*. 2014.

[89] Yu Li et al. "Design and analysis of single-mode Fabry-Pérot lasers with high speed modulation capability". In: *Optics Express* 19.13 (2011), pp. 12131–12140.

[90] Timothy R. Groves. "Electron beam lithography". In: *Nanolithography*. 2014, pp. 80–115.

[91] Wei Sun et al. "Analysis of high-order slotted surface gratings by the 2D finite-difference time-domain method". In: *Journal of Lightwave Technology* 35.1 (2016), pp. 96–102.

[92] Alan V. Oppenheim et al. *Signals and Systems*. Vol. 2. 1997.

[93] Bohdan Mroziewicz, Maciej Bugajski, and Włodzimierz Nakwaski. *Physics of Semiconductor Lasers*. 2017.

[94] Frank Bello et al. "Traveling wave analysis for a high-order grating, partially slotted laser". In: *IEEE Journal of Quantum Electronics* 51.11 (2015), pp. 1–5.

[95] Govind P. Agrawal. *Fiber-Optic Communications Systems*. Third edition. Vol. 6. 2002.

[96] George Guekos. *Photonic Devices for Telecommunications: How to Model and Measure*. 1999.

[97] Kunio Tada. "Gain-coupled DFB lasers". In: *Conference on Optical Fiber Communication/International Conference on Integrated Optics and Optical Fiber Communication*. 1993.

[98] Harry J.R. Dutton. *Understanding Optical Communications*. Vol. 1. 1998.

[99] Jeff Hecht. *The Laser Guidebook*. Second edition. 1999. Chap. 20.

[100] Jens Buus, Markus-Christian Amann, and Daniel J. Blumenthal. *Tunable Laser Diodes and Related Optical Sources*. 2005.

[101] Wolfgang Zeller et al. "DFB Lasers Between 760 nm and 16 μm for Sensing Applications". In: *Sensors* 10.4 (2010), pp. 2492–2510.

[102] Andrew J. Ward et al. "Widely tunable DS-DBR laser with monolithically integrated SOA: design and performance". In: *IEEE Journal of Selected Topics in Quantum Electronics* 11.1 (2005), pp. 149–156.

[103] Yuliya A. Akulova et al. "Widely tunable electroabsorption-modulated sampled-grating DBR laser transmitter". In: *IEEE Journal of Selected Topics in Quantum Electronics* 8.6 (2002), pp. 1349–1357.

[104] Vijaysekhar Jayaraman and Zuon-Min Chuang Larry A. Coldren. "Theory, design, and performance of extended tuning range semiconductor lasers with sampled gratings". In: *IEEE Journal of quantum electronics* 29.6 (1993), pp. 1824–1834.

[105] Samir Ghosh et al. "Scalable transfer printing approach to heterogeneous integration of InP lasers on silicon-on-insulator waveguide platform". In: *Applied Physics Letters* 125.8 (2024).

[106] Javad Rahimi et al. “Demonstration of a high-efficiency short-cavity III-V-on-Si C-band DFB laser diode”. In: *IEEE Journal of Selected Topics in Quantum Electronics* 28.3: Hybrid Integration for Silicon Photonics (2022), pp. 1–6.

[107] *Performance of DFB Semiconductor Lasers*. Accessed: 2023-09-12. URL: https://www.fiberoptics4sale.com/blogs/wave-optics/performance-of-dfb-semiconductor-lasers.

[108] *Micro-integrable tunable laser assembly (μITLA) Lumentum Operations LLC*. Accessed: 08-06-2023. URL: https://www.lumentum.com/en/products/micro-itla-tunable-laser-100-khz.

[109] Brendan Roycroft et al. “Transition from perturbed to coupled-cavity behavior with asymmetric spectral emission in ridge lasers emitting at 1.55 μm”. In: *IEEE Photonics Technology Letters* 19.2 (2007), pp. 58–60.

[110] David Bitauld, Simon Osborne, and Stephen O’Brien. “Passive harmonic mode locking by mode selection in Fabry-Pérot diode lasers with patterned effective index”. In: *Optics Letters* 35.13 (2010), p. 2200.

[111] Kevin Shortiss et al. “Inverse scattering method design of regrowth-free single-mode semiconductor lasers using pit perturbations for monolithic integration”. In: *IEEE Photonics Journal* 10.5 (2018), pp. 1–10.

[112] Chih-Sheng Chang et al. “Amplified spontaneous emission spectroscopy in strained quantum-well lasers”. In: *IEEE Journal of Selected Topics in Quantum Electronics* 1.4 (1995), pp. 1100–1107.

[113] Paul W.A. McIlroy. “Calculation of the mode suppression ratio in Fabry-Pérot , DBR, and external cavity lasers”. In: *IEEE Journal of Quantum Electronics* 26.6 (1990), pp. 991–997.

[114] *The Differences Between Threshold Current Calculation Methods*. Tech. rep. MKS Instruments, Inc., 2020.

[115] Laurent Chusseau et al. “Carrier-induced change due to doping in refractive index of InP: Measurements at 1.3 and 1.5 μm”. In: *Applied Physics Letters* 69.20 (1996), pp. 3054–3056.

[116] Emilio Gini and Hans Melchior. "The refractive index of InP and its temperature dependence in the wavelength range from 1.2 μm to 1.6 μm". In: *Proceedings of 8th International Conference on Indium Phosphide and Related Materials*. 1996.

[117] *Indium Phosphide (InP) Wafers and Substrates*. Accessed: 06-03-2024. URL: https://www.shalomeo.com/Wafers-and-Substrates/SAW-Wafers-and-Crystals/InP-Semi-Growth/product-257.html.

[118] Saman Q. Mawlud. "Bias-voltage dependence on thermoelectric cooler coefficient for $Al_{0.7}Ga_{0.3}As$ and $I_{0.2}Ga_{0.8}As$ SQW laser diode". In: *Tikrit Journal of Pure Science* 16 (2011), pp. 165–170.

[119] Yin Wang et al. "Narrow linewidth single-mode slotted Fabry-Pérot laser using deep etched trenches". In: *IEEE Photonics Technology Letters* 24.14 (2012), pp. 1233–1235.

[120] Charles H. Henry. "Theory of the linewidth of semiconductor lasers". In: *IEEE Journal of Quantum Electronics* 18.2 (1982), pp. 259–264.

[121] Bohdan Mroziewicz, Mariusz Zbroszczyk, and Maciej Bugajski. "Analysis of threshold current and wall-plug efficiency of diode lasers with asymmetric facet reflectivity". In: *Optical and Quantum Electronics* 36 (2004), pp. 443–457.

[122] Jiachen Tian et al. "Analysis of high-order surface gratings based on micron lasers on silicon". In: *MDPI Photonics* 11.1 (2024), p. 92.

[123] Adachi Sadao. "Chemical etching of InP and InGaAsP/InP". In: *Journal of The Electrochemical Society* 129.3 (1982), p. 609.

[124] Chang-Zheng Sun et al. "Vertical and smooth, etching of InP by $Cl_2/CH_4/Ar$ inductively coupled plasma at room temperature". In: *Chinese physics letters* 20.8 (2003), pp. 1312–1314.

[125] Fan Ren et al. "Electron cyclotron resonance plasma etching of InP and related materials in BCl_3". In: *Solid-State Electronics* 39.5 (1996), pp. 695–698.

[126] Atsushi Kurobe et al. "Effects of well number, cavity length, and facet reflectivity on the reduction of threshold current of GaAs/AlGaAs multiquantum well lasers". In: *IEEE Journal of Quantum Electronics* 24.4 (1988), pp. 635–640.

[127] Mohamad Dernaika et al. "Deeply etched inner-cavity pit reflector". In: *IEEE Photonics Journal* 9.1 (2017), pp. 1–8.

[128] Giovanni Iadarola et al. “GPU-accelerated T-matrix algorithm for light-scattering simulations”. In: *Journal of Computational Physics* 231.17 (2012), pp. 5640–5652.

[129] John D. Owens et al. “GPU Computing”. In: *Proceedings of the IEEE* 96.5 (2008), pp. 879–899.

[130] Yuc L. Wong and John E. Carroll. “A travelling-wave rate equation analysis for semiconductor lasers”. In: *Solid-State Electronics* 30.1 (1987), pp. 13–19.

[131] Mohammed Mehdi Bouchene and Rachid Hamdi. “The effect of facets reflectivity on the static characteristics of (DFB) semiconductor laser”. In: *2018 International Conference on Electrical Sciences and Technologies in Maghreb (CISTEM)*. 2018.